Chapter 2
Fundamentals

2.1 NMR Methods

Nuclear magnetic resonance (NMR) designates the resonant interaction of nuclear magnetic dipole moments[1] $\boldsymbol{\mu}$ in an external magnetic field[2] $\boldsymbol{B_0}$ with an electromagnetic field $\boldsymbol{B_1}$.

Resonant means that only an electromagnetic field of a certain frequency is able to interact with the nuclear dipole. Underlying new concepts from quantum mechanics are briefly mentioned in Sect. 2.1.1. The basic relations for the presented NMR methods are summarized in Sect. 2.1.2. In Sect. 2.1.3 the technique used to achieve spatial resolution is outlined. For NMR methods with spatial resolution, the term MRI is employed. Different quantities that can be measured by various NMR methods are presented in Sect. 2.1.4 and the following. More details can be found e.g. in the textbooks [1, 9, 10, 13, 14, 16, 22, 28, 34, 41, 49, 58, 67].

2.1.1 Notes on Quantum Mechanics

2.1.1.1 Energy Levels of a Nuclear Magnetic Dipole in an External Field

In classical magnetostatics the energy E of a magnetic dipole $\boldsymbol{\mu}$ in an external magnetic field $\boldsymbol{B_0}$ is given by the scalar product

$$E = -\boldsymbol{\mu}\,\boldsymbol{B_0}. \tag{2.1}$$

[1] Vectors are set in bold italic face.

[2] As common in NMR literature, the $\boldsymbol{B}$-field is designated as magnetic field. Alternative names are magnetic flux density or magnetic induction. In vacuum the magnetic $\boldsymbol{H}$-field is proportional to the magnetic induction with the induction constant μ_0: $\boldsymbol{B} = \mu_0 \boldsymbol{H}$.

E.H. Hardy, *NMR Methods for the Investigation of Structure and Transport*,
DOI 10.1007/978-3-642-21628-2_2, © Springer-Verlag Berlin Heidelberg 2012

In quantum-mechanical description, see e.g. [56], the dipole vector is replaced by the corresponding vector operator $\hat{\boldsymbol{\mu}}$ and the energy by the Hamilton operator:

$$\hat{H}_0 = -\hat{\boldsymbol{\mu}}\,\boldsymbol{B_0}. \tag{2.2}$$

The magnetic-dipole vector operator is proportional to the nuclear spin operator $\hat{\boldsymbol{I}}$:

$$\hat{\boldsymbol{\mu}} = \gamma\,\hat{\boldsymbol{I}}, \tag{2.3}$$

where γ is designated as gyromagnetic ratio.[3] Thus the energy quantization follows from the quantization of the nuclear spin. The corresponding spin quantum number I is integer or half-integer. Both I and γ are ground-state properties of the nucleus, as rest mass and charge. For an isolated nuclear spin in an external magnetic field, the quantization axis is given by the direction of the latter. It is usually chosen as z direction, i.e., $\boldsymbol{B_0} = B_0\boldsymbol{e}_z$. The scalar product in (2.2) can thus be written as

$$\hat{H}_0 = -\gamma\,\hat{I}_z B_0. \tag{2.4}$$

The eigenvalues of the z component of a quantum mechanical angular momentum are $m\hbar$ with the Planck constant $\hbar$ and the magnetic quantum number $m = -I, -I+1, \ldots, I$. It follows for the eigenvalues E_m of the Hamilton operator:

$$E_m = -\gamma m\hbar B_0. \tag{2.5}$$

Here only the selection rule $\Delta m = \pm 1$ is considered. Accordingly, the magnitude of the energy difference for a transition amounts to

$$|\Delta E| = \gamma\hbar B_0. \tag{2.6}$$

2.1.1.2 Notes on Photons and First Derivation of the NMR Master Equation

The Planck–Einstein equation

$$\Delta E = \hbar\omega \tag{2.7}$$

states that electromagnetic waves with angular frequency ω can behave as particles called photons with energy $\hbar\omega$ that can be absorbed or emitted in transitions with corresponding energy, see Fig. 2.1. For the moment the common assumption is made that this concept is also applicable for the excitation and detection of the NMR signal. Combination of the resonance condition (2.7) and the energy difference (2.6) yields the NMR master equation from quantum mechanical energy considerations:

[3] Sometimes more appropriate as magnetogyric ratio.

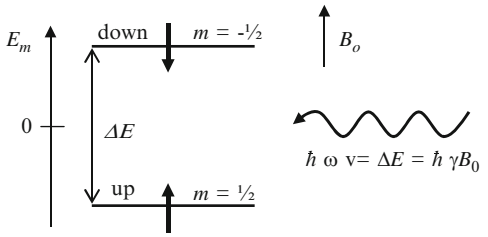

Fig. 2.1 Common representation of signal excitation and detection in NMR as resonant interaction of a photon with energy $\hbar\omega$ and a nuclear magnetic dipole in the field $\boldsymbol{B_0}$, here for spin quantum number $I = 1/2$. In the "up" state with magnetic quantum number $m = 1/2$ the z component of the dipole is parallel to the field. This is energetically more favorable than the "down" state ($m = -1/2$) with anti parallel orientation. The scalar form of the NMR master equation (2.8) follows from the energy difference (2.6) and the Planck–Einstein equation (2.7). Although this interpretation is widely held it leads to paradoxes concerning the detected signal [35, 36]. A detailed theoretical framework relying on the concept of virtual-photon exchange was presented recently [21]

$$\omega = -\gamma B_0. \tag{2.8}$$

Here the resonance frequency ω is obtained as a scalar. In the following Sect. 2.1.2 the master equation will be derived from the classical equation of motion. The angular resonance frequency appears as angular velocity and the choice of the sign gets explained.

Whereas this description is well suited in the far-field limit it does not hold for the excitation and detection of NMR signals where near-field contributions dominate [35,36]. Recently a detailed theoretical framework relying on the concepts of quantum electrodynamics (QED [23]) was presented [21]. It is concluded that during excitation both asymptotically free photons as well as virtual photons appear whereas detection can be characterized by virtual-photon exchange only. In this context it was verified experimentally that the classical description of NMR signal as near-field Faraday induction produces correct results[35]. This classical framework used in the following also comprises the reciprocity theorem, see Sects. 2.1.9 and 2.3.4.

2.1.2 Nuclear Magnetic Resonance

2.1.2.1 Macroscopic Magnetization

The population probability P_m of energy state E_m is given in thermal equilibrium by the Boltzmann distribution:

$$P_m = \frac{\exp\{-E_m/kT\}}{\sum_{m=-I}^{I} \exp\{-E_m/kT\}}. \tag{2.9}$$

For the small energy differences in NMR the high-temperature approximation is used, meaning that the linear approximation of the exponential function is employed. Inserting expression (2.5) for the energy yields for the population probability:

$$P_m \approx \frac{1 + \gamma m \hbar B_0 / kT}{\sum_{m=-I}^{I} 1 + \gamma m \hbar B_0 / kT}. \tag{2.10}$$

The equilibrium magnetization for N_S spins of a given kind in volume V is obtained from the sum of z components of nuclear magnetization in states m weighted with P_m. Given the eigenvalue $\gamma m \hbar$ for the nuclear z magnetization the equilibrium magnetization M_z^{eq} amounts to:

$$\begin{aligned} M_z^{eq} &= \frac{N_S}{V} \sum_{m=-I}^{I} \frac{1 + \gamma m \hbar B_0 / kT}{\sum_{m'=-I}^{I} 1 + \gamma m' \hbar B_0 / kT} \gamma m \hbar \\ &= \frac{N_S}{V} \frac{\gamma^2 I(I+1) \hbar^2}{3kT} B_0. \end{aligned} \tag{2.11}$$

This relation is known as Curie's law, see also problem 2.2 on p. 46.

2.1.2.2 Classical Equation of Motion and Bloch Equations

According to classical magnetostatics the magnetic dipole moment $\boldsymbol{\mu}$ in the external field $\boldsymbol{B}$ experiences a torque $\boldsymbol{\mu} \times \boldsymbol{B}$. This results in a change of angular momentum $\mathrm{d}\boldsymbol{I}/\mathrm{d}t$. Applying the proportionality (2.3) between the magnetic dipole moment and the nuclear spin to the macroscopic magnetization $\boldsymbol{M}$ the classical equation of motion is obtained:

$$\frac{\mathrm{d}\boldsymbol{M}}{\mathrm{d}\,t} = \gamma \boldsymbol{M} \times \boldsymbol{B}. \tag{2.12}$$

Application to the magnetization (dipole density) means summation over all dipoles and division by the volume V. It is assumed that $\boldsymbol{B}$ is homogeneous in V.

For a field $\boldsymbol{B}$ constant in space and time the solution of (2.12) is a precession of the magnetization around $\boldsymbol{B}$ with the angular frequency

$$\boldsymbol{\omega_0} = -\gamma \boldsymbol{B_0}. \tag{2.13}$$

This is a second derivation of the NMR master equation. Here, the angular velocity of the so-called Larmor precession is a vector.

In the phenomenological Bloch equations [6]

$$\frac{\mathrm{d}M_x}{\mathrm{d}\,t} = \gamma(\boldsymbol{M} \times \boldsymbol{B})_x - \frac{M_x}{T_2} \tag{2.14}$$

$$\frac{\mathrm{d}M_y}{\mathrm{d}\,t} = \gamma(\boldsymbol{M} \times \boldsymbol{B})_y - \frac{M_y}{T_2} \tag{2.15}$$

$$\frac{\mathrm{d}M_z}{\mathrm{d}t} = \gamma(\boldsymbol{M} \times \boldsymbol{B})_z - \frac{M_z - M_z^{\mathrm{eq}}}{T_1} \tag{2.16}$$

the classical equation of motion is extended by an exponential relaxation toward thermal equilibrium. In favorable cases the transverse relaxation time T_2 equals the longitudinal relaxation time T_1. Frequently, the decay of transverse magnetization is significantly faster than the return of longitudinal magnetization toward thermal equilibrium.[4]

2.1.2.3 Rotating Frame of Reference

The classical equation of motion is sufficient to describe the presented results. It is usually transformed into a frame of reference rotating around z in order to simplify the solution. Further down a circular polarized transverse radio-frequency field (rf field) $\boldsymbol{B_1}$ with angular frequency $\omega_{\mathrm{rf}} \approx \omega_0$ will be introduced.[5] It is made time-independent in the rotating frame by transformation with the angular frequency ω_{rf}.[6] The transformation can be carried out using different formalisms. In [22] the explicit representations of the vectors and their time derivatives in both coordinate systems are calculated with the rotation matrix. Here, the more abstract and concise transformation from [1] is chosen. The macroscopic magnetization $\boldsymbol{M}$ is considered as object that is identical in both coordinate systems.[7] However, the motion of the object is observed differently in the rotating frame compared to the laboratory frame of reference. In the rotating frame, index "R," additional terms are obtained upon time derivation due to the time-dependence of the unit vectors. Using the product rule for the derivation and the fact that the time derivative of the unit vector is the cross product of $\boldsymbol{\omega}_{\mathrm{rf}}$ with this vector it follows

$$\left.\frac{\mathrm{d}\boldsymbol{M}}{\mathrm{d}t}\right|_{\mathrm{L}} = \left.\frac{\mathrm{d}\boldsymbol{M}}{\mathrm{d}t}\right|_{\mathrm{R}} + \boldsymbol{\omega}_{\mathrm{rf}} \times \boldsymbol{M}. \tag{2.17}$$

[4]The relation $T_2 \leq T_1$ is obtained in theoretical calculations for several relaxation mechanisms [8]. The condition that the magnitude of the magnetization cannot exceed the magnitude of the equilibrium magnetization through relaxation leads to the weaker condition $T_2 \leq 2T_1$.

[5]Usually a linear polarized field is irradiated. It can be decomposed into two counter rotating circular polarized fields. For $B_1 \ll B_0$ the component rotating with the magnetization acts as described in (2.23). The counter rotating component leads to the Bloch–Siegert Shift, see [7] and Fig. 2.2. Advanced NMR systems allow to generate only the required circular polarized component [18, 27].

[6]Experimentally, this corresponds to the signal being mixed with the rf frequency and subsequent low-pass filtering.

[7]In contrast to the representation in the form of coordinates in a column vector, denoted as "matrix representation," that differs between coordinate systems.

The left-hand side of (2.17) signifies the time derivation in the laboratory frame, index "L." Here, no additional terms arise. Insertion of the right-hand side of (2.17) in (2.12) yields

$$\left.\frac{\mathrm{d}\boldsymbol{M}}{\mathrm{d}\,t}\right|_{\mathrm{R}} = \gamma \boldsymbol{M} \times \left(\boldsymbol{B} + \frac{1}{\gamma}\,\boldsymbol{\omega}_{\mathrm{rf}}\right). \tag{2.18}$$

Distributivity and anti commutativity of the cross product has been used. The Bloch equations in the rotating frame are obtained by addition of the relaxation terms, in coordinates

$$\frac{\mathrm{d}M_x}{\mathrm{d}\,t} = \gamma\left[M_y(B_z + \omega_{\mathrm{rf}}/\gamma) - M_z B_y\right] - \frac{M_x}{T_2} \tag{2.19}$$

$$\frac{\mathrm{d}M_y}{\mathrm{d}\,t} = \gamma\left[M_z B_x - M_x(B_z + \omega_{\mathrm{rf}}/\gamma)\right] - \frac{M_y}{T_2} \tag{2.20}$$

$$\frac{\mathrm{d}M_z}{\mathrm{d}\,t} = \gamma\left[M_x B_y - M_y B_x\right] - \frac{M_z - M_z^{\mathrm{eq}}}{T_1}. \tag{2.21}$$

The objects in the right-hand side of (2.18) do not depend on the coordinate system. However, (2.19)–(2.21) contain components of the matrix representation that have to be expressed in the rotating frame.

2.1.2.4 Generation of Transverse Magnetization

If $\boldsymbol{\omega}_{\mathrm{rf}}$ and $\boldsymbol{\omega_0}$ are identical, the influence of $\boldsymbol{B_0}$ on the motion of $\boldsymbol{M}$ disappears in the rotating frame, see (2.13). At first, one additional field is considered, $\boldsymbol{B} = \boldsymbol{B_0} + \boldsymbol{B_1}$ with

$$\begin{aligned}\boldsymbol{B_1} &= B_1[\cos(\omega_{\mathrm{rf}}t + \phi_1)\boldsymbol{e_x} + \sin(\omega_{\mathrm{rf}}t + \phi_1)\boldsymbol{e_y}] \\ &= B_1[\cos(\phi_1)\boldsymbol{e_x}' + \sin(\phi_1)\boldsymbol{e_y}'].\end{aligned} \tag{2.22}$$

Primed unit vectors refer to the rotating frame of reference. Neglecting relaxation the equation of motion in the rotating frame of reference reads:

$$\frac{\mathrm{d}\boldsymbol{M}}{\mathrm{d}\,t} = \gamma \boldsymbol{M} \times \boldsymbol{B_1}. \tag{2.23}$$

The solution is denoted as Rabi nutation around $\boldsymbol{B_1}$. The angular velocity amounts to

$$\boldsymbol{\omega_1} = -\gamma \boldsymbol{B_1}. \tag{2.24}$$

Accordingly the equilibrium magnetization can be rotated e.g. on the x' axis of the rotating frame by application of a resonant $\boldsymbol{B_1}$-field with constant amplitude along the negative y' axis, i.e., $\phi_1 = -\pi/2$. The duration τ of such a "90 degree" rf pulse is related to its amplitude by $\omega_1\tau = \pi/2$, see also Fig. 2.2. The following

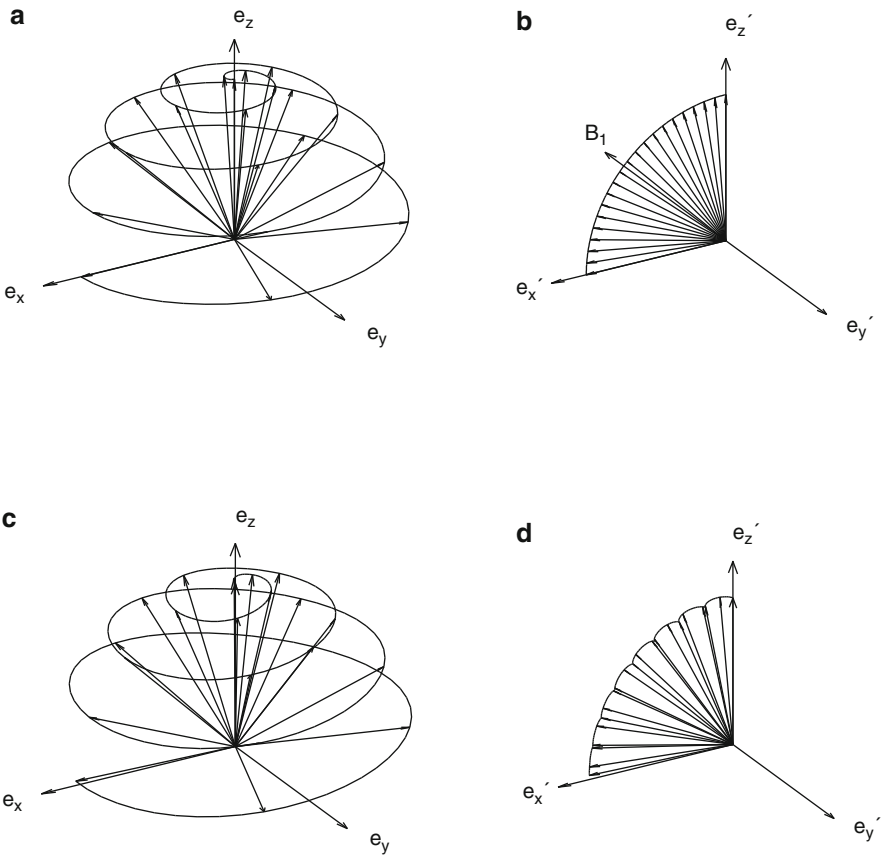

Fig. 2.2 (**a**), (**c**) numerical solution of the equation of motion (2.12) in the laboratory frame of reference. (**b**), (**d**) solution of the equation in the rotating frame (2.18). Initial magnetization is parallel to the static field $B_0 \boldsymbol{e}_z$. The resonant circular polarized $\boldsymbol{B_1}$-field, see (2.22) allows to generate transverse magnetization. For the sake of clearness, $B_0 = 16 B_1$ was chosen in (**a**). Typically, the ratio is about three powers of ten. In the experiment frequently a linear polarized field of twice the amplitude is used. The perturbance of the contained counter rotating circular polarized component is visible in the laboratory frame (**c**) and clearer in the rotating frame (**d**). For $B_1 \ll B_0$ the perturbance is marginal

precession of magnetization with ω_0 induces a weak voltage in the receiver coil,[8] see also Sect. 2.3.4. This situation is the starting point for the classical description of Fourier imaging in Sect. 2.1.3.

[8] Usually the coil transmitting $\boldsymbol{B_1}$ and the receiver coil are identical. Between transmit and receive mode a dead time of some microseconds has to be waited. For the distinction of x and y component of transverse magnetization pairs of data points can be digitized with a delay corresponding to a precession by $\pi/2$. This procedure is denoted as "sequential quadrature detection."

Finally the case of $\boldsymbol{\omega}_{\mathrm{rf}} \neq \boldsymbol{\omega_0}$ with a remaining field $B_z = B_0 + \omega_{\mathrm{rf}}/\gamma$ is mentioned. Here the nutation in the rotating frame occurs around the effective field

$$\boldsymbol{B}_{\mathbf{1}\mathrm{eff}} = B_1[\cos(\phi_1)\boldsymbol{e}_{\boldsymbol{x}}{}' + \sin(\phi_1)\boldsymbol{e}_{\boldsymbol{y}}{}'] + (B_0 + \omega_{\mathrm{rf}}/\gamma)\boldsymbol{e}_z. \tag{2.25}$$

2.1.3 Fourier Imaging

2.1.3.1 Basic Principle

Fourier imaging relies on a position-to-frequency transformation. In addition to the homogeneous fields $\boldsymbol{B_0}$ and $\boldsymbol{B_1(t)}$ required for NMR a field with homogeneous gradient is necessary. The basic principle is readily formulated using the classical equation of motion in the rotating frame [31].

As stated at the end of Sect. 2.1.2 the magnetization in the observable volume V having the x direction of the rotating frame is the starting point. Furthermore $\boldsymbol{\omega}_{\mathrm{rf}}$ and $\boldsymbol{\omega_0}$ are supposed to be identical, relaxation is neglected. Without additional fields the right-hand side of (2.18) is zero, the magnetization appears to be static.

Additional coils allow to superimpose the polarizing $\boldsymbol{B_0}$-field by fields with linear variation of the z component along the directions of the laboratory frame of reference:

$$B_z = B_0 + \frac{\partial B_z}{\partial x}x \equiv B_0 + G_x x \quad \text{or} \tag{2.26}$$

$$B_z = B_0 + \frac{\partial B_z}{\partial y}y \equiv B_0 + G_y y \quad \text{or} \tag{2.27}$$

$$B_z = B_0 + \frac{\partial B_z}{\partial z}z \equiv B_0 + G_z z, \quad \text{in general} \quad B_z = B_0 + \boldsymbol{Gr}. \tag{2.28}$$

Due to the inhomogeneous field Eqs. (2.12)ff have to be applied locally for "macroscopic magnetization" $\boldsymbol{M}(\boldsymbol{r})$ in the volume element $\mathrm{d}V$. The volume element has to be small enough to consider $\boldsymbol{B}(\boldsymbol{r})$ as homogeneous within it. "Macroscopic" signifies that the number $\mathrm{d}N_{\mathrm{S}}$ of observed spins is large enough for a meaningful averaging according to the Boltzmann distribution in (2.11). As example a cubical water sample with a volume V of one milliliter and a mass of one gram is considered. Given the molar mass of 18 g/mol this corresponds to 0.056 mol water molecules and 0.111 mol hydrogen nuclei, respectively. Even if the cube is divided into 10^9 volume elements $\mathrm{d}V$ with 10 micrometer length of side, each volume element still contains $\mathrm{d}N_{\mathrm{S}} = 6.7 \times 10^{13}$ ^{1}H nuclei, with $\mathcal{N}_{\mathrm{A}} = 6.022 \times 10^{23}\,\mathrm{mol}^{-1}$ for the Avogadro number. Introducing the local spin density

$$\rho(\boldsymbol{r}) = \mathrm{d}N_{\mathrm{S}}(\boldsymbol{r})/\mathrm{d}V \tag{2.29}$$

and the z component of the Boltzmann-averaged nuclear magnetic dipole

$$\langle \mu_z \rangle = \frac{\gamma^2 I(I+1)\hbar^2}{3kT} B_0. \tag{2.30}$$

Curie's law can be formulated locally as[9]

$$M_z^{\mathrm{eq}}(\boldsymbol{r}) = \rho(\boldsymbol{r}) \langle \mu_z \rangle. \tag{2.31}$$

The solution of (2.18) with the initial condition

$$\boldsymbol{M}(\boldsymbol{r}) = \rho(\boldsymbol{r}) \langle \mu_z \rangle \boldsymbol{e_x}' \tag{2.32}$$

at $t = 0$ and the additional field $(\boldsymbol{Gr})\,\boldsymbol{e}_z$ is a precession with the space- and possibly time-dependent angular velocity

$$\boldsymbol{\omega}(\boldsymbol{r}, t) = -\gamma(\boldsymbol{Gr})\,\boldsymbol{e}_z \tag{2.33}$$

around the z axis. The time-dependence applies for gradients $\boldsymbol{G}(t)$ that are a function of time. Motion of the nuclear spins that contribute to the spin density $\rho(\boldsymbol{r})$ will be treated in Sects. 2.1.7 and 2.1.8. The angle of precession is denoted as phase. It is obtained by integrating (2.33) to

$$\phi(\boldsymbol{r}, t) = -\gamma \int_0^t \boldsymbol{G}(t')\boldsymbol{r}\, \mathrm{d}t' \tag{2.34}$$

$$\equiv -\boldsymbol{k}\boldsymbol{r}. \tag{2.35}$$

In (2.35) the definition of the wave vector

$$\boldsymbol{k} = \gamma \int_0^t \boldsymbol{G}(t')\, \mathrm{d}t' \tag{2.36}$$

has been introduced.[10] The measuring system samples the integrated transverse magnetization in the observable volume V, see Sect. 2.3.4. Division by V yields for the average magnetization

$$\bar{\boldsymbol{M}}(t) = \frac{\langle \mu_z \rangle}{V} \iiint_V \rho(\boldsymbol{r}) \left[\cos(\phi(\boldsymbol{r}, t)) \boldsymbol{e_x}' + \sin(\phi(\boldsymbol{r}, t)) \boldsymbol{e_y}' \right] \mathrm{d}x\mathrm{d}y\mathrm{d}z. \tag{2.37}$$

[9] A spatial variation of $\langle \mu_z \rangle$ due to the superposition of $\boldsymbol{B_0}$ with $\boldsymbol{Gr}$ can be neglected. On the one hand the additional gradient fields are typically at least three orders of magnitude weaker than $\boldsymbol{B_0}$. On the other hand the gradient fields are usually switched on as pulses with a duration that is short compared to the longitudinal relaxation time T_1.

[10] A more general definition with the effective gradient will be given in Sects. 2.1.7 and 2.1.8. The concept of effective gradients includes the effect of rf pulses with $\omega_1 \tau = \pi$.

Nondimensionalization with $\langle\mu_z\rangle/V$ and identification of the transverse plane of the rotating frame of reference with the complex plane leads to the concise expression

$$\boxed{M^+(\boldsymbol{k}) = \iiint_V \rho(\boldsymbol{r}) \exp(-i\,\boldsymbol{k}\,\boldsymbol{r})\mathrm{d}x\mathrm{d}y\mathrm{d}z} \tag{2.38}$$

with $\mathrm{Re}(M^+) = \bar{M}_x V/\langle\mu_z\rangle$ and $\mathrm{Im}(M^+) = \bar{M}_y V/\langle\mu_z\rangle$. According to this the average transverse magnetization $M^+(\boldsymbol{k})$ is the Fourier transform of the spin density at point $\boldsymbol{k}$ in reciprocal position space.[11] Thus the sought-after spin density can be determined approximately by inverse Fourier transform if $M^+(\boldsymbol{k})$ can be suitably sampled in reciprocal position space.

With the exception of research described in Sects. 4.5 and 4.10, all applications presented in Chap. 4 use the principle of Fourier imaging. The effect of small deviations from linear field variations are treated analytically for a special case in Chap. 9.

2.1.3.2 Pair of Continuous and Discrete Fourier Transform

If it were possible to sample reciprocal position space continuously and completely, the spin density could be calculated by inverse Fourier transform:

$$\rho(\boldsymbol{r}) = \frac{1}{(2\pi)^3} \iiint M^+(\boldsymbol{k}) \exp(i\,\boldsymbol{k}\,\boldsymbol{r})\mathrm{d}k_x\mathrm{d}k_y\mathrm{d}k_z. \tag{2.39}$$

This can be seen quite simply by inserting (2.38) in (2.39), which leads to the Fourier representation of the Dirac or delta function. Experimentally, neither a continuous nor an infinitely expanded sampling is possible. Usually reciprocal space is sampled on a regular Cartesian grid. In one dimension, the expression for the discrete inverse Fourier transform then reads

$$\tilde{\rho}_n = \frac{1}{N} \sum_{k=1}^{N} M^+{}_k \exp[i\,2\pi(k-1)(n-1)/N], \quad 1 \le n \le N. \tag{2.40}$$

For multidimensional data the procedure (2.40) has to be applied sequentially for all dimensions. In the expressions $\tilde{\rho}_n$ and $M^+{}_k$ the naturals n and k signify the index of the result and measured data vectors, respectively. The latter results from the discretization of e.g. k_x in (2.38). For the sake of completeness, the discrete Fourier transform is also indicated. Assuming a discrete spin density $\tilde{\rho}_n$, the expression of the measured signal would be

[11] See also problems 2.5 and 2.6.

$$\tilde{M}^{+}_{k} = \sum_{n=1}^{N} \tilde{\rho}_n \exp[-i\,2\pi(k-1)(n-1)/N], \quad 1 \le k \le N. \tag{2.41}$$

For the hypothetical discrete pair it is also rather simple to see that insertion of $\tilde{M}^{+}_{k}$ from (2.41) instead of M^{+}_{k} into (2.40) leads to the identity. The Kronecker delta occurs in place of the delta function.

Here it is necessary to examine the less simple question what the discrete inverse Fourier transform (2.40) of the measured continuous Fourier transform (2.38) signifies. To this end the discrete $\boldsymbol{k}$ values have to be expressed as a function of the index k and inserted into (2.38). Only one dimension is considered, the extension to higher dimensions gives corresponding results. In order to achieve the highest resolution with a given number of discretization points, the length L of the field of view (FOV) is chosen to just contain the sample. According to the sampling or Nyquist theorem the increment in reciprocal space is then calculated from[12]

$$k_{\text{inc}} = 2\pi/L. \tag{2.42}$$

For the fast Fourier transform (FFT) the number N of points sampled is a power of two. They are chosen as

$$\frac{2\pi}{L}(k-1-N/2), \quad 1 \le k \le N. \tag{2.43}$$

Now (2.38) can be expressed as a function of index k and inserted into (2.40):

$$\begin{aligned}\tilde{\rho}_n = \frac{1}{N}\sum_{k=1}^{N}\int_{-L/2}^{L/2} \rho(r)\exp[-i\,(2\pi/L)(k-1-N/2)r]\mathrm{d}r \\ \times \exp[i\,2\pi(k-1)(n-1)/N], \quad 1 \le n \le N.\end{aligned} \tag{2.44}$$

The integration limits are reduced assuming that no spin density is observed outside the FOV. Interchanging summation and integration as well as collection of the exponential functions lead to

$$\begin{aligned}\tilde{\rho}_n = \frac{1}{N}\int_{-L/2}^{L/2} \mathrm{d}r\,\rho(r)\sum_{k=1}^{N}\exp\left\{i\,2\pi\left[-\frac{r}{L}\left(k-1-\frac{N}{2}\right)\right.\right. \\ \left.\left.+\frac{(k-1)(n-1)}{N}\right]\right\}, \quad 1 \le n \le N.\end{aligned} \tag{2.45}$$

[12]This corresponds to the claim of unambiguous phase increments $k_{\text{inc}}r$ for all positions within the FOV. For magnetization outside the FOV the phase increment between two discretization points calculated from (2.35) and (2.42) is outside the interval $[-\pi\ \ \pi]$. This violation of the sampling theorem leads to a folding of spin density in the calculated image.

Rearranging finally yields:

$$\tilde{\rho}_n = \frac{\exp\{i(n-1)\pi\}}{N} \int_{-L/2}^{L/2} \mathrm{d}r\, \rho(r) \sum_{k=1}^{N} \exp\left\{-i2\pi\left(k-1-\frac{N}{2}\right)\left(\frac{r}{L}-\frac{n-1}{N}\right)\right\}, \quad 1 \le n \le N. \tag{2.46}$$

The first exponential is one for odd index n and minus one for even index. This corresponds to a first-order phase error, analogous to the shift theorem of the Fourier transformation. In two dimensions a checkerboard pattern is obtained. This effect can be removed by a simple phase correction. The correction of non trivial phase errors will be treated in Sect. 2.3.5. The sum in (2.46) is a superposition of sine and cosine functions. The common origin depends on the index n of the result vector, the scaling of the argument on index k of the measured data in reciprocal space. As the sum is finite, it only represents an approximation of the delta function. The position of the origin and the degree of approximation shall be illustrated for four cases in Fig. 2.3.

For $n = 1$ the origin is at zero, i.e., $\tilde{\rho}_1$ is an approximation of $\rho(0)$. In Fig. 2.3a the sum is represented for a coarse discretization of $N = 16$. Obviously not only $\rho(0)$ contributes to the real part of $\tilde{\rho}_1$, but predominantly the weighted integral of $\rho(r)$ in an interval of width $2L/N$ around $r = 0$. Additionally on each side alternately $N/4$ integrals with decreasing negative weight and $N/4 - 1$ integrals with decreasing positive weight in intervals of width L/N contribute. Although $\rho(r)$ is real, the oscillating imaginary part of the sum in general leads to a small imaginary part of $\tilde{\rho}_n$. The maximum of the real part of the sum is N times higher than the amplitude of the oscillating imaginary part.

For $n = 2$ the origin is at L/N, i.e., $\tilde{\rho}_2 \approx \rho(L/N)$. Apart from that there is a cyclic shift of the function. All N points are equidistant with the "digital resolution"

$$r_{\mathrm{inc}} = L/N = 2\pi/(Nk_{\mathrm{inc}}). \tag{2.47}$$

For $n = N/2$ the origin is such that $\tilde{\rho}_{N/2}$ is dominated by $\rho(r)$ in the vicinity of the right boundary of the FOV. Still for a rather coarse discretization of $N = 32$ the corresponding sum is shown in Fig. 2.3b.

The first point of the result vector with $n = N/2 + 1$ samples the left and right ends of the FOV in equal measure. This is demonstrated in Fig. 2.3c for $N = 64$, which depending on the application is already a suitable discretization.

Due to the cyclic shift the following points of the result vector with $N/2 + 2 \le n \le N$ sample the spin density predominantly at negative positions. This is shown in Fig. 2.3d for $N = 128$ and $n = 96$. To obtain the correct image, the halves of $\tilde{\rho}$ calculated by (2.46) are shifted.

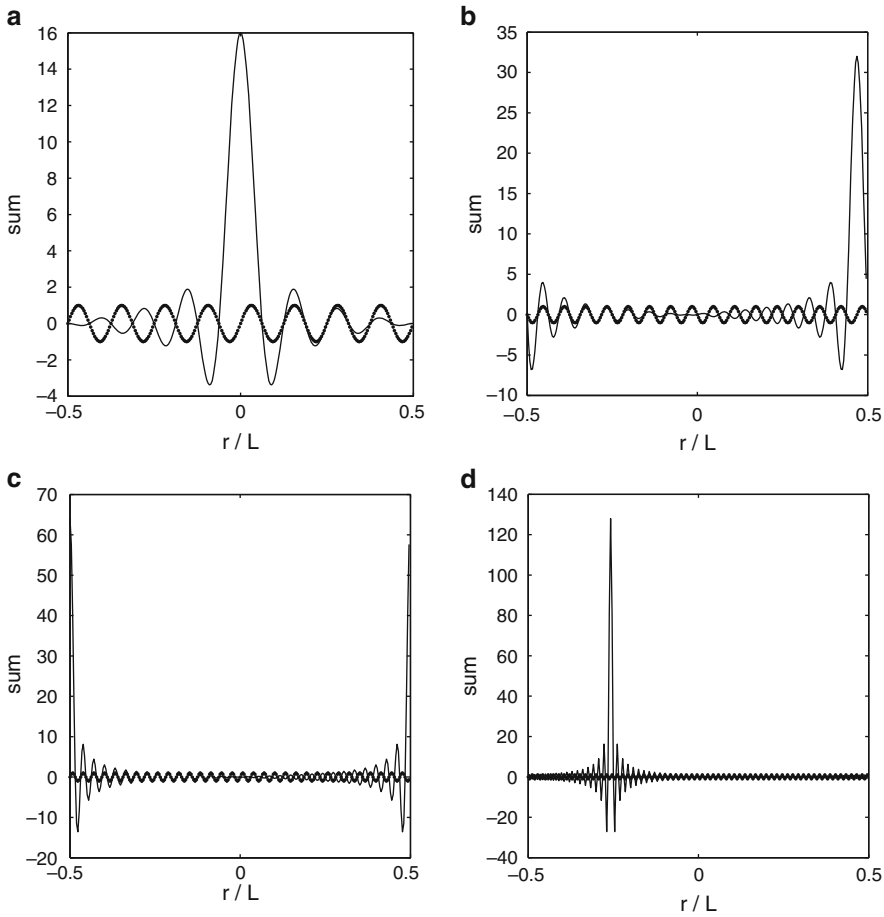

Fig. 2.3 Representation of the sum in (2.46). Real part: *solid line*, imaginary part: *dotted line*. Results for varying discretization N of the discrete Fourier transform and varying index n of the result vector are shown. (**a**) $N = 16$, $n = 1$; (**b**) $N = 32$, $n = N/2 = 16$; (**c**) $N = 64$, $n = N/2 + 1 = 33$; (**d**) $N = 128$, $n = 96 > N/2 + 1$

In summary the first point of the shifted result vector is related to both boundaries of the FOV. It is followed by $N/2 - 1$ points corresponding to negative r. The point of origin is at index $n = N/2 + 1$. Positive r are represented by the last $N/2 - 1$ points. If the sampled spin density $\rho(r)$ shows only minor variation on the length scale of the oscillations of the sum, contribution from side lobes with alternating polarity cancel and $\tilde{\rho}$ is a faithful approximation. For steep jumps in the spin density it is comprehensible from the preceding that artifacts such as the Gibbs effect can result from discrete sampling and Fourier transformation. An example for the investigation of artifacts by discrete sampling is given in Sect. 4.9.

2.1.3.3 Simple Pulse Sequence, Resolution

There are two common methods to conduct the transverse magnetization $M^+(\boldsymbol{k})$ to the required sampling points in $\boldsymbol{k}$ space.

In the method called frequency encoding the gradient in (2.36) is kept constant and is denoted as read gradient $\boldsymbol{G}_\mathrm{r}$. Data acquisition is performed with a dwell time (DW) calculated such that the chosen $k_{\alpha\,\mathrm{inc}}$ is obtained, where α designates the gradient direction. Usually α is x, y, or z but other directions can be realized by simultaneous switching of gradients. In order to conduct the first point to $-(N_\alpha/2)k_{\alpha\,\mathrm{inc}}$ a gradient with opposite polarity and corresponding time integral is applied before data acquisition, see Fig. 2.4. This gradient is denoted as read dephase gradient. Its magnitude can be higher than that of the read gradient in order to reduce its duration, the read dephase time. For $\boldsymbol{k} = 0$ the magnetization phase is independent of position and the signal is at its maximum. The maximum is denoted as gradient echo and the corresponding time as t_{GE}.

In order to sample the remaining dimensions frequency encoding can be supplemented by a method denoted as phase encoding. The phase gradient $\boldsymbol{G}_\mathrm{p}$ perpendicular to the read gradient is switched on after generation of transverse

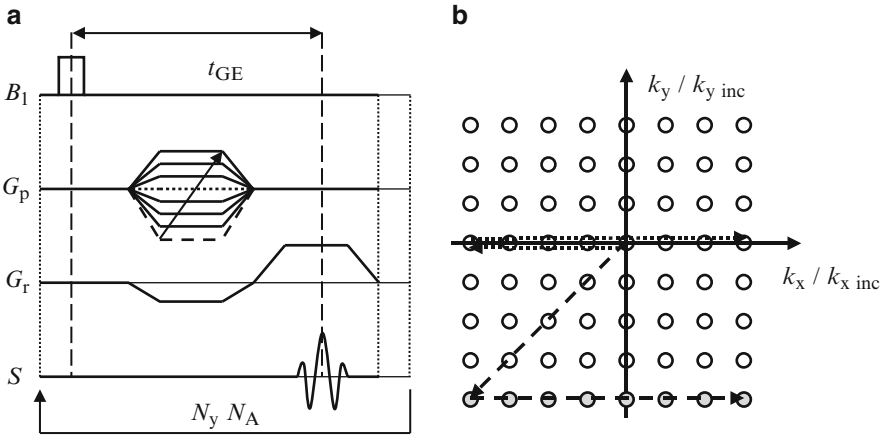

Fig. 2.4 Simple experimental scheme for the sampling of reciprocal position space. (**a**) Synchronization of excitation with B_1, phase encoding with G_p, frequency encoding with G_r, and data acquisition. (**b**) Corresponding path in $\boldsymbol{k}$ space. Just after excitation the magnetization state corresponds to the origin of $\boldsymbol{k}$ space. The simultaneous action of the phase gradient and read dephase gradient produces the straight lines to sampling points at the left border of $\boldsymbol{k}$ space. During acquisition of the signal S the read gradient leads the magnetization along horizontal lines. In the example the read gradient has x direction and the phase gradient y direction. The depicted signal is a sketch of the real part of the total observable magnetization for $G_\mathrm{p} = 0$. It exhibits a maximum at time t_GE of the gradient echo. The imaginary part, corresponding to the y component of the magnetization, is not shown. After a relaxation delay a loop is executed until the signal is acquired for all values of the phase gradient. If necessary, each acquisition can be repeated N_A times to improve SNR and reduce artifacts. [31]

magnetization and off before data acquisition, see Fig. 2.4. As rotations due to both gradients occur around the z axis the phase gradient can be applied simultaneously to the read dephase gradient. The procedure is repeated with varying amplitude of $\boldsymbol{G}_\mathrm{p}$ so that for the dimension of the phase gradient the values calculated by (2.36) and (2.43) are obtained. The remaining third dimension can be sampled by an additional phase encoding gradient.

The achievable spatial resolution and the experimental time required depend on several factors. According to (2.47) the distance between discretization points in real space equals π divided by the maximum value of the wave vector. As can be seen from (2.36) a technical limit for the resolution is thus imposed by the maximum gradient time integral that can be realized by the gradient system, see Sect. 3.1. As discussed in [13] the spatial resolution can be limited by the SNR that decreases with increasing digital resolution. Further limitations to the spatial resolution by transverse T_2 relaxation, translational self diffusion, and susceptibility artifacts are also treated in [13]. Let N_α be the number of frequency-encoding steps and N_β, N_γ the number of encoding steps in the two phase-encoded dimensions of the simple experiment described above. The duration of each frequency encoding is of the order of milliseconds and is neglected. If after each frequency encoding step the relaxation of magnetization toward thermal equilibrium is awaited, about four times the longest longitudinal relaxation time T_1 is required. In this case the experimental time amounts to

$$t_\mathrm{expt} = N_\beta N_\gamma \, 4T_1 N_\mathrm{A}, \tag{2.48}$$

where N_A designates the number of averages used to improve SNR and reduce artifacts. In favorable cases the experimental time can be drastically reduced, see e.g. [9] or [31] and Fig. 2.7.

2.1.3.4 Slice Selection

Abandoning sampling of the third dimension by phase encoding reduces the experimental time in (2.48) by the factor N_γ. Let z be the direction that is not sampled. For $G_z \equiv 0$ and thus $k_z \equiv 0$ the spin density integrated along z is obtained according to (2.38). Alternatively a slice of thickness Δz perpendicular to the z direction can be selected and a two-dimensional (2D) image of the slice produced. Slice selection by selective excitation is described in the following first in a linear approximation and then on the basis of the classical equation of motion.

According to (2.8) nuclear spins are excited by a resonant electromagnetic field if $\omega_\mathrm{rf} = \gamma B_0$ is fulfilled. If during excitation a slice gradient $\boldsymbol{G}_\mathrm{s}$ is applied along z the energy difference in (2.6) depends on z:

$$\Delta E = \gamma\hbar(B_0 + G_\mathrm{s} z). \tag{2.49}$$

In this case and for a continuous electromagnetic wave of angular frequency $\omega_{rf} = \gamma B_0$ the resonance condition would only be fulfilled at $z = 0$, producing hardly any signal. Excitation by a pulsed electromagnetic field generates not only a single frequency but also a frequency distribution around the carrier frequency. The form of the spectrum around the carrier frequency is given by the Fourier transform of the pulse shape. For a block pulse with rectangular shape a sinc spectrum is obtained, with $\mathrm{sinc}(x) = \sin(x)/x$. The pulse bandwidth $\Delta\omega$ can be defined e.g. as frequency difference between the first zeros of the spectrum on both sides of the maximum. It is inversely proportional to the duration of the pulse. Using (2.8) the approximate thickness Δz of the slice in which the resonance condition is fulfilled is calculated as:

$$\Delta\omega = \gamma G_s \Delta z. \tag{2.50}$$

A slice with sharper profile is obtained for a rf pulse with sinc amplitude shape as its frequency spectrum is rectangular. A sinc pulse truncated at the third zero of the shape on both sides of the maximum is shown in Fig. 2.5a. The corresponding

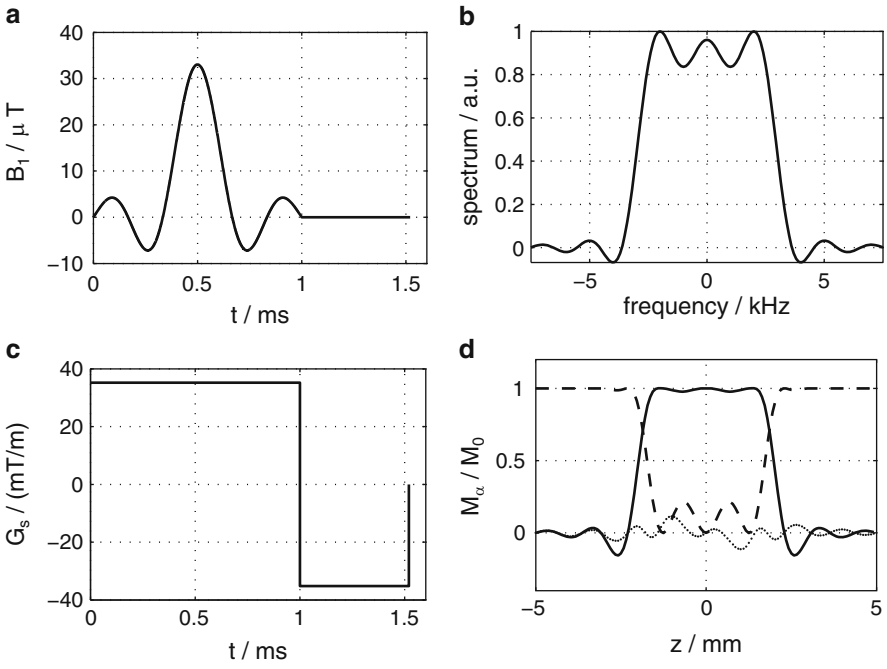

Fig. 2.5 Simulation of slice selection. (**a**) Amplitude shape of a narrow-banded sinc rf pulse. (**b**) Fourier transform of the pulse shape. (**c**) Slice gradient G_s followed by a slice-refocusing gradient. (**d**) Numerical calculation of resulting magnetization-vector components in the rotating frame of reference as a function of position perpendicular to the slice, here z. *Solid line*: x component. *Dotted line*: y component. *Dashed line*: z component. [31]

frequency spectrum is depicted in 2.5b. Deviations from a rectangular spectrum are due to the necessary truncation and represent a compromise. A description in the framework of linear systems is given in [9].

The process of slice selection can be studied accurately by numerical solution of the equation of motion (2.18). For $\boldsymbol{\omega}_{\mathrm{rf}} = \boldsymbol{\omega_0}$ and including the rf as well as gradient field it reads:

$$\frac{\mathrm{d}\boldsymbol{M}}{\mathrm{d}\,t} = \gamma \boldsymbol{M} \times \left[B_1(t)(\boldsymbol{e_x}' \cos\phi_1 + \boldsymbol{e_y}' \sin\phi_1) + (\boldsymbol{G}_{\mathrm{s}}\boldsymbol{r})\,\boldsymbol{e}_z \right]. \tag{2.51}$$

The result of a simple piecewise constant integration with 20,000 equal time steps, see Sect. 6.4,is shown in Fig. 2.5d. A typical duration of $\tau = 1$ ms was chosen for the sinc pulse. The amplitude of the rf field is calculated considering the center of the slice where the slice gradient produces no additional field. The integral of the Rabi nutation is set to the required pulse angle, here 90 degrees:

$$-\gamma \int_0^{\tau} B_1(t)\,\mathrm{d}t = \pi/2. \tag{2.52}$$

As starting point 128 points along the slice direction between −5 mm and 5 mm with constant equilibrium magnetization were chosen. The desired slice thickness was set to $\Delta z = 4$ mm. For an infinite sinc pulse with (1/6) ms between the maximum and first zero amplitude the bandwidth amounts to $\Delta\omega/(2\pi) = 6$ kHz. With the slice thickness and bandwidth the slice gradient G_{s} is calculated by (2.50). Ideal slice selection means z component zero and e.g. maximum x component within the slice. Outside the slice the situation is inverse. The remaining y component is zero at all positions. Integration up to the pulse length τ yields for the z component approximately the desired result as shown in Fig. 2.5d. Deviations from ideal slice selection exhibit features already visible in the linear approximation, see Fig. 2.5b. The transverse components however oscillate along the slice direction. Application of the slice refocusing gradient after the rf pulse, see Fig. 2.5c, produces the profiles of x and y magnetization depicted in Fig. 2.5d. The area of the optimal simulated slice refocusing gradient is −0.52 times the integral of the slice gradient. For higher flip angles such as π in Fig. 2.9 the simulation reveals larger deviations of the obtained slice thickness compared to the result of linear approximation in (2.50). Such simulations are used in the optimization of parametrized pulse shapes with respect to given properties such as sharp slice boarders without oscillation of transverse components [25].

If all rf pulses in an experiment are slice selective a pseudo 3D image can be obtained in the experimental time of a 2D image. Waiting about $4T_1$ between two phase encoding steps for each slice usually leaves enough time for the measurement of further slices. However, the achievable spatial resolution in slice direction in multi slice imaging is about one order of magnitude inferior to that of full 3D sampling of reciprocal space, e.g., 1 mm versus 100 μ m. Again, the directions of $\boldsymbol{G}_{\mathrm{r}}$, $\boldsymbol{G}_{\mathrm{p}}$, $\boldsymbol{G}_{\mathrm{s}}$ can be chosen arbitrarily through rotation, i.e., linear combinations of $\boldsymbol{G}_x$, $\boldsymbol{G}_y$, $\boldsymbol{G}_z$.

2.1.4 Contrast

2.1.4.1 Additional Dimensions

According to (2.38) the complex signal in Fourier imaging is determined by the spin density $\rho(\boldsymbol{r})$. In fact, constituting the strength of NMR, a multitude of additional parameters influence the measured NMR response. In the following Sects. frequently employed parameters are briefly reviewed. Instead of the simple 3D spin density, generally a distribution density with high dimensionality is considered:

$$M_{\boldsymbol{B}}^{+}(t) = \int_{\xi} \rho(\xi) \exp\{i\,\phi_B(t,\xi)\}\,\mathrm{d}\boldsymbol{\xi} \tag{2.53}$$

with

$$\boldsymbol{\xi} = (\boldsymbol{r}, \Omega, T_1, T_2, D, \boldsymbol{v}, \ldots). \tag{2.54}$$

In (2.54) Ω designates a frequency shift in the sense of NMR spectroscopy. It is due to the magnetic shielding σ.[13] T_1 and T_2 are the relaxation times introduced in (2.14)–(2.16). D is the translational self-diffusion coefficient.[14] The velocity in case of coherent displacement is denoted by $\boldsymbol{v}$. The phase $\phi_{\boldsymbol{B}}(t, \boldsymbol{\xi})$ in (2.53) is a function of time and parameters $\boldsymbol{\xi}$ as well as a functional of the experimentally chosen $\boldsymbol{B}(\boldsymbol{r}, t)$. For a real-valued phase as in (2.38) the integral transform is a Fourier transform. Relaxation corresponds to an imaginary phase and a Laplace transform.

Even a coarse resolution of the above distribution in ten dimensions is prohibited by the required experimental time and the amount of data. Hence the experiments integrate the distribution totally or partially over variables ($\boldsymbol{r}$ and Ω) or the influence of parameters in the form of a weighting is avoided, used, or accepted (T_1, T_2, D, and $\boldsymbol{v}$). Further notes on distribution densities are given in Sect. 2.1.8 on p. 32ff.

As example, consider the pair of variables position and spectroscopic frequency. Common experiments are:

- Spectroscopic resolution and total integration of position space
- Spectroscopic resolution for a small selected volume
- Spectroscopic resolution and 2D spatial resolution within a slice
- Spectroscopic and full 3D spatial resolution
- 2D or 3D spatial resolution and total integration of the spectroscopic dimension
- 2D or 3D spatial resolution and integration of the spectroscopic dimension in a range of chemical shifts

In all combinations the influence of longitudinal relaxation can be avoided by waiting about five times the longest T_1 of the sample between two scans. Weighting

[13] More precisely the isotropic magnetic shielding, i.e., one-third of the trace of the shielding tensor, see also Sect. 2.1.5.

[14] To be replaced by the corresponding tensor in case of anisotropic diffusion, see also Sect. 2.1.7.

by transverse T_2 relaxation is reduced by minimizing the time between excitation and detection of magnetization. Signal attenuation due to translational self diffusion is avoided if no or only moderate gradients of the magnetic field are present. If convection can be suppressed the signal is not influenced by $\boldsymbol{v}$.

Another example is the variable pair transverse relaxation and translational self diffusion. If inhomogeneities of the polarizing field or the sample do not allow for spectroscopic resolution, 2D T_2-D spectra are increasingly used as valuable source of information. Without space encoding the signal is integrated over the spatial dimensions. However, the experimental setup can be designed to possess a detection volume of suitable size and shape. Spatial resolution is then possible by moving the sensor relative to the sample. For the remaining parameters the considerations given above are still valid.

In the following all distribution densities are denoted by the same symbol "ρ," even if the considered distribution results from an integration over some parameters. To be mathematically correct, a new symbol would have to be introduced in each case.

2.1.5 Spectroscopy

The surrounding electron density causes a shielding of the polarizing field at the positions of the nuclei. For different chemical groups this chemical shielding has slightly different values.[15] In the simplest case NMR spectroscopy consists of a pulse excitation followed by a free induction decay (FID). The broad-banded rf pulse rotates the nuclear magnetization of the observed kind (e.g. ^{1}H or ^{13}C) in the transverse plane, see (2.24). The pulse response is sampled and a frequency analysis performed by Fourier transformation. During the FID the magnetic field in (2.18) amounts to $(1-\sigma)B_0$ for a given magnetic shielding σ. Consequently a residual precession with angular velocity $\Omega = -\sigma\omega_0$ remains in the rotating frame, similar to the situation in (2.33). Integrating over the observed sample, i.e., the occurring residual frequencies, the nondimensionalized magnetization reads

$$M^+(t) = \int_{-\infty}^{\infty} \rho(\Omega)\exp(i\,\Omega t)\mathrm{d}\Omega \tag{2.55}$$

similar to the expression in (2.38). Here, the total transverse magnetization $M^+(t)$ and the spectrum $\rho(\Omega)$ form a Fourier pair.[16] According to (2.55) the magnetization at time $t = 0$ reflects the integral of the observed spectrum. This still holds if the signal decays by transverse relaxation to be discussed in Sect. 2.1.6. Signal decay

[15] In the range of 10 ppm (parts per million) for hydrogen nuclei, 200 ppm for the NMR-observable carbon isotope ^{13}C.

[16] The angular frequency has been used as variable. In spectroscopy it is common to use the chemical shift δ relative to a reference: $\delta = 10^6(\sigma_{\mathrm{ref}} - \sigma)/(1-\sigma_{\mathrm{ref}}) \approx 10^6(\sigma_{\mathrm{ref}} - \sigma)$.

by relaxation results in a peak height-reduction and broadening in the measured spectrum. Nevertheless, following from the Fourier relation, the integral of the measured spectrum is directly related to the magnetization at $t = 0$ and hence the number of spins. By linearity of the Fourier transform the direct relation between the peak integral and the number of spins of the corresponding chemical group holds for the spectrum of superposed lines with chemical shift.[17] In favorable cases this experiment is sufficient to analyze which chemical groups are present and in which number. The fine structure by through-bond coupling is not to be discussed here. It should simply be mentioned that this additional information is used to determine the primary structure. The secondary structure e.g. in solution can be assessed by measurement of dipolar through-space coupling. By this, NMR is one of the most important analysis tools in chemistry and biochemistry.

Broadening, overlap and artifacts hamper the inference from the measured spectrum on the true spectrum. One strategy in the analysis of spectra is a fit of the weighted superposition of parametrized lines to the measured spectrum. Ideally the parametrized line shape should be physically motivated. In spectroscopy the symmetric Voigt profile is popular. It is the convolution of a Lorentzian line resulting from monoexponential relaxation and a Gaussian line accounting for a statistical broadening. Analysis with a pseudo Voigt function[18] have been conducted on severely distorted spectra with a largely automated program [43]. In order to account for the frequently asymmetric line shape, a new physically motivated line-shape function was derived, see Chap. 7.

An application exploiting the temperature dependence of chemical shielding in water is presented in Sect. 4.9. In the diffusion measurements described in Sect. 4.10, spectroscopic resolution is used to differentiate between the phases of an emulsion.

2.1.6 Relaxometry

In the following the three variables spectroscopic frequency ω, transverse relaxation time T_2, and longitudinal relaxation time T_1 are jointly considered. Including these parameters the rotating frame equations (2.19)–(2.21) read:

$$\frac{\mathrm{d}M_x}{\mathrm{d}t} = -\Omega M_y - \frac{M_x}{T_2^*} \tag{2.56}$$

$$\frac{\mathrm{d}M_y}{\mathrm{d}t} = \Omega M_x - \frac{M_y}{T_2^*} \tag{2.57}$$

$$\frac{\mathrm{d}M_z}{\mathrm{d}t} = -\frac{M_z - M_z^{\mathrm{eq}}}{T_1}. \tag{2.58}$$

[17] In contrast e.g. to infrared spectroscopy, where band integrals are influenced by further parameters.

[18] There is no closed analytical expression for the convolution.

After the excitation pulse again a FID is obtained, i.e., no rf or gradient fields are applied. It is assumed that $\omega_{\mathrm{rf}} = \omega_0 = -\gamma B_0$ holds. As in (2.55) Ω designates the product $\gamma B_0 \sigma$. The effective transverse relaxation time is denoted by T_2^*. It is shorter than the natural relaxation time T_2 if inhomogeneities of the polarizing field lead to a dephasing of magnetization. Using the symbol T_2^+ for this relaxation time due to inhomogeneous broadening, the relation

$$\frac{1}{T_2^*} = \frac{1}{T_2} + \frac{1}{T_2^+} \tag{2.59}$$

holds for additive relaxation rates [22].

Without rf fields (2.58) is decoupled from (2.56) and (2.57). However, the time evolution of M_z influences the initial condition of transverse magnetization if the time t_{R} between two excitations is insufficient for return to thermal equilibrium. Here it is assumed that each excitation totally converts longitudinal to transverse x magnetization that decays to zero before the next excitation. Longitudinal magnetization builds up during the time interval t_{R}. Starting the time axis after the excitation the solution of (2.56) and (2.57) reads

$$M^+(t, t_{\mathrm{R}}) = M_z^{\mathrm{eq}}(1 - \exp(-t_{\mathrm{R}}/T_1)) \exp(i\,\Omega t) \exp(-t/T_2^*). \tag{2.60}$$

With the spatially integrated density $\rho(\Omega, T_1, T_2^*)$ (2.55) is extended to

$$\begin{aligned} M^+(t, t_{\mathrm{R}}) = &\int_{-\infty}^{\infty} \mathrm{d}\Omega \int_0^{\infty} \mathrm{d}T_1 \int_0^{\infty} \mathrm{d}T_2^* \rho(\Omega, T_1, T_2^*) \\ &\times (1 - \exp(-t_{\mathrm{R}}/T_1)) \exp(i\,\Omega t) \exp(-t/T_2^*). \end{aligned} \tag{2.61}$$

First the common case of spectroscopy with relaxation is further discussed. Let individual chemical groups with frequency shift Ω_k and relaxation times $T_{1,k}, T_{2,k}^*$ contribute with fraction ρ_k. The spin density is then expressed as

$$\rho(\Omega, T_1, T_2^*) = \sum_k \rho_k \delta(\Omega - \Omega_k) \delta(T_1 - T_{1,k}) \delta(T_2^* - T_{2,k}^*). \tag{2.62}$$

Insertion of (2.62) in (2.61) yields for the complex signal a superposition of damped oscillations as in (2.60) for a single group. Fourier transformation with respect to t can be calculated quite simply leading to the experimental spectrum

$$\begin{aligned} &\frac{1}{2\pi} \int_{-\infty}^{\infty} M^+(t, t_{\mathrm{R}}) \mathrm{e}^{-i\,\Omega t} \mathrm{d}t \\ &= \frac{1}{2\pi} \sum_k \rho_k (1 - \exp(-t_{\mathrm{R}}/T_{1,k})) \\ &\quad \left(\frac{1/T_{2,k}^*}{(1/T_{2,k}^*)^2 + (\Omega_k - \Omega)^2} + i \frac{\Omega_k - \Omega}{(1/T_{2,k}^*)^2 + (\Omega_k - \Omega)^2} \right). \end{aligned} \tag{2.63}$$

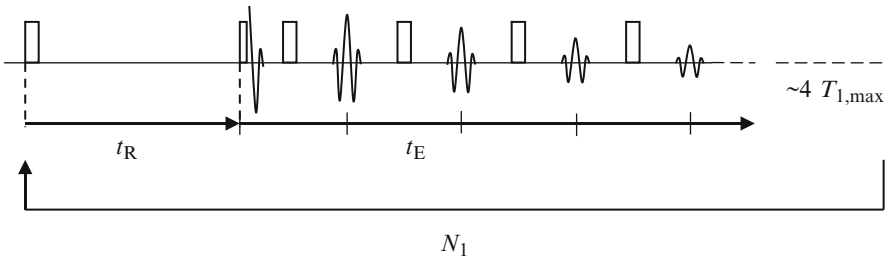

Fig. 2.6 Inversion recovery pulse sequence with CPMG detection for the determination of T_1–T_2 distributions. The first rf pulse with flip angle π prepares the magnetization. It is inverted to the $-z$ axis. During the evolution period t_R longitudinal relaxation occurs. The following $\pi/2$ rf pulse transforms the longitudinal magnetization into precessing, i.e., detectable transverse magnetization. It decays by T_2^* relaxation which can be fast due to dephasing magnetization. Dephasing is refocused repeatedly by the train of π pulses generating a series of echoes as in the CPMG sequence (Carr-Purcell-Meiboom-Gill). The first dimension of the experiment is the recovery time t_R. This dimension is sampled by incrementing t_R for different passes of the sequence. The second dimension is the time t_E at which the echoes occur. Several thousand echoes can be observed. The third dimension is the time axis for each individual echo. Frequently, this dimension is not sampled and only the center of each spin echo is detected

In the integration it has to be regarded that the above expression for the signal only holds for $t > 0$ and zero has to be inserted for $t < 0$. This asymmetry leads to the imaginary dispersion line in the spectrum. As already mentioned on p. 24 the real part for each group is a Lorentzian line centered around Ω_k. The full line width at half maximum (FWHM) amounts to $2/T_{2,k}^*$.[19] Thus experimentally a superposition of Lorentzian distributions instead of delta distributions assumed in (2.62) is obtained. The direct relation between the line integral and the fraction of associated spins mentioned on p. 24 is expressed in the prefactor ρ_k in (2.63). The additional T_1 weighting can be avoided allowing for a sufficiently long t_R.

A second case of increasing interest is the determination of a continuous distribution of longitudinal T_1 and transverse natural T_2 relaxation times [59]. For this purpose the pulse sequence shown in Fig. 2.6 can be used. Each time it starts with fully relaxed magnetization, e.g., between two repetitions about four times the longest longitudinal relaxation time is waited. The first inversion pulse produces a flip angle of π. For this initial condition the solution of (2.58) which contains $1 - 2\exp(-t_R/T_1)$ has an additional factor 2 compared to (2.61). The second pulse with nutation angle $\pi/2$ rotates the magnetization to the transverse plane. It dephases by natural T_2 relaxation, differences in chemical shielding and inhomogeneities of the polarizing field. The following train of π pulses inverts repeatedly the sign of magnetization phase if the rotation axis is x. This generates

[19]The prefactor of a normalized Lorentzian distribution is $1/\pi$ and not $1/(2\pi)$ as in (2.63). The factor 1/2 is a consequence of the missing signal for negative times. If the distribution is expressed with the linear frequency instead of angular frequency the full width at half maximum amounts to $1/(\pi T_{2,k}^*)$.

at echo times t_E between the pulses refocused magnetization denoted as spin echo. The envelope of the spin echo series only[20] decays by the occurring natural T_2 times as contributions by chemical shielding and field inhomogeneities are refocused. The echo maximums are therefore given by

$$M^+(t_E, t_R) = \int_0^\infty dT_1 \int_0^\infty dT_2\, \rho(T_1, T_2) \times (1 - 2\exp(-t_R/T_1))\exp(-t_E/T_2). \quad (2.64)$$

In this case the relation between the measured signal and the distribution $\rho(T_1, T_2)$ is a 2D Laplace transformation and not a Fourier transformation.[21] The difficulty in the analysis of T_1-, T_2 consists in the performance of a robust 2D inverse Laplace transformation. Recently progress has been achieved by the methods described in [59].

Finally a pulse sequence for the investigation of transverse relaxation in a slice with spatial resolution is presented, see Fig. 2.7. It combines read and phase encoding, see Fig. 2.4 with slice selection, see Fig. 2.5 and CPMG (Carr-Purcell-Meiboom-Gill) detection, see Fig. 2.6. After every spin echo with frequency encoding the effect of the phase gradient is revoked by a gradient of opposite polarity. The position in $\boldsymbol{k}$ space thus corresponds to the position before the slice selective π pulse. Starting with a further π pulse the trajectory in $\boldsymbol{k}$ space can be cycled through repeatedly. If r echoes are acquired for each of the N_y phase encoding steps r slice images with incremented echo time are obtained. Transverse relaxation can be analyzed for each point in the slice. Alternatively, the phase gradient can be incremented for each echo. Only N_y/r repetitions of the sequence are required, reducing drastically the experimental time. The fast spin echo imaging is denoted as turbo spin echo or RARE (rapid acquisition with relaxation enhancement). In favorable cases $r = N_y$ can be chosen for a "single shot" image acquisition.

One application is shown in Sect. 4.2, p. 110f. A tracer is used to generate relaxation contrast. Relaxation measurements on flowing samples are discussed in Sect. 2.1.9 with results presented in Sect. 4.5. For a relaxation measurement with 3D spatial resolution, see Sect. 4.6, p. 133f.

2.1.7 Diffusometry

In the following three Sects. the consequence of displacements of the spin carrying nuclei on the detected transverse magnetization is considered. A basic experiment

[20] Neglecting translational self diffusion and experimental artifacts.

[21] Fourier transformation can be treated as special case of Laplace transformation. The latter is a special case of Fredholm integral equation of the first kind, i.e., a linear integral equation with constant integral limits and the unknown function occurring only in the integral. This general case is treated in [59].

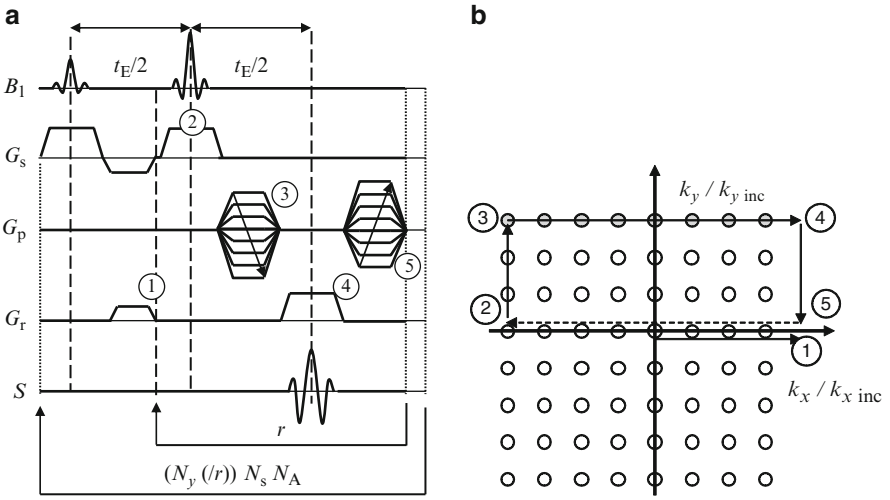

Fig. 2.7 Slice image with CPMG detection: (**a**) Pulse sequence. (**b**) Corresponding path and sampling points in $\boldsymbol{k}$ space. After excitation with B_1 and G_s the magnetization state in the selected slice corresponds to the origin of reciprocal position space. The read-dephase gradient G_r (1) leads to the point $(N_x k_{x\,inc}/2,\ 0)$. In order to reduce the echo time, the slice refocusing gradient can be applied simultaneously. The following multi echo part is executed r times. The refocusing π pulses act selectively on the excited slice and produce a reflection with respect to the origin (2). The π pulses are self refocusing, no slice refocusing gradient is required. Prior to data acquisition the phase gradient G_p takes the magnetization to the beginning of a line in $\boldsymbol{k}$ space (3). After frequency encoding (4) the action of the phase gradient is revoked by a second gradient of opposite polarity (5). After N_y passes with N_A averages r slice images with incremented echo time are obtained. Alternatively, the phase gradient can be incremented for each of the r echoes. Only N_y/r instead of N_y repetitions are necessary, considerably speeding up data acquisition ("turbo spin echo" or "rapid acquisition with relaxation enhancement, RARE"). As all rf pulses are slice selective, the sequence can be applied to N_s further sliced during relaxation of one slice ("multi slice"). For 3D spatial resolution a second phase encoding is applied instead of slice selection. [31]

for the characterization of displacements is shown in Fig. 2.8. Transverse magnetization with phase zero is created by the first rf pulse with nutation angle $\pi/2$. Neglecting chemical shielding, relaxation, and displacement during the gradient-pulse width δ, integration of (2.33) results in the magnetization phase $-\gamma \boldsymbol{G_q r}\,\delta$ at position $\boldsymbol{r}$ after the first gradient pulse, where $\boldsymbol{G_q}$ designates the amplitude and direction of the gradient pulse. As already described on p. 26 the following rf pulse with nutation angle π inverts the sign of the magnetization phase. Further integration of (2.33) until the end of the second gradient pulse yields

$$\begin{aligned}\phi(\boldsymbol{R}(\Delta), t_E) &= \gamma \boldsymbol{G_q r}\,\delta - \gamma \boldsymbol{G_q}(\boldsymbol{r} + \boldsymbol{R}(\Delta))\,\delta \\ &\equiv -\boldsymbol{q}\,\boldsymbol{R}(\Delta),\end{aligned} \tag{2.65}$$

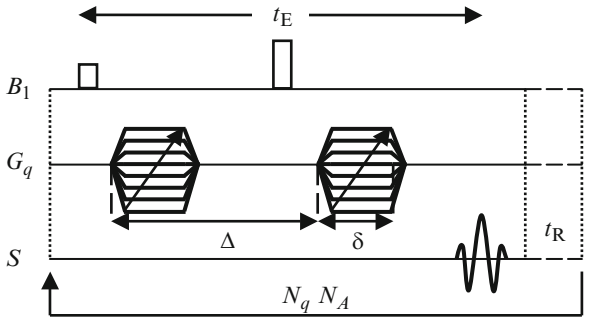

Fig. 2.8 Pulsed-Gradient Spin-Echo Sequence (PGSE). Transverse magnetization with phase zero is generated by the initial $\pi/2$ rf pulse (B_1). The first gradient pulse with amplitude G_q and duration δ creates a linear dependence of the phase to the position in direction of the gradient. A π rf pulse inverts the sign of the magnetization phase. After the observation time Δ the first gradient pulse if followed by a second pulse with identical amplitude and duration. Without displacements the magnetization helix created by the first pulse is unwound by the second pulse and a spin echo occurs at t_E. In the presence of displacements the amplitude of the spin echo is damped. A phase shift of the echo indicates coherent displacements. The displacement probability density function is usually sampled incrementing the gradient amplitude in N_q steps. N_A: number of averages. [31]

where $\boldsymbol{R}(\Delta)$ denotes the displacement during the observation time Δ. In (2.65) the definition of the reciprocal displacement vector

$$\boldsymbol{q} = \gamma \boldsymbol{G_q} \delta \tag{2.66}$$

has been introduced. Equations (2.65) and (2.66) correspond to (2.35) and (2.36), respectively, the position being replaced by the displacement. As in (2.38), the result for a distribution of displacements is expressed as

$$M^+(\boldsymbol{q}, \Delta) = \iiint \rho(\boldsymbol{R}(\Delta)) \exp(-i\boldsymbol{q}\boldsymbol{R}) \mathrm{d}R_x \mathrm{d}R_y \mathrm{d}R_z. \tag{2.67}$$

The nondimensionalized transverse magnetization is the Fourier transform of the displacement probability density function at position $\boldsymbol{q}$ in reciprocal displacement space. As in this simple experiment the starting point for the displacement is not resolved, $\rho(\boldsymbol{R}(\Delta))$ is also designated as average propagator $P(\boldsymbol{R}, \Delta)$. It can be determined approximately by inverse Fourier transform if reciprocal displacement space is suitably sampled. Concerning sampling the considerations on p. 14ff also apply for the measurement of displacements.

For unrestricted translational self diffusion the average propagator is determined by the self-diffusion coefficient D:

$$\rho(\boldsymbol{R}(\Delta)) = (4\pi D\Delta)^{-3/2} \exp(-\boldsymbol{R}^2/(4D\Delta)). \tag{2.68}$$

Inserting this propagator in (2.67) for only one gradient direction yields for the signal

$$M^{+}(q, \Delta) = M_z^{\mathrm{eq}} \exp(-q^2 D \Delta), \tag{2.69}$$

see e.g. [13].

The assumption in (2.65) and (2.67) that displacements during the gradient pulses can be neglected ("narrow-pulse approximation") can be inaccurate. For self diffusion the Bloch equations (2.14)–(2.16) have been extended by Torrey [65]. In [40] the solution without relaxation is given:

$$\ln(M^{+}(t)/M_z^{\mathrm{eq}}) = -D\gamma^2 \int_0^t \left(\int_0^{t'} \tilde{G}_q(t'')\mathrm{d}t'' \right)^2 \mathrm{d}t'. \tag{2.70}$$

The effective gradient $\tilde{G}_q$ in (2.70) accounts for the influence of π rf pulses by inversion of the sign of the preceding gradient pulses. For the basic pulse sequence shown in Fig. 2.8 integration yields the equation of Stejskal and Tanner [60, 61]:

$$M^{+}(G_q, \delta, \Delta) = M_z^{\mathrm{eq}} \exp(-\gamma^2 G_q^2 \delta^2 D(\Delta - \delta/3)). \tag{2.71}$$

Further solutions for pulse sequences applied in case of short T_2 or background gradients are given by Cotts et al. [19].

For unrestricted diffusion the self-diffusion coefficient D is usually determined by a fit of (2.71) to experimental data with varying G_q and constant δ, Δ. No tracer is required. Uncertainties are in the range of percent. An application with restricted diffusion is presented in Sect. 4.10. Dependence of the measured diffusion on the observation time in a tortuous porous medium as well as in a spherical confinement is treated.

Including magnetic shielding and the three introduced relaxation times the basic experiment shown in Fig. 2.8 already leads to rather complex results. As simple case the distribution in (2.62) is extended by a contribution from natural relaxation times ($\delta(T_2 - T_{2,k})$) and diffusion ($\delta(D - D_k)$) per chemical group. Monoexponential relaxation and unrestricted diffusion are assumed. In order to study diffusion for different components of a multi-component system spectroscopic resolution can be used. To sample the diffusion dimension, the experiment is repeated with varying gradient amplitude. Each time the second half of the echo is digitized. The time axis t starts at t_{E}. Background gradients contributing to T_2^* are assumed to be insignificant for diffusion encoding. Natural T_2 relaxation is neglected compared to T_2^* relaxation during data acquisition.[22] After Fourier transform with respect to t the real part of the result then reads:

$$\mathrm{Re}\left(\int_{-\infty}^{\infty} M^{+}(t, t_{\mathrm{E}}, t_{\mathrm{R}}, G_q, \delta, \Delta) \mathrm{e}^{-i\Omega t} \mathrm{d}t \right)$$

[22] Condition for symmetric echoes.

$$= \sum_k \rho_k (1 - \exp(-t_R/T_{1,k})) \exp(-t_E/T_{2,k})$$
$$\frac{1/T^*_{2,k}}{(1/T^*_{2,k})^2 + (\Omega_k - \Omega)^2} \exp(-\gamma^2 G_q^2 \delta^2 D_k (\Delta - \delta/3)). \tag{2.72}$$

Before diffusion coefficients can be determined by a fit of the gradient dependence a deconvolution of the spectra can be necessary.

The case of continuous distribution of diffusion coefficients and longitudinal relaxation in analogy to (2.64) is treated e.g. in [38].

2.1.8 Velocimetry

In Sect. 2.1.7 first the measurement of displacements with the pulsed-gradient spin-echo experiment (PGSE) sequence in the "narrow-pulse approximation" was presented, see (2.67). For unrestricted self diffusion without coherent displacement the expression for the signal without this approximation was then formulated in (2.71). Here the case of coherent displacement is treated. Integration of (2.33) without the narrow-pulse approximation yields for the magnetization phase

$$\phi(t) = -\gamma \int_0^t \tilde{\boldsymbol{G}}(t')\boldsymbol{r}(t')\mathrm{d}t', \tag{2.73}$$

where $\tilde{\boldsymbol{G}}$ denotes the effective gradient introduced in (2.70). Expansion of $\boldsymbol{r}(t')$ to the linear term leads to the expression of the magnetization phase for displacements with velocity $\boldsymbol{v} = (u, v, w)$

$$\begin{aligned}\phi(t) &= -\gamma \left\{ \boldsymbol{r}(0) \int_0^t \tilde{\boldsymbol{G}}(t')\mathrm{d}t' + \boldsymbol{v} \int_0^t \tilde{\boldsymbol{G}}(t')t'\mathrm{d}t \right\} \\ &= -\gamma \tilde{\boldsymbol{m}}_0(t)\boldsymbol{r}(0) - \gamma \tilde{\boldsymbol{m}}_1(t)\boldsymbol{v},\end{aligned} \tag{2.74}$$

where $\tilde{\boldsymbol{m}}_0$ and $\tilde{\boldsymbol{m}}_1$ denote the zeroth and the first moment of the effective gradient, respectively. With the relation

$$\boldsymbol{k} = \gamma \tilde{\boldsymbol{m}}_0(t) \tag{2.75}$$

the signal without relaxation, diffusion, and chemical shielding reads

$$M^+(t) = \iiint \iiint \rho(\boldsymbol{r}, \boldsymbol{v}) \exp(-i\boldsymbol{k}\boldsymbol{r}(0)) \exp(-i\gamma \tilde{\boldsymbol{m}}_1(t)\boldsymbol{v}) \, \mathrm{d}x\mathrm{d}y\mathrm{d}z \, \mathrm{d}u\mathrm{d}v\mathrm{d}w. \tag{2.76}$$

Thus the spin density $\rho(\boldsymbol{r}, \boldsymbol{v})$ with respect to the parameters position and velocity can in principle be determined by inverse Fourier transformation of the measured signal if the 6D reciprocal space is suitably sampled. In the following measurements of

velocity without and with spatial resolution are presented. Finally the influence of gradient imperfections is discussed.

2.1.8.1 Velocity Probability Density Function

As simplest case the experiment shown in Fig. 2.8 is treated for the case of perfect gradients and time-independent velocity field. During data acquisition the reciprocal position vector $\boldsymbol{k}$ calculated with the effective gradient is zero. With the definition of the velocity probability density function (VPDF)

$$f(\boldsymbol{v}) = \iiint \rho(\boldsymbol{r}, \boldsymbol{v}) \mathrm{d}x \mathrm{d}y \mathrm{d}z \tag{2.77}$$

equation (2.76) reduces to

$$M^{+}(t_{\mathrm{E}}, \boldsymbol{q}_v) = \iiint f(\boldsymbol{v}) \exp(-i\,\boldsymbol{q}_v \boldsymbol{v})\, \mathrm{d}u \mathrm{d}v \mathrm{d}w, \tag{2.78}$$

where the reciprocal velocity vector $\boldsymbol{q}_v = \gamma \tilde{\boldsymbol{m}}_1(t_{\mathrm{E}})$ has been introduced. The time point t_{E} for data acquisition in (2.78) refers to the situation where an echo is observed due to field inhomogeneities or chemical shielding. For the PGSE experiment the calculation of the first moment of the effective gradient yields for the reciprocal velocity vector $\boldsymbol{q}_v = \gamma \boldsymbol{G}_{\boldsymbol{q}} \delta \Delta$. It is related to the reciprocal displacement vector in the narrow-pulse approximation (2.66) by $\boldsymbol{q}_v = \boldsymbol{q} \Delta$. The VPDF is obtained by discrete inverse Fourier transform of the data sampled by a variation of $\boldsymbol{G}_{\boldsymbol{q}}$.

In terms of probabilities $\rho(\boldsymbol{r}, \boldsymbol{v})$ can be denoted as joint probability with $\rho(\boldsymbol{r} \cap \boldsymbol{v})$ as alternative symbol. Probability density is insofar incorrect as the integral e.g. in (2.76) is not unity but the total number of observed spins N_{S}. The function $f(\boldsymbol{v})$ in (2.77) is a 3D marginal probability obtained by integration over x, y, and z. In the following also the cases "conditional probability" and "independent probabilities" occur. Distribution here denotes the distribution density per infinitesimal interval. The integral or sum in the discrete case up to a given value of the variable is denoted as cumulative distribution.

An application of VPDF measurement in symmetric capillary flow to rheometry is presented in Sect. 4.4 on p. 115ff.

2.1.8.2 Position and Velocity Distribution

A simple pulse sequence for sampling of position and velocity space is shown in Fig. 2.9, see also [52]. The first rf pulse generates transverse magnetization with phase zero in the entire coil. As in Fig. 2.8 the first gradient pulse of the pair for velocity encoding follows. The subsequent π rf pulse is slice selective, see p. 19. It refocuses evolution due to field inhomogeneities and chemical shielding.

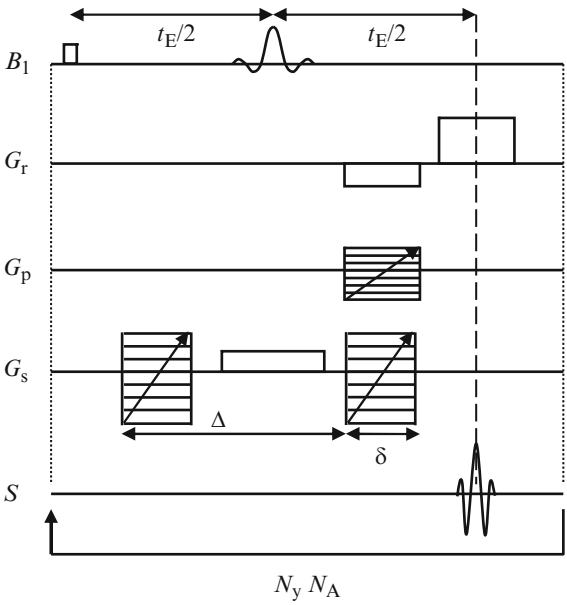

Fig. 2.9 Simple pulse sequence for the measurement of the velocity component perpendicular to an imaged slice, see also [52]

Note that the slice selective π rf pulse requires no slice-refocusing gradient as the excitation pulse in Fig. 2.5. Gradients for velocity encoding and slice selection have the same direction so the velocity component perpendicular to the observed slice is sampled. The result is integrated over the remaining velocity components. The second velocity-encoding gradient acts as described for the PGSE experiment within the observed slice. Outside the slice both gradients of the PGSE pair cause rotations in the same sense and the magnetization is spoiled. Simultaneously to the second velocity-encoding gradient a phase gradient G_p and read-dephase gradient G_r are applied as in Fig. 2.4a. Finally the total transverse magnetization is sampled under the action of a read gradient. The experiment is designed to allow for a short echo time t_E. This is advantageous if the velocity of a spin is not constant in time. In addition it allows the measurement on systems with relatively short transverse relaxation time T_2. An example is given in [52] where the velocity of SF_6 gas was measured. The ^{19}F nuclei were observed. This is possible with reasonable SNR, especially if SF_6 is used under pressure. Drawbacks of the pulse sequence are that only the velocity component perpendicular to the slice can be measured and that no "flow compensation" of space encoding is present. This means that the first moment of the slice, phase, and read gradient are not zero during data acquisition. Thus, depending on velocity, deviations from the sampling of reciprocal position space represented in Fig. 2.4b occur. On the other hand, deviations are minimized by the application of these gradients immediately before data acquisition.

One of the first pulse sequences for velocity imaging is described in [50]. It consists of only one rf pulse and is able to detect all three velocity components. In [9] an experiment with flow compensated slice and phase gradient is explained.

The read gradient is also flow compensated at time t_E, of course not for the entire acquisition time. Further methods for the phase encoding of velocity are presented in [13]. Selection of the best pulse sequence for the system under investigation requires a deeper understanding of the NMR methods.

The experimental time can be reduced drastically if the spatial resolution is assumed to be sufficiently high so that at each point in position space only one velocity is present. Following [41] the marginal spin density in position space is denoted as $\rho(\boldsymbol{r})$ and $p(\boldsymbol{v}|\boldsymbol{r})$ denotes the conditional probability that spins at position $\boldsymbol{r}$ have velocity $\boldsymbol{v}$. The above assumption signifies

$$\begin{aligned}\rho(\boldsymbol{r},\boldsymbol{v}) &= \rho(\boldsymbol{r})\,p(\boldsymbol{v}|\boldsymbol{r}) \\ &= \rho(\boldsymbol{r})\delta(\boldsymbol{v}-\boldsymbol{v}(\boldsymbol{r})).\end{aligned} \tag{2.79}$$

Insertion into (2.76) results in

$$M^{+}(t) = \iiint \rho(\boldsymbol{r}) \exp(-i\,\boldsymbol{k}\boldsymbol{r}(0)) \exp(-i\,\boldsymbol{q}_v\boldsymbol{v}(\boldsymbol{r}))\,\mathrm{d}x\mathrm{d}y\mathrm{d}z. \tag{2.80}$$

Fourier transformation with respect to position space yields $\rho(\boldsymbol{r})\exp(-i\,\boldsymbol{q}_v\boldsymbol{v}(\boldsymbol{r}))$. The magnitude of this complex image is the marginal spin density in position space. If the product $\boldsymbol{q}_v\boldsymbol{v}(\boldsymbol{r})$ is within the range $[-\pi\ \pi[$ velocity is unequivocally related to image phase. Instead of sampling reciprocal velocity space, first a reference image without velocity encoding is acquired. For each velocity component, a single image with encoding in the respective direction is sufficient for the calculation of the velocity field from the phase difference. Due to imperfections, a phase difference can occur experimentally even for velocity zero. In this case the image with velocity encoding without flow can be used as phase-reference image [52]. An application of this method is shown in Fig. 4.27, p. 139.

2.1.8.3 Influence of Gradient Imperfections

Up to here ideal gradient pulses and a homogeneous static field have been assumed. This is a good approximation for the presented measurements conducted in the high field tomograph. The static field is homogenized by superconducting and adjustable resistive coils to the ppm range and better. Gradient coils are also sophisticated and actively shielded. Transient effects by eddy currents are minimized. Persisting effects after gradient pulses are not observed.

However, for measurements in permanent-magnet systems as described in Sect. 4.4, p. 115ff, important effects occur. Calculations for static samples are presented in Chap. 8. Here the influence on the VPDF measurement is treated. As explained in Chap. 8.1 it is assumed that the dominant effects can be represented by background gradients.[23]

[23] That is unintended gradients by eddy currents or remanent changes of the permanent-magnet system that act in the "background."

A fully developed laminar, isothermal, and macroscopically homogeneous flow through a cylindrical tube is considered. Choosing the tube axis as z axis only the radially varying w component of velocity is non-zero. To measure the VPDF of w only gradients in z direction are required. Thus the moments in (2.74) are scalar functions. For the sake of simplicity the direction z is not written as index. Equation (2.76) simplifies to

$$M^+(t) = \iiint\iiint \rho(\boldsymbol{r},\boldsymbol{v}) \exp(-i\gamma\tilde{m}_0(t)z(0)) \exp(-i\gamma\tilde{m}_1(t)w)\,\mathrm{d}x\mathrm{d}y\mathrm{d}z\,\mathrm{d}u\mathrm{d}v\mathrm{d}w. \tag{2.81}$$

Integration over x, y, u, and v leads to the 2D marginal probability $\rho(z,w)$. A dependence of the observed spin density on z results from the axial distribution of the rf field. Again only one symbol ρ is used and variables over which the distribution is not integrated are listed as arguments. The argument of $z(0)$ is not written. As velocity in the tube flow depends on x and y but not on z it holds

$$\begin{aligned}\rho(z,w) &= \rho(z)\,p(w|z)\\ &= \rho(z)\,p(w)\\ &\equiv \rho(z)\,f(w).\end{aligned} \tag{2.82}$$

In (2.77) $f(\boldsymbol{v})$ is normalized to the total number of observed spins. If in the above equation $\rho(z)$ is normalized to the total number of observed spins, $f(w) \equiv p(w)$ is normalized to one. Given the independence of the distributions $\rho(z)$ and $f(w)$ the integral in (2.81) can be simplified to the product

$$M^+(t) = \int \mathrm{d}z\rho(z)\exp(-i\gamma\tilde{m}_0(t)z)\int \mathrm{d}w\,f(w)\exp(-i\gamma\tilde{m}_1(t)w). \tag{2.83}$$

In contrast to (2.78) it is not assumed that the zeroth moment vanishes as for the ideal sequence in Fig. 2.8. If permanent and transient effects as described in Sect. 8.4.1 are not compensated as explained in Sect. 8.4.2, the effects can be studied using a simple model for the gradient imperfections, the spatial spin density, and VPDF.

Regarding the permanent effects a constant gradient G_p acting in the background from excitation to detection is assumed. A permanent gradient is a remanent gradient that persists after a switched gradient pulse until it possibly gets altered by a subsequent switched gradient pulse. The existence of a permanent gradient is obvious if imaging by frequency encoding is possible without switched gradient. Concerning the dependence of the permanent-gradient amplitude on the amplitude of the previously switched gradients a marked hysteresis was observed. In general for different steps of displacement encoding different permanent gradients act. A reproducible situation can be achieved by steady-state methods, see Figs. 4.11 and 8.2. Transient effects are described as an additional amplitude contribution G_m for the

second gradient pulse, see Sect. 8.4.3. The direction of the permanent and transient gradients is the same as that of the switched gradients, here z.

The spin density detected by an ideal coil is a constant ρ within the length of the coil from $z = -a/2$ to $z = a/2$ and zero outside the coil. This corresponds to a rectangular rf profile. For the VPDF a parabolic velocity profile is assumed. This also corresponds to a constant value $1/w_\mathrm{m}$ from velocity zero to the maximum velocity w_m. Inserting these assumptions concerning the distributions and gradient imperfections into (2.83) the expression

$$M^+(t) = a\rho\,\mathrm{sinc}\left(\gamma\tilde{m}_0\frac{a}{2}\right)\left[\mathrm{sinc}(\gamma\tilde{m}_1 w_\mathrm{m}) + \frac{i\,(\cos(\gamma\tilde{m}_1 w_\mathrm{m}) - 1)}{\gamma\tilde{m}_1 w_\mathrm{m}}\right] \tag{2.84}$$

with

$$\tilde{m}_0(t) = G_\mathrm{p}(t - t_\mathrm{E}) + G_\mathrm{m}\delta \tag{2.85}$$

and

$$\tilde{m}_1(t) = \frac{1}{2}\left(G_\mathrm{p}(t^2 - t_\mathrm{E}^2/2) + G_\mathrm{m}\delta(\delta + t_\mathrm{E}) + \hat{G}\delta t_\mathrm{E}\right) \tag{2.86}$$

is obtained for the signal. In (2.84) "sinc" denotes the sine function divided by its argument. The amplitude of the ideal gradient pulse is denoted in (2.86) as $\hat{G}$. In (2.86) it has been assumed that the gradient pulses immediately follow the rf pulses what usually is the case in the experiment.

The influence of gradient imperfections on the magnetization dynamics described in (2.84)–(2.86) is shown in Fig. 2.10 for typical experimental parameters. In Fig. 2.11 the resulting distortion of the VPDF is depicted. The length of the rectangular rf profile was set to $a = 40\,\mathrm{mm}$ and $\rho = 1/a$. A maximum velocity of $w_\mathrm{m} = 10\,\mathrm{mm/s}$ was chosen. An echo time of $t_\mathrm{E} = 28\,\mathrm{ms}$ and gradient-pulse duration of $\delta = 3\,\mathrm{ms}$ was used. Four times the maximum velocity was taken as field of flow. For 128 flow-encoding steps the resulting maximum amplitude of the pulsed gradient is $0.9\,\mathrm{T/m}$.

Figure 2.10 shows the real part of the signal for four situations. The ideal situation without permanent and transient effects is depicted in Fig. 2.10a. It is approximately realized in a high-field tomograph or in the permanent-magnet system using the compensated pulse sequence of Fig. 8.2. The calculated signal for the permanent-magnet system without any compensation is shown in Fig. 2.10b. Transient effects resulting in a gradient mismatch prevent the formation of a complete echo. In Fig. 2.10c only this effect is included. As transient effects increase with increasing amplitude of the pulsed gradient this corresponds to a low-pass filter in the sampling of the VPDF, see also Fig. 2.11c. The permanent gradient additionally included in Fig. 2.10b can cause the formation of an echo which however is shifted with respect to the spin-echo (SE) time. The width of the echo decreases with increasing magnitude of the permanent gradient. Values for the permanent gradient were obtained from a measured hysteresis curve. The transient effect was calculated from a function fitted to experimental results:

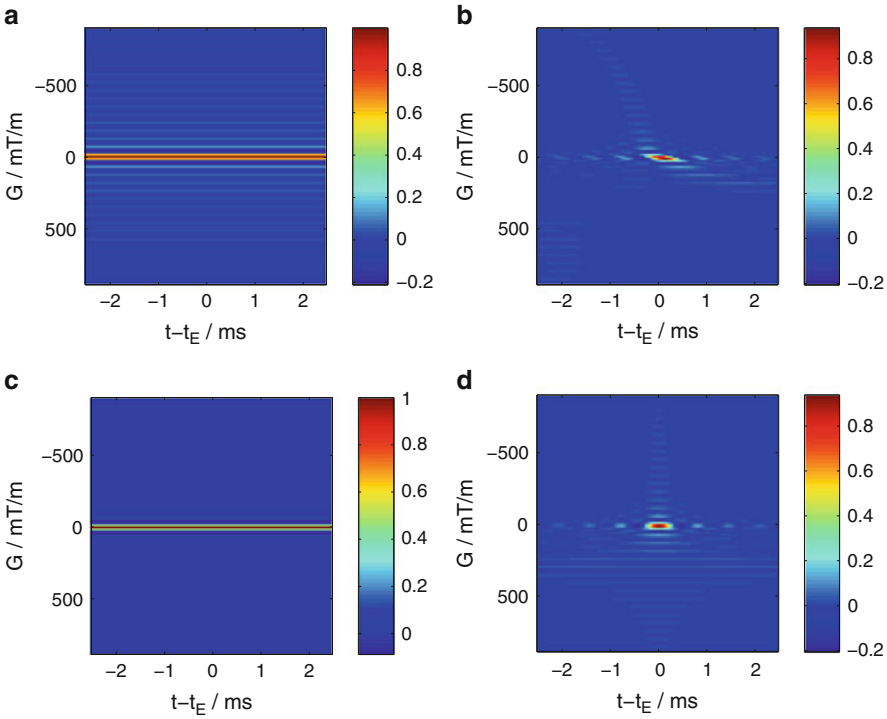

Fig. 2.10 Real part of PGSE signal for a rectangular rf profile and a Newton fluid calculated using (2.84)–(2.86) and typical experimental parameters. The four cases with and without permanent gradient G_p and gradient mismatch G_m are shown, respectively. (**a**) $G_p = G_m = 0$. (**b**) $G_p \neq 0$ and $G_m \neq 0$. (**c**) $G_p = 0$ and $G_m \neq 0$. (**d**) $G_p \neq 0$ and $G_m = 0$

$$G_{\mathrm{m}} = \mathrm{sign}(\hat{G}) \left[1 - \exp\left(-\frac{|\hat{G}|}{0.0136\,\mathrm{T/m}} \right) \right] 1.14 \times 10^{-4}\,\mathrm{T/m} + 4.91 \times 10^{-4} \hat{G}. \tag{2.87}$$

In (2.87) the sign function is plus or minus one in accordance with the sign of its argument. Figure 2.10d shows the calculated signal in the presence of the permanent gradient from the hysteresis curve without transient effects. This corresponds to the situation achieved with the steady-state sequences, See Fig. 4.11. Without gradient mismatch G_{m} the signal maximum occurs at the spin-echo time t_{E}. The width of the echo varying with the permanent gradient does not influence the velocity encoding at the echo time. However, according to (2.86) the first moments of the sampling points at t_{E} are shifted with respect to the ideal values by $G_{\mathrm{p}}(t_{\mathrm{E}}/2)^2$.

Figure 2.11 shows the VPDF calculated from the signal at time t_{E} for the data represented in Fig. 2.10. A low-pass Hamming filter was applied prior to the discrete inverse Fourier transform. It effectively reduces Gibbs artifacts without important broadening. This is evident for the ideal case shown in Fig. 2.11a. The calculated

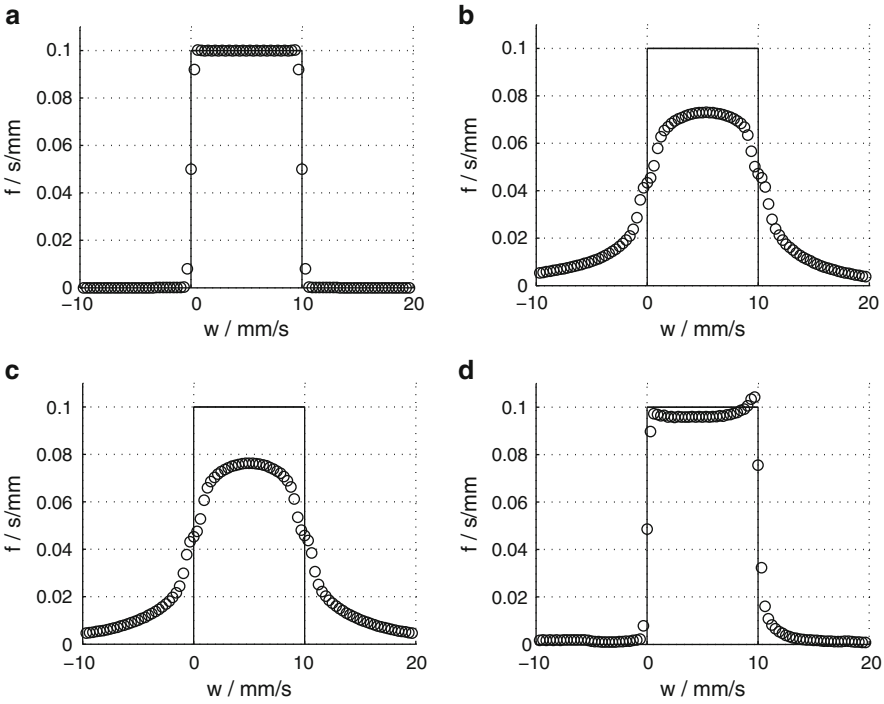

Fig. 2.11 VPDF calculated using the signals shown in Fig.2.10 at t_E. The *solid line* corresponds to the rectangular VPDF of a Newton fluid with the given maximum velocity. A Hamming filter was applied prior to the discrete inverse Fourier transform to reduce Gibbs artifacts. (**a**) $G_p = G_m = 0$. (**b**) $G_p \neq 0$ and $G_m \neq 0$. (**c**) $G_p = 0$ and $G_m \neq 0$. (**d**) $G_p \neq 0$ and $G_m = 0$

points represented by circles are in good agreement with the input VPDF plotted as solid line. In Figs. 2.11b and 2.11c the low-pass filtering by transient effects is obvious. The VPDF is significantly broadened. A difference between Fig. 2.11b with permanent gradients and Fig. 2.11c without is hardly noticeable. However, in the absence of transient effects the influence of sampling-point shifts by permanent gradients is evident in Fig. 2.11d. Besides the bending of the VPDF with a peak at the highest velocity a broadening of the high-velocity edge of the VPDF is obtained. This calculated result closely resembles the experimental result shown in Fig. 2.12 for a Newton fluid and the pulse sequence of Fig. 4.11. If the values of sampling-point shifts by permanent gradients are known, their effect can be treated by a post processing described further on.

One method for measurements in presence of gradient imperfections is presented in [12]. However, it is only suited for the study of diffusion, not of velocities. Experimentally, the generation of permanent gradients can be avoided by actively shielded gradient systems as described in Sect. 3.3.1.

2.1.8.4 Post Processing

In the inverse discrete Fourier transform it is assumed that data points are sampled on a grid of equidistant sampling points, see p. 14ff. The N ideal sampling points in reciprocal velocity space are denoted as $q_{vn} = n q_{v\,\mathrm{inc}}$ with $n = -N/2, \ldots, N/2-1$. The irregular grid resulting from a permanent-gradient hysteresis is designated by q_{vG}. Regriding aims to infer the signal $M^+(q_{vn})$ on the ideal grid from the measured $M^+(q_{vG})$. The inverse transform is then applied to the regrided data. This problem is also known in MRI, where in some methods reciprocal position space is deliberately sampled on an irregular grid [51, 54]. For a 1D VPDF the number of data points is manageable. Thus the direct method of "uniform resampling" was implemented. Its explanation in [51] starts with the inverse problem. First the data points $M^+(q_{vn})$ on the ideal grid are assumed to be known and the result $M^+(q_{vG})$ for the irregular grid to be wanted. According to the Whittaker–Shannon interpolation formula the solution is

$$M^+(q_{vG}) = \sum_n K(q_{vG} - q_{vn}) M^+(q_{vn}) \tag{2.88}$$

with the ideal sinc interpolation kernel

$$K(q) = \frac{\sin(\pi q/q_{v\,\mathrm{inc}})}{\pi q/q_{v\,\mathrm{inc}}}. \tag{2.89}$$

The interpolation formula assumes that the function M^+ is bandlimited. The inverse Fourier transform or spectrum of M^+ is the VPDF. As the spectrum is limited by zero and the maximum velocity $w_{\max}$ this condition is fulfilled. It is further assumed that the sampling interval is smaller than the inverse Nyquist rate, i.e., $q_{v\,\mathrm{inc}} < \pi/w_{\max}$ has to be ensured in the experiment.[24] The sum in (2.88) extends from $-\infty$ to ∞. Therefore it has to be finally assumed that the contribution of points outside the N points sampled in the center of q_v space can be neglected. Collecting M calculated results on an irregular grid in a vector $\boldsymbol{b}$ and the N sampled points on a regular grid in a vector $\boldsymbol{x}$, the M equations (2.88) can be represented in matrix notation:

$$\boldsymbol{b} = \boldsymbol{A}\boldsymbol{x} \quad \text{with} \quad A_{Gn} = K(q_{vG} - q_{vn}). \tag{2.90}$$

The situation in the experimental problem is inverse, i.e., $\boldsymbol{b}$ is known and $\boldsymbol{x}$ is wanted. For $M > N$ $\boldsymbol{x}$ is overdetermined. It can be optimally determined in the least-squares sense by multiplication of (2.90) with the $N \times M$ Moore-Penrose pseudo inverse of $\boldsymbol{A}$. From the singular-value decomposition (SVD) USV' of $\boldsymbol{A}$ it is calculated to $VS^{-1}U'$.

[24] The magnetization phase angle is given by $\phi = q_v w$. Thus $w_{\max}$ corresponds to an angular frequency.

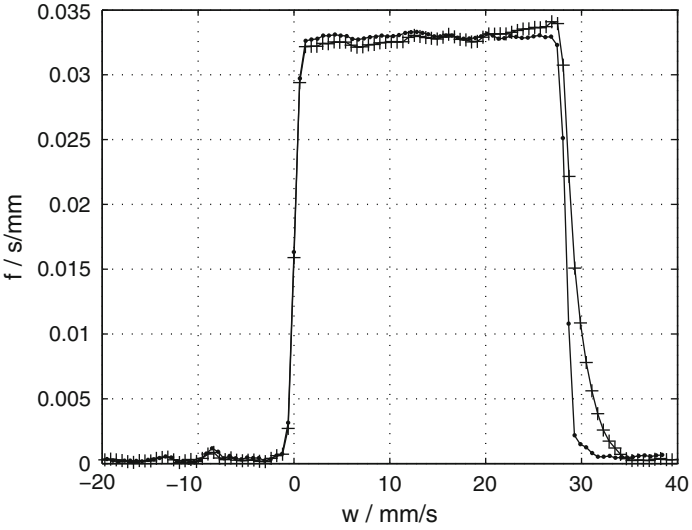

Fig. 2.12 Rectification by post processing of the VPDF measured with sampling-point shifts. Crosses represent the result of inverse Fourier transformation of data measured with the sequence shown in Fig. 4.11. Regriding of the experimental data to equidistant sampling points prior to inverse transformation leads to the improved result displayed as points. Knowledge of the permanent-gradient hysteresis in the experiment is required for regriding

Regriding requires the permanent-gradient hysteresis to be known to calculate the sampling-point positions according to (2.86). In order to obtain a stable inversion of 2.90 the number of sampled points was chosen as twice the number of calculated points for the inverse transform [51]. Thus the experimental time is doubled. The considerable improvement achieved by regriding is obvious in Fig. 2.12 showing experimental results for a Newton fluid with and without post processing, respectively.

2.1.8.5 Alternative NMR Methods

As alternative to phase encoding velocities can be measured by NMR time of flight methods. One method is to generate a line pattern of saturated magnetization that is imaged after a time which is insufficient for complete longitudinal relaxation [41]. An early method used two distinct coils for saturation and detection [30]. Another possibility is to monitor the signal decay due to outflow of excited spins from the detection volume. In contrast, a signal enhancement is obtained for unsaturated spins flowing into the observed slice (inflow) if the repetition time of an imaging sequence is short compared to the longitudinal relaxation time. An application is presented in Sect. 4.8. Phase encoding is considered to be the most accurate method of NMR velocimetry [15]. However, it has to be assured that inflow and outflow effects do

not lead to errors. In the context of inhomogeneous fields this is discussed in the following Sect. 2.1.9.

2.1.9 Relaxation for Flowing Liquids

Also relaxometry experiments without magnetic-field gradients are influenced if the sample flows through the NMR system. Early applications used the effects to monitor blood flow [57]. Considerations in the context of HPLC-NMR hyphenation can be found e.g. in [4]. However, frequently plug flow is assumed [63] and inhomogeneities of the magnetic fields are neglected or drastically simplified [66]. On the other hand, very general statements are formulated by Stepisnik [62]. In the following, expressions for quantitative description in the case of laminar pipe flow presented in Sect. 4.5 are derived. The aim is to correct the relaxometry experiment for the flow-induced effects.

The standard CPMG sequence is considered, see detection part after t_R in Fig. 2.6. It is assumed that:

1. The sample is macroscopically homogeneous
2. Diffusion and thus Taylor dispersion can be neglected
3. The signal is not attenuated by $\boldsymbol{B_0}$ inhomogeneities, i.e., homogeneous $\boldsymbol{B_0}$ or effective refocusing pulses

Due to the timing, echoes from signal excited by imperfect refocusing pulses occur at the time of subsequent refocusing pulses. First the simple case of signal decay by outflow of excited spins is treated using further assumptions. This is followed by calculations including inhomogeneous $\boldsymbol{B_0}$ and $\boldsymbol{B_1}$.

2.1.9.1 Simplest Model: Outflow of Excited Spins

In the simplest model additionally a rectangular $\boldsymbol{B_1}$ profile and homogeneously polarized spins are assumed. Immediately after ideal excitation transverse magnetization is maximum within a cylindrical pipe section of length L and zero outside. For a flow rate Q, the fraction of excited spins in the section of volume V initially decreases linearly by $(1 - Qt/V)$. The fraction decreases less than linear when also non excited spins flow out of the pipe section. With the maximum velocity $w_{\max}$ this occurs at times larger than $t = L/w_{\max}$. This is illustrated in Fig. 2.13.

Considering outflow as well as transverse relaxation with rate R_2 the signal is described by

$$M^+(t) = \int_0^\infty \int_0^{L/t} \rho_{w,R_2}(w, R_2)(1 - wt/L) \exp(-R_2 t)\, \mathrm{d}w\, \mathrm{d}R_2. \qquad (2.91)$$

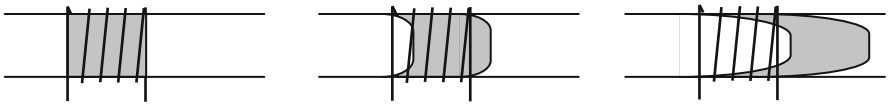

Fig. 2.13 Outflow of excited spins from a cylindrical pipe section of length L. *Left*: Excitation at time $t = 0$. *Middle*: reduction of the volume of excited spins in the pipe section linear in time for $t \leq L/w_{\max}$. *Right*: Reduction less than linear in time for $t > L/w_{\max}$

The velocity integral only extends to L/t. For higher velocities all excited spins have left the pipe section. If velocity and relaxation are not independent, the relation has to be determined for further evaluation. If however relaxation and velocity or shear rate are independent the joint distribution can be factorized into the marginal distributions and the integral into

$$M^+(t) = \int_0^{L/t} \rho_w(w)(1 - wt/L)\,\mathrm{d}w \int_0^{\infty} \rho_{R_2}(R_2)\exp(-R_2 t)\,\mathrm{d}R_2. \tag{2.92}$$

The second integral is the Laplace transform of the relaxation-rate distribution.

For velocities exceeding the maximum velocity the first integral yields one for the velocity distribution and the average velocity for its first moment:

$$M^+(t < L/w_{\max}) = (1 - \langle w\rangle t/L) \int_0^{\infty} \rho_{R_2}(R_2)\exp(-R_2 t)\,\mathrm{d}R_2. \tag{2.93}$$

The slope of the initial decrease of the signal ratio with and without flow is determined by the mean residence time $L/\langle w\rangle$. Calculations for times $t > L/w_{\max}$ require knowledge of the velocity probability-density function (VPDF). For the special case of a Newton fluid with $\rho_w(w) = 1/w_{\max}$ the integral for later times yields a hyperbolic decrease of the ratio:

$$M^+(t > L/w_{\max}) = \frac{L}{2w_{\max}} \frac{1}{t} \int_0^{\infty} \rho_{R_2}(R_2)\exp(-R_2 t)\,\mathrm{d}R_2. \tag{2.94}$$

Expanding the exponential in (2.93) for the case of a single relaxation rate R_2 leads to

$$M^+(t < L/w_{\max}) = 1 - \left(\frac{\langle w\rangle}{L} + R_2\right) t + \ldots. \tag{2.95}$$

Thus a monoexponential decay with the sum of the relaxation rate and the inverse mean residence time can be approximated for short times. This common approximation [4, 57]

$$\left(1 - \frac{\langle w\rangle}{L}\, t\right) \exp(-R_2 t) \approx \exp\left(-\left(R_2 + \frac{\langle w\rangle}{L}\right) t\right) \tag{2.96}$$

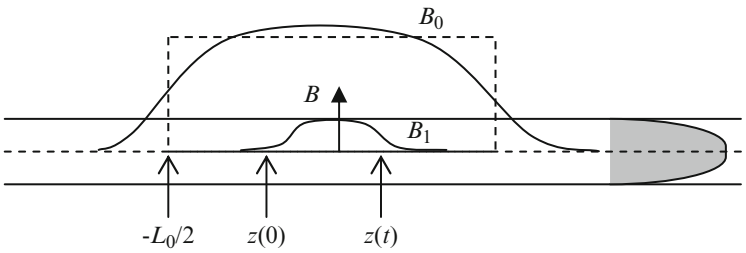

Fig. 2.14 Schematic representation of B_0 and B_1 profile and relevant z coordinates

can be transformed into $(1 - \langle w \rangle t/L) \exp(\langle w \rangle t/L) \approx 1$ to evaluate its validity. The deviation amounts e.g. to -10% for $t = 0.4\, L/\langle w \rangle$.

2.1.9.2 Calculations Including Inhomogeneous Magnetic Fields

Experimental results show that the initial decay of signal ratio is slower than predicted by (2.93). Indeed the assumption of a rectangular B_1 profile in Fig. 2.13 is a crude approximation. In the following signal calculation, the more realistic assumption is that the spatial distribution of the B_1 amplitude only depends on the z coordinate in direction of the tube axis.

According to the reciprocity theorem, see p. 68 the signal contribution of spins at coordinate z is proportional to the rf amplitude $B_1(z)$. If t is the time after excitation, spins with velocity $w(r)$ that are located at coordinate z at time t have been excited at coordinate $z - w(r)t$. Thus, in the calculation of the corresponding excited transverse magnetization, the rf field $B_1(z - w(r)t)$ has to be inserted into the expression for the nutation frequency in (2.24). Besides on the nutation angle, the excited transverse magnetization depends on the polarization of the spins at coordinate $z - w(r)t$. It is obtained by integration of (2.16) with the right-hand side consisting only of the second term. However, the equilibrium magnetization depends on $B_0(z)$ according to (2.11). In general, the relaxation time T_1 also depends on the polarizing field. As simplification it is assumed that the polarizing field has a rectangular profile from $-L_0/2$ to $L_0/2$, see schematic representation in Fig. 2.14. The duration of polarization with constant relaxation rate R_1 then amounts to $(z - w(r)t + L_0/2)/w(r)$.[25] This results in the following equation for the signal:

[25] For the case of spins with velocity w and arbitrary profiles of relaxation rate and equilibrium magnetization, the solution of the differential equation $\dot{M}_z = w(\partial M_z/\partial y) = -R_1(y)(M_z - M_z^{\mathrm{eq}}(y))$ is $M_z(y) = (1/w) \int_{-\infty}^{y} R_1(y') M_z^{\mathrm{eq}}(y') \exp\{-(1/w) \int_{y'}^{y} R_1(y'')\mathrm{d}y''\}\mathrm{d}y'$. This is obtained by solution of the homogeneous differential equation by separation of the variables and variation of the constant for the particular integral. For a constant relaxation rate R_0 and piecewise constant equilibrium magnetization, the integrals yield $M_z(y) = \exp\{-R_0 y/w\}[\sum_{i=1}^{n} M_i(\exp\{R_0 y_i/w\}$

$$M^+(t) = \int_0^\infty \int_0^\infty \int_{-\infty}^\infty \int_0^{2\pi} \int_0^\infty \rho_{r,\phi,z,R_1,R_2}(r,\phi,z,R_1,R_2)$$
$$\underbrace{(1-\exp(-R_1(z-w(r)t+L_0/2)/w(r)))}_{\text{polarization}}\ \underbrace{\sin(-\gamma B_1(z-w(r)t)\tau)}_{\text{Nutation}}$$
$$\underbrace{\exp(-R_2 t)}_{\text{relaxation}}\ \underbrace{B_1(z)/B_1(0)}_{\text{detection}}\ r\,\mathrm{d}r\,\mathrm{d}\phi\,\mathrm{d}z\,\mathrm{d}R_1\,\mathrm{d}R_2. \tag{2.97}$$

The pulse duration is denoted as τ. It is assumed that the repetition time is sufficiently long to avoid saturation effects. If as in (2.92) it is assumed that transverse relaxation is independent of velocity and the remaining variables and that this also holds for longitudinal relaxation, the signal after integration over ϕ reads

$$M^+(t) = \int_0^\infty \rho_{R_1}(R_1) \int_{-\infty}^\infty \int_0^\infty \rho_{r,z}(r,z)$$
$$(1-\exp(-R_1(z-w(r)t+L_0/2)/w(r)))\ \sin(-\gamma B_1(z-w(r)t)\tau)$$
$$B_1(z)/B_1(0)\,2\pi\,r\mathrm{d}r\,\mathrm{d}z\,\mathrm{d}R_1 \int_0^\infty \rho_{R_2}\exp(-R_2 t)\,\mathrm{d}R_2. \tag{2.98}$$

As velocity is independent of z the distribution $\rho_{r,z}(r,z)$ can also be factorized. The integration over r can be replaced by the corresponding integral over the VPDF. For a constant spin density $1/L_0$ in z direction the expression

$$M^+(t) = \int_0^\infty \rho_{R_1}(R_1) \int_0^{w_{\max}} \rho_w(w) \int_{-L_0/2}^{L_0/2} 1/L_0$$
$$(1-\exp(-R_1(z-wt+L_0/2)/w))\ \sin(-\gamma B_1(z-wt)\tau)$$
$$B_1(z)/B_1(0)\,\mathrm{d}z\,\mathrm{d}w\,\mathrm{d}R_1 \int_0^\infty \rho_{R_2}\exp(-R_2 t)\,\mathrm{d}R_2. \tag{2.99}$$

is obtained. In the case of complete polarization, $R_1(z-wt+L_0/2)/w \gg 1$, the z integral simplifies to the cross-correlation integral of $\sin(-\gamma B_1(z)\tau)$ and $B_1(z)$ with the shift $-wt$:

$$M^+(t) = \int_0^{w_{\max}} \rho_w(w)\frac{1}{L_0 B_1(0)} \int_{-L_0/2}^{L_0/2} \sin(-\gamma B_1(z-wt)\tau)\ B_1(z)\,\mathrm{d}z\,\mathrm{d}w$$
$$\int_0^\infty \rho_{R_2}(R_2)\exp(-R_2 t)\,\mathrm{d}R_2. \tag{2.100}$$

$-\exp\{R_0 y_{i-1}/w\}) + M_{n+1}(\exp\{R_0 y/w\} - \exp\{R_0 y_n/w\})]$. With a relaxation profile, numerical integration by simple time slicing yields good results.

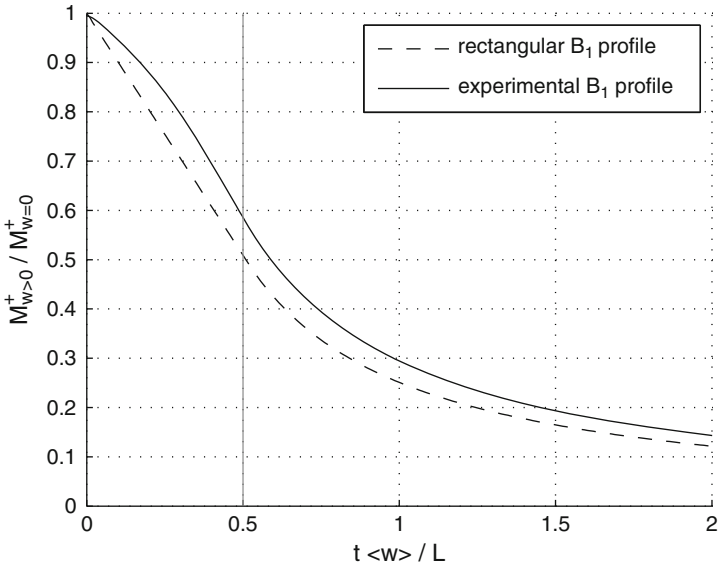

Fig. 2.15 CPMG signal with flow relative to the signal without flow for a Newton fluid according to (2.100). *Dashed line*: result for rectangular B_1 profile with a linear and a hyperbolic part. *Solid line*: Calculation with experimentally determined B_1 profile. L denotes the length of the rectangular profile and a characteristic length of the experimental profile, respectively. The CPMG signal measured with flow can be corrected by this function prior to further analysis. For non-Newtonian flow, the corresponding correction function has to be calculated with (2.100) using the actual VPDF, to be determined as described in Sect. 2.1.8

The cross-correlation integral can be calculated numerically if the B_1 profile is determined experimentally. For different velocities, the results as a function of time differ by a scaling of the abscissa. In order to perform the velocity integral numerically, the different results are interpolated to a common discretization of the time axis. For a rectangular B_1 profile triangles are obtained for the cross-correlation integral. For short times the superposition of triangles yields the previous result of (2.93). Of course also the long-time behavior of (2.94) is obtained if the constant VPDF of a Newton fluid is used in the integration. This can be seen in Fig. 2.15 where the signal calculated numerically according to (2.100) is shown for a Newton fluid and a rectangular B_1 profile. The result with an experimentally determined B_1 profile is plotted in comparison. As observed experimentally, a slower initial signal decay is obtained. This can be understood by the fact that the excitation profile with the sine function is broader than the detection profile. Thus the integrand of the cross correlation stays almost constant for small shifts. The B_1 profile was determined using frequency encoding with 128 discretization points, see discussion in Sect. 4.5. For the VPDF 64 grid points were used.

Without complete polarization the z integral in (2.99) still is a cross-correlation integral. However, the first function has the additional factor $(1 - \exp(-R_1$

$(z + L_0/2)/w)$). In this case the cross correlation not only depends on a property of the NMR system, namely the B_1 profile, but also on the longitudinal relaxation properties of the sample and the B_0 profile. If the distribution $\rho_{R_2}(R_2)$ for transverse relaxation is to be measured, it is likely that the distribution $\rho_{R_1}(R_1)$ is also unknown. Thus if possible complete polarization should be realized. For this purpose only a moderately homogeneous magnetic field is required. Alternatively a sufficient residence time of the flowing liquid in the NMR system before entry in the probe head can be realized. First experimental results are described in Sect. 4.5 on p. 125ff.

2.2 Problems

2.1. NMR Master Equation
For a magnet generating a field of $B_0 = 4.7\,\mathrm{T}$, the proton resonance frequency is indicated as $\nu = 200.13\,\mathrm{MHz}$. Calculate the gyromagnetic ratio of the proton.

2.2. Curie's Law
Show the validity of the evaluation of the sums in (2.11).

2.3. NMR Master Equation in the Context of Precession
Show that the precession with angular frequency $\boldsymbol{\omega_0} = -\gamma \boldsymbol{B_0}$ in (2.13) solves the equation of motion $\mathrm{d}\boldsymbol{M}/\mathrm{d}t = \gamma \boldsymbol{M} \times \boldsymbol{B}$ in (2.12) for a constant field $\boldsymbol{B_0}$ in z direction.

2.4. Rabi Nutation
For a micro-imaging probe connected to a 100 W RF amplifier, a realistic duration of the $\pi/2$ pulse is 12.5 μs. Calculate the Rabi frequency of nutation around $\boldsymbol{B_1}$ and the magnitude of $\boldsymbol{B_1}$.

2.5. Fourier Imaging: Example of k-Space Point for Discrete Sample
A sample is composed of twelve small water droplets at positions $(x, y) = (-25, 0)$, $(-25, 25)$, $(0, -25)$, $(0, 0)$, $(0, 25)$, $(0, 50)$, $(25, -25)$, $(25, 0)$, $(25, 25)$, $(25, 50)$, $(50, 0)$, and $(50, 25)$. Coordinates are given in mm. The four droplets in the center of the sample have twice the volume of the surrounding eight ones.

(a) Sketch the arrangement of the droplets with their initial magnetization as considered in Sect. 2.1.3, i.e., all magnetization along the x axis of the rotating frame.
(b) A gradient along x with $\gamma G_x = 3.142 \times 10^6\,\mathrm{rad\,s^{-1}m^{-1}}$ is switched on for 10 microseconds. Sketch the new rotating-frame magnetization for each droplet after this time period.
(c) Calculate the total transverse magnetization for both situations (a) and (b) in units of the small-droplet magnetization.

2.6. Fourier Imaging: Analytical Expression for a Simple Sample
Consider a cubic sample with edge length a and homogeneous spin density ρ_0.

Calculate the ideal Fourier-imaging signal according to (2.38) for the centered sample with its edges parallel to the gradient-system axes.

2.7. Slice Selection

(a) A slice of 1 mm thickness is to be selected. As in Fig. 2.5, a soft rf pulse with sinc3 amplitude shape and 1 ms duration is used. Calculate the required gradient amplitude according to the linear-response relation (2.50) using the bandwidth of the infinite sinc pulse.
(b) A parallel slice with equal thickness and a gap of 1 mm is to be selected. Calculate the corresponding shift in the rf-pulse carrier frequency if the same gradient amplitude is used.
(c) Estimate the maximum value of the B_1 amplitude for a nutation angle of $\pi/2$. How to perform the numerically exact calculation according to (2.52)?

2.8. Diffusometry vs. Velocimetry
The root-mean-square displacement by diffusion amounts to $\sqrt{2D\Delta}$ in any direction.

(a) Which result is obtained for water at ambient temperature and an observation time of $\Delta = 10\,\text{ms}$?
(b) How does this compare to the displacement during the same time in the absence of diffusion given a velocity of 1 mm/s?

2.3 Image Analysis

NMR measurements often yield huge mounds of data. Reducing this data to relevant, quantitative information can be challenging. As example, consider simple 3D spin-density imaging without sampling of further contrast dimensions. Sampling of 256 points in each dimension of reciprocal position space produces a comparatively high resolution. Discrete inverse Fourier transformation approximately yields the spin density for 256^3 grid points in real space, see (2.46). The volume element around each grid point is called voxel, in analogy to picture elements or pixels in the 2D case. If the signal magnitude at each point is mapped to 16 bits, the 16 megavoxels require 32 megabytes of memory.[26] The same amount of data is obtained for 64 points for each direction of 3D position space and 64 echoes for sampling of transverse relaxation.

In some applications the sample consists of areas with constant observable spin density and areas where no signal is observed. Nevertheless, a more or less broad

[26]The raw data before transformation requires more memory, as it consists of a real and an imaginary part. The spectrometer used always saves raw data with 32 bits, resulting in 128 megabytes in the present example.

signal-intensity distribution is observed also in these cases. One source for the distribution is signal noise. Another cause is the inhomogeneity of the B_1 field, increasing toward the boarders of the FOV. However, depending on the number of points sampled in reciprocal space, a substantial contribution to the intensity distribution results from artifacts of the discrete inverse Fourier transform, see Sect. 2.1.3, p. 14ff. In the ideal NMR image generated numerically in Fig. 2.16b only the last contribution is present. In the following, first the reduction to a binary image is discussed along with the resulting porosity as one elementary information.

2.3.1 Thresholds, Porosity, Filters

2.3.1.1 Threshold

Figure 2.16a shows a quasi continuous binary spin density $\rho(x, y)$. Insertion into (2.38) allows to calculate the ideal NMR signal $M^+(k_x, k_y)$ numerically. The resulting complex matrix is denoted as $(M^+)_{kl}$.[27] Finally, the ideal NMR image $(\tilde{\rho})_{nm}$ is calculated according to (2.40). As usual in experiments, Fig. 2.16b represents the magnitude of the complex image matrix. Concerning the benefits and challenges of phase correction, see Sect. 2.3.5. The absolute-intensity frequency distribution is obviously asymmetric around zero, see Fig. 2.16c, in contrast to the situation for a phase-corrected real-part image.

In this example without noise or experimental artifacts the spatial resolution is relatively high, about ten grid points per disc diameter. Accordingly, the frequency peaks at low and high intensities are well separated. Choosing a threshold ρ_s between the peaks, a binary image with the attributes "signal" or "no signal" is derived according to

$$\tilde{\rho}'_{nm} = \begin{cases} 1 & : \quad |\tilde{\rho}_{nm}| \geq \rho_s \\ 0 & : \quad |\tilde{\rho}_{nm}| < \rho_s \end{cases} . \tag{2.101}$$

2.3.1.2 Porosity and Threshold

If "signal" signifies pore space filled with some liquid and "no signal" solid with fast signal relaxation compared to the echo time, the porosity is calculated from the binary $N \times M$ matrix $\tilde{\rho}'_{nm}$ as

$$\varepsilon(\rho_s) = \left(\sum_n \sum_m \tilde{\rho}'_{nm} \right) (NM)^{-1}. \tag{2.102}$$

[27] There are several common notations for matrices. Here the notation $(a)_{nm}$ is used, see e.g., http://mathworld.wolfram.com/Matrix.html. More detailed notations are $(a_{nm})_{nm}$ as well as $a_{n=1\ldots N, m=1\ldots M}$. Introduction of a new symbol, such as A or $\underline{\underline{a}}$ is avoided.

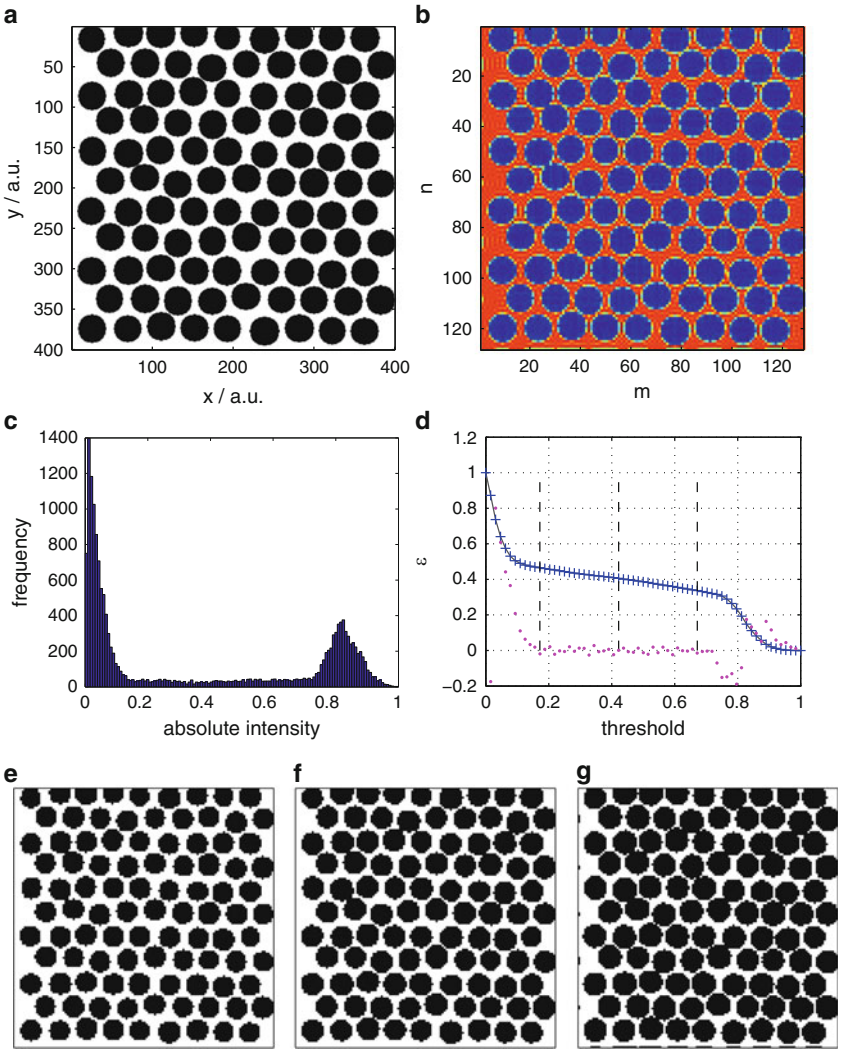

Fig. 2.16 (**a**) Two-dimensional porous structure $\rho(x, y)$ with surface porosity $\varepsilon = 0.41$. Pore space is represented by *white, solid as black*. (**b**) Numerically calculated ideal NMR image $(|\tilde{\rho}|)_{nm}$. (**c**) Frequency distribution of signal magnitude, normalized to one. (**d**) Porosity as function of threshold. Points show the discrete second derivative. The two outer broken vertical lines comprise half the intensity range, centered around the threshold corresponding to the input porosity (*broken line* in between). Binary images obtained with this three values as threshold are shown in (**e**) ($\varepsilon = 0.47$) to (**g**) ($\varepsilon = 0.34$)

This function of the threshold is shown in Fig. 2.16d for the numerically calculated ideal NMR image. Due to transformation artifacts, intensity values between the peaks occur in the intensity frequency distribution and there is no porosity plateau

between the peak intensities. If the actual porosity is known, e.g., by gravimetry, the threshold can be set such that this value is obtained. In Fig. 2.16d the surface porosity of the input structure is indicated as horizontal line and the corresponding threshold as central broken line. The binary image derived with this threshold is shown in Fig. 2.16f. However, Fig. 2.16e, g demonstrate that plausible images are also obtained with a significantly smaller respectively higher threshold, as intensities between the peaks correspond to grid points at the disc boarders. The porosities obtained are 0.47 and 0.34, respectively. One strategy for the determination of the threshold without previous knowledge is to detect the inflection point in the middle of the porosity function $\epsilon(\rho_s)$. The discrete second derivative is shown in Fig. 2.16d as points. Obviously, the strategy yields no sharp criterion in this particular example.

Applications requiring thresholds are presented in Sects. 4.6, 4.7, and 4.8. In the special case of fiber filters, see Sect. 4.1, an alternative method was adopted.

2.3.1.3 Noise

In the experiment, noise is always present in addition to transformation artifacts. Accordingly, normally distributed noise was added to the real and imaginary part of the calculated ideal NMR signal before transformation (the origin of noise and its relation to the signal is discussed in Sect. 2.3.4). Figure 2.17a shows the magnitude image for the noisy data. The impact on the signal frequency distribution can be seen in Fig. 2.17c.

As Fourier transformation is linear and white noise was added, the real and imaginary part of the transformed image also have normally distributed noise superimposed:

$$\begin{aligned} \mathrm{Re}(\tilde{\rho}_{nm}) &\to \mathrm{Re}(\tilde{\rho}_{nm}) + n_{i,nm} \\ \mathrm{Im}(\tilde{\rho}_{nm}) &\to \mathrm{Im}(\tilde{\rho}_{nm}) + n_{q,nm}. \end{aligned} \tag{2.103}$$

The normal distribution

$$P_{\mathrm{N}}(n) = \frac{1}{s\sqrt{2\pi}} \exp\left(-\frac{(n-\mu)^2}{2s^2}\right) \tag{2.104}$$

of noise has average $\mu = 0$ and a variance s^2. Index i for the real-part stands for "in-phase noise" and q for the imaginary part stands for "quadrature noise." In the following it is assumed that the signal distribution due to transformation artifacts can be neglected compared to the distribution caused by noise. In this case the signal magnitude $\sqrt{(\rho_c + n_{i,nm})^2 + n_{q,nm}^2}$ in areas with constant spin density ρ_c is distributed according to the Rice distribution,[28]

[28] Named after Stephen O. Rice.

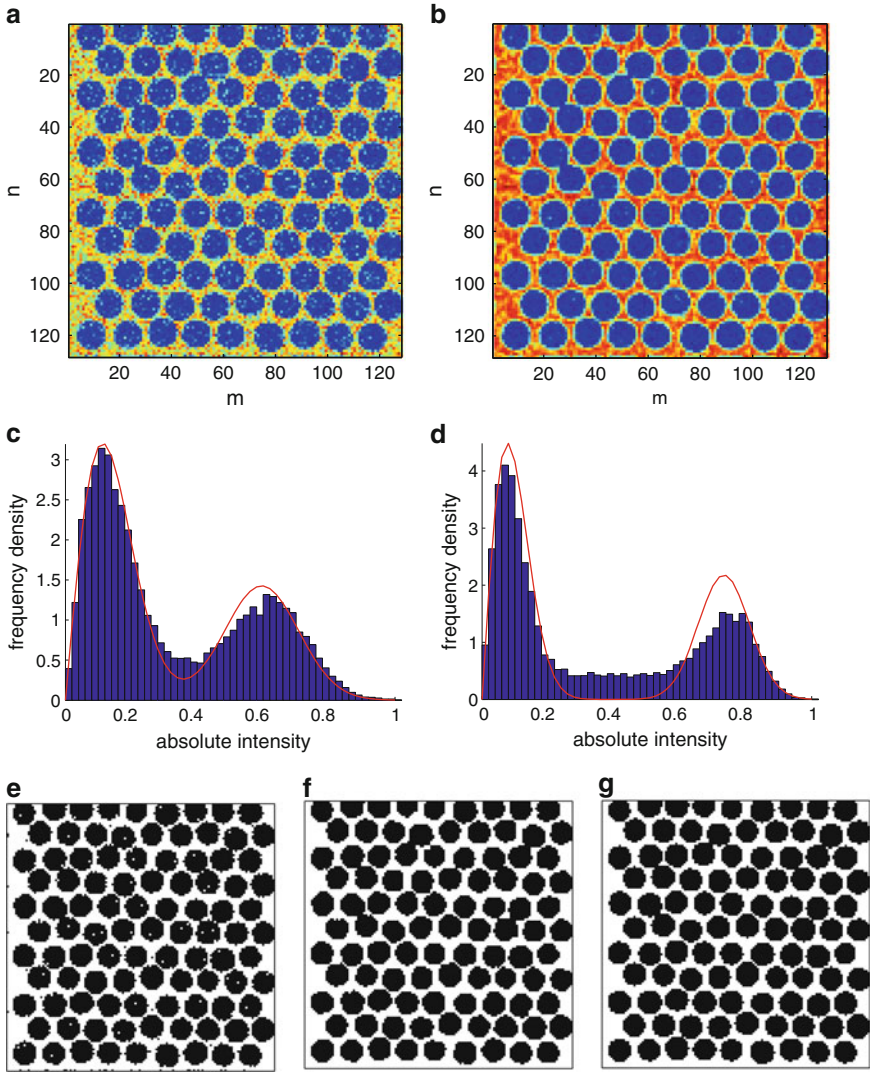

Fig. 2.17 (**a**) NMR image $(|\tilde{\rho}|)_{nm}$ for signal with superimposed noise. (**b**) NMR image $(|\tilde{\rho}_f|)_{nm}$ with low-pass filter, see (2.112). (**c**) Frequency distribution density for image (**a**) and fit of (2.107) resulting in $\varepsilon = 0.40$. (**d**) Frequency distribution density for image (**b**) and fit of (2.107) resulting in $\varepsilon = 0.42$. (**e**) Binary image derived from (**b**) with input porosity (0.41). (**f**) Application of filters (2.108) and (2.109) to image (**e**). (**g**) Binary image derived from (**b**) with input porosity (0.41)

$$P_{\mathrm{Ri}}(\tilde{\rho}) = \frac{\tilde{\rho}}{s^2} \exp\left(-\frac{\tilde{\rho}^2 + \rho_c^2}{2s^2}\right) I_0\left(\frac{\tilde{\rho}\rho_c}{s^2}\right), \tag{2.105}$$

with the modified Bessel function of the first kind and order zero I_0. In areas without observable spin density there is only statistically independent normally distributed noise in the real and imaginary part. In this case the magnitude is distributed according to the Rayleigh distribution

$$P_{\mathrm{Ra}}(\tilde{\rho}) = \frac{\tilde{\rho}}{s^2} \exp\left(-\frac{\tilde{\rho}^2}{2s^2}\right) \tag{2.106}$$

as special case of the Rice distribution. Thus in the simple case of a binary spin density and neglecting transformation artifacts, the total magnitude-signal distribution is the weighted sum of a Rayleigh and Rice distribution with the porosity as weight:

$$P_{\mathrm{ges}}(\tilde{\rho}) = \varepsilon P_{\mathrm{Ri}}(\tilde{\rho}, s, \rho_c) + (1-\varepsilon) P_{\mathrm{Ra}}(\tilde{\rho}, s). \tag{2.107}$$

Under these assumptions (2.107) can be fitted to the signal-magnitude distribution to obtain the porosity without prior knowledge.[29] The result is shown in Fig. 2.17c as solid line. The agreement for the peak at low intensity is good. Larger deviations are observed for the peak at high intensity, showing the influence of transformation artifacts. The porosity value $\varepsilon = 0.40$ obtained is in close agreement with the input value of 0.41.

2.3.1.4 Filter

Due to transformation artifacts and noise, assignments according to 2.101 can be incorrect, i.e., grid points in the pore space are set to zero instead of one and conversely grid points in the solid are set to one instead of zero. Both kinds of errors are observed in the binary image in Fig. 2.17e derived from Fig. 2.17a. If both errors compensate each other, the porosity can be correct. In Fig. 2.17e the threshold is chosen in the way that the input porosity is obtained. However, the specific surface, to be treated in Sect. 2.3.2, is heavily exaggerated for the image with erroneous spots. Likewise pore-space characteristics such as the pore-volume distribution discussed in Sect. 2.3.3 are grossly falsified.

With some prior knowledge of the imaged structures, erroneous assignments can be corrected by inspection of the surrounding grid points. If the imaged structures are known to consist of at least some connected grid points, more or less isolated grid points can be converted to the value of the surrounding grid points. Corresponding rules for a corrected copy $\tilde{\rho}''_{nm}$ of the original image, to be applied

[29] Note that for the Rice or Rayleigh distribution the parameter s^2 is not the variance of the distribution.

for each grid point, are[30]

$$\tilde{\rho}''_{nm} = 0 \quad \text{if} \quad \tilde{\rho}'_{nm} = 1 \quad \text{and} \quad \sum_{k=-1}^{1} \sum_{l=-1}^{1} \tilde{\rho}'_{n+k,m+l} \leq d_{ls}, \tag{2.108}$$

$$\tilde{\rho}''_{nm} = 1 \quad \text{if} \quad \tilde{\rho}'_{nm} = 0 \quad \text{and} \quad \sum_{k=-1}^{1} \sum_{l=-1}^{1} \tilde{\rho}'_{n+k,m+l} \geq d_{sl}. \tag{2.109}$$

In the 2D case the double sum considers the 8-neighborhood of each grid point, in the concept of pixels the four pixels with a common edge and the four pixels with just a common vertex. The filter (2.108) converts isolated liquid pixels (i.e., pore space pixels) to solid pixels if less than d_{ls} neighbors are liquid pixels. Strictly isolated liquid pixels correspond to $d_{ls} = 1$ as the considered pixel is included in the sum. For the filtered image shown in Fig. 2.17f $d_{ls} = 2$ was chosen. Conversely (2.109) converts isolated solid pixels to the liquid pixels if more than d_{sl} neighbors are liquid pixels. Strictly isolated solid corresponds to $d_{sl} = 8$. For the image in Fig. 2.17f $d_{sl} = 5$ was applied. The parameters are chosen by visual inspection of the result.

In the 3D case the corresponding triple sum considers the 26-neighborhood of each grid point, in the concept of voxels six neighbors at faces, twelve neighbors at edges and eight at vertices. Thus totally isolated solid corresponds to $d_{sl} = 26$ whereas for totally isolated liquid $d_{ls} = 1$ still holds. Applications of these filter are described in Sects. 4.6 and 4.7 on p. 132f and 135ff, respectively.

Another possibility is to reduce noise by application of a low-pass filter. The price is a blurring of fine structures. As example the cosine square filter is chosen. For a quadratic matrix with $N = M$ the components at highest frequencies in reciprocal k space are set to zero with the filter definition

$$L_{kl} = \cos^2 \frac{\pi \sqrt{(k - 1 - N/2)^2 + (l - 1 - N/2)^2}}{N\sqrt{2}}, \tag{2.110}$$

$$M^+_{kl} \to M^+_{kl} L_{kl}. \tag{2.111}$$

The effect of this filter on the numerically calculated data with noise is shown in Fig. 2.17b. As the resolution is quite high and the structures are well resolved, the blurring is not very pronounced. The binary image derived with (2.101) and the threshold giving the input porosity is shown in Fig. 2.17g. Erroneous assignments are avoided, but contacts of the actually separated discs are more frequent than with the filter pair (2.108) and (2.109), see Fig. 2.17f. The signal-magnitude distribution

[30] If the original image is corrected grid point by grid point, it gets modified during the process of correction and the rules would apply to the modified image. Thus it is necessary to apply the corrections to a copy by inspection of the original image.

with low-pass filter is narrower at the peaks compared to the distribution without filter but more intensities are present between the peaks. The fit of (2.107) in Fig. 2.17d for the low-pass filtered image is less adequate. However, the obtained porosity of $\epsilon = 0.42$ still agrees well with the input value of 0.41.

A low-pass filter can also be characterized by its point spread function (PSF). The filtered image $(\tilde{\rho}_f)_{nm}$ is the convolution of the unfiltered image $(\tilde{\rho})_{nm}$ with the PSF:

$$(\tilde{\rho}_f)_{nm} = (\tilde{\rho})_{nm} \otimes \text{PSF}. \tag{2.112}$$

According to the convolution theorem this corresponds to a multiplication in Fourier space, in the discrete case

$$\mathscr{F}\{(\tilde{\rho}_f)_{nm}\}_{kl} = M^{+}{}_{kl} L_{kl}, \tag{2.113}$$

with $\mathscr{F}\{(\tilde{\rho}_f)_{nm}\}_{kl}$ being the k, l component of the discrete Fourier transform of the filtered image. Thus the PSF is the Fourier transform of the filter:

$$\text{PSF} = \mathscr{F}\{(L)_{kl}\}. \tag{2.114}$$

The PSF of the rather broad filter in (2.110) is correspondingly narrow. An example with a Gauß filter can be seen in Fig. 4.25 on p. 136.

The choice of filter or combination of filters depends on the image characteristics, the SNR and the application. For images with outliers, a moving median filter can be appropriate. The influence of experimental artifacts and the case of varying spin density will be discussed in Sect. 2.3.4.

2.3.2 Specific Surface

Besides the porosity, the specific surface is an important information in many applications, see e.g., Sect. 4.7, p. 135ff. In the following, two methods of obtaining the surface from a volume image $(\tilde{\rho})_{nmo}$ on a rectangular grid [29] are briefly described.

2.3.2.1 Reconstruction of the Surface

Surface reconstruction is a common procedure, also used to visualize a volume image. The isosurface for a chosen isovalue is meshed, e.g., by triangulation. It is the 3D analog of a contour or isoline of a 2D data set. The isovalue can equal the threshold used to generate the binary image. In Figs. 2.18a–d results for simple structures are shown. The spin density $(\tilde{\rho})_{nmo}$ is set to one for the grid points in an inner cube of edge length l in units of the lattice spacing. Surface meshing by

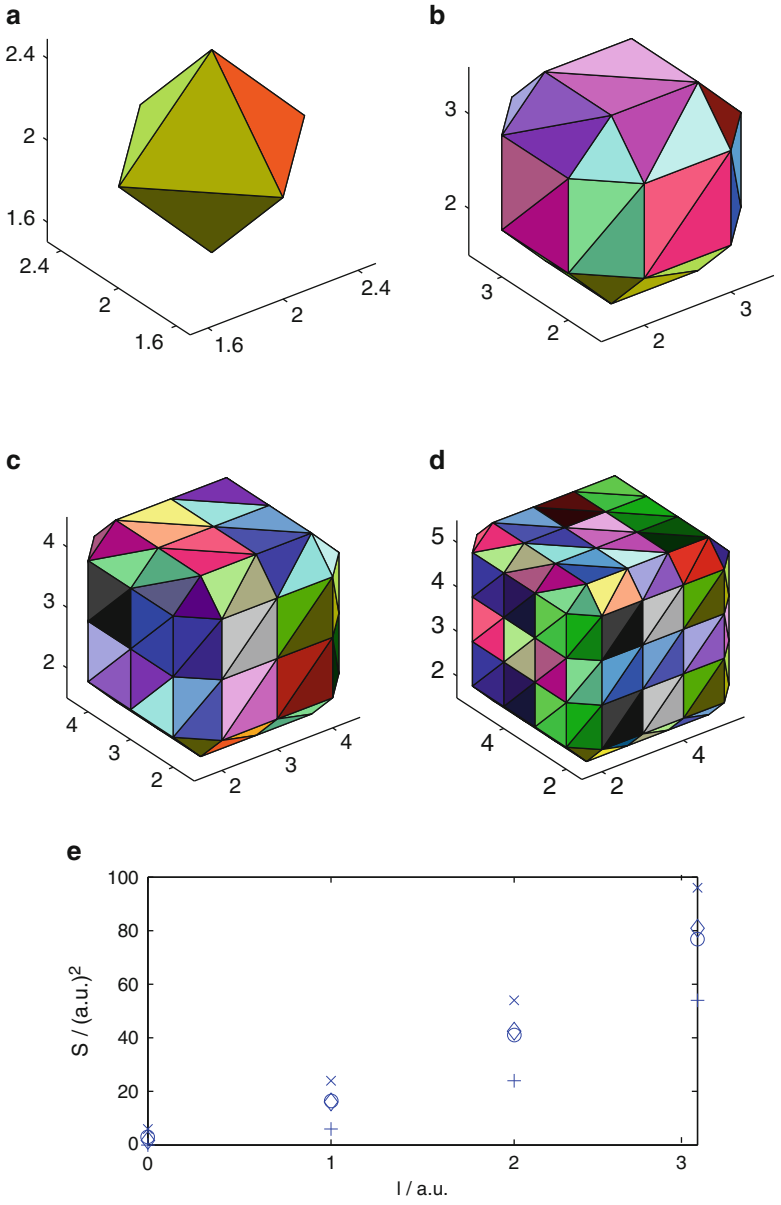

Fig. 2.18 Surface calculations for simple volume images consisting of homogeneous inner cubes with increasing edge length l in units of the lattice spacing. (**a**)–(**d**) Triangulation of the isosurface. (**a**) One inner grid point, i.e., $l = 0$. (**b**) Eight points, $l = 1$. (**c**) 27 points, $l = 2$. (**d**) 64 points, $l = 3$. (**e**) Surface $6l^2$ of the inner cube (*plus*), surface by the Crofton formula (*circle*), surface by triangulation (*diamond*), surface $6(l + 1)^2$ of the outer cube (*times*)

triangulation was performed with a commercial program MATLAB®.[31] The total area of the triangles S_D was calculated from the obtained mesh with the program listed in Sect. 6.2. The mesh is returned as a list of coordinates $\boldsymbol{r}_i$ of vertices and a list of point triples forming each face. If points $(\boldsymbol{r}_1, \boldsymbol{r}_2, \boldsymbol{r}_3)$ form a triangle with vectors $(\boldsymbol{r}_{12} = \boldsymbol{r}_2 - \boldsymbol{r}_1, \boldsymbol{r}_{13} = \boldsymbol{r}_3 - \boldsymbol{r}_1)$ along two edges, the surface S_k of this triangle amounts to

$$S_k = \frac{1}{2} |\boldsymbol{r}_{12} \times \boldsymbol{r}_{13}|. \tag{2.115}$$

With $S_\mathrm{D}(X)$ as total surface of phase X in the total volume V, the specific surface is calculated as

$$S_{V,\mathrm{D}} = S_\mathrm{D}(X)/V = \frac{1}{V} \sum_k S_k. \tag{2.116}$$

2.3.2.2 Indirect Evaluation

An efficient evaluation of the surface without reconstruction is described in [48]. Here first a binary image $(\tilde{\rho}')_{nmo}$ has to be generated from the volume image using a suitable threshold. The method of computation is based on one of the Crofton formulas for the calculation of the surface:

$$S_\mathrm{C}(X) = \frac{1}{\pi} \int \sin\theta \mathrm{d}\theta \int \mathrm{d}\varphi \iint \mathrm{d}\boldsymbol{y}\ \chi(X \cap \boldsymbol{e}_{y,\theta,\varphi}). \tag{2.117}$$

In (2.117) $\boldsymbol{e}_{y,\theta,\varphi}$ designates the line with direction (θ, φ) (polar and azimuth angle) through point $\boldsymbol{y}$ in a plane perpendicular to $\boldsymbol{e}_{y,\theta,\varphi}$. The 1D Euler number $\chi(X \cap \boldsymbol{e}_{y,\theta,\varphi})$ specifies how often the line intersects with X. The inner integral $\iint \mathrm{d}\boldsymbol{y}$ thus yields the weighted shadow area for a light source at infinite distance above the considered plane. The weight at point $\boldsymbol{y}$ is the number of object parts above this point that would cast a shadow independently. For the simple case in Fig. 2.19a the weight is 2. The inner integral is also denoted as "area of the total projection" or "rose of intersections." In this context (2.117) is also denoted as Cauchy formula. For the simple case of a sphere it is easily verified that the integration over the unit sphere and division by π yields the correct value for the sphere surface.

In the case of discrete grid points in three dimensions the evaluation of the Crofton formula (2.117) in [48] is based on the 8-neighborhood of each grid point. As indicated in Fig. 2.19b it can be encoded with eight bits or one byte. The grid point whose neighborhood is to be encoded is associated with the least significant bit 2^0, the neighboring grid points with 2^1 to 2^7. A bit is set only if it belongs to the phase X. If grid points plotted in black in Fig. 2.19b belong to X encoding yields 10101001 as binary number or $1 + 8 + 32 + 128 = 169$ as decimal number. For the evaluation of the surface only the histogram of these numbers is required,

[31] The MathWorks™, Inc.

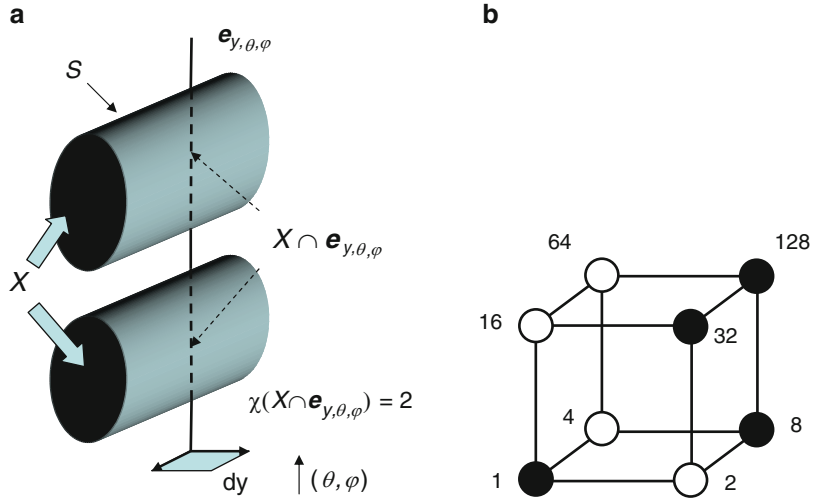

Fig. 2.19 Quantities used in the Crofton formula (**a**) and encoding of the 8-neighborhood of a grid point in the discrete case (**b**)

not the eight-bit gray-tone image itself. In [48] a program written in language "C" is presented that performs encoding using bit-shift operations and compiles the histogram very efficiently in a single triple loop.[32] A literal translation of the required C programs presented in [48] into MATLAB® language can be found in Sect. 6.1. The integration in 2.117 is replaced by a double sum over all 256 possible configurations with the gray-tone histogram as weight and over the 13 directions occurring in the 8-neighborhood (three edge directions, $3 \times 2 = 6$ face diagonals, four body diagonals). The Euler number is obtained very compactly and efficiently as sum of two products of results from logical comparisons involving "bit-wise OR" and "bitwise AND" operations, see Sect. 6.1. In the sum over directions in space weights accounting for the associated solid angle occur. Note that the figures appearing in [48] and Sect. 6.1 only hold for the common case of isotropic spatial resolution.

2.3.2.3 Comparison of the Methods

First the surfaces calculated with both methods are compared for the simple cubic geometries shown in Fig. 2.18. The smallest cube shown in Fig. 2.18a consists of a single grid point and has edge length $l = 0$. Triangulation yields an octahedron with edge length $1/\sqrt{2}$ in units of the lattice spacing. Its surface S_D, indicated in the following in units of the squared lattice distance, amounts to $\sqrt{3}$. According to (2.46) $\tilde{\rho}_{nmo}$ approximates in each direction the integral of the spin density in

[32] A free download as file ghist.c is available at http://www.materialography.net/.

the range of one lattice spacing. A sphere with the lattice spacing as diameter has surface $\pi/6$. A cube with the lattice spacing as edge length (cubical voxel) has surface 6. Computation according to [48] yields $S_C = 3$. In this simplest case the considered results increase in the order $6l^2 < \pi/6 < S_D < S_C < 6(l+1)^2$. In Fig. 2.18e the surfaces for the limiting cases "inner" and "outer" cube as well as S_D and S_C are plotted for the four cubes depicted above. For the cube consisting of eight grid points with $l = 1$ S_D and S_C yield almost the same surface. For larger cubes (verified up to 1,000 points and $l = 10$) the order changes to $S_C < S_D$. In the case of $l = 10$ the mesh consists of 1,448 triangles with total surface 686, the inner cube has surface 600, the outer 726, and the calculation based on the Crofton formula [48] yields a surface of 638. Thus the results obtained with both methods are in line with the limiting cases.

For large data sets the computing time can be relevant, especially if several volume images are to be processed. Both methods were applied to ten data sets of varying size for bead packings and one data set for a ceramic sponge [29], see Sect. 4.7. At first the implementation of both methods in MATLAB®, see Sects. 6.1 and 6.2, were tested with respect to computing time on one computer. As described in [48] the time required for S_C scales with the number of data points. It is about half of the computation time required for S_D, in which the latter obviously depends on the details of the structure under investigation. In addition the literal translation of the optimized C program in [48] into MATLAB® was compared with the original version. For 60 million data points the implementation in MATLAB® ran for 15 min on a PC with P4 processor, 3.2 GHz clock frequency, 1 GB RAM and a XP SP3 operating system. On a Linux PC with P4 processor and only 2.4 GHz clock frequency, 512 MB RAM, the program compiled with the free gcc compiler processed the same data set in only 15 s. This impressively demonstrates the efficiency of the optimized C code compared to the obviously non optimal literal translation in Sect. 6.1.

2.3.2.4 Remarks

Figure 2.18e shows that both methods yield reasonable results for simple test data. However, it is difficult to evaluate the uncertainty for images of complex structures with experimental artifacts.

Moreover the specific surface depends more or less on the observed length scale. Beads of packed bed can appear smooth on a coarse length scale and coarse on a fine length scale. On a molecular length scale the observed specific surface can increase drastically as, e.g., for zeolites. A dependence of the specific surface on the length scale in the accessible range of length scales can be studied by variation of the spatial resolution.

For structures with various relevant length scales obtaining a statistically meaningful volume image is difficult. The data set should contain enough representative coarse structures. The spatial resolution cannot be made arbitrarily small compared to the total image size, for experimental reasons or simply because of the maximum

amount of manageable data. Thus fine structures might not be sufficiently resolved. For coarse structures, edge effects at the borders of the volume image become noticeable.

As already discussed in Sect. 2.3 the choice of the isovalue or threshold also influences the specific surface. Erroneous assignments of grid points are absolutely to be avoided.

To study the inner specific surface NMR measurements of diffusion within the porous structure can be used, see e.g., [3, 44] and also Sect. 4.10.

2.3.3 Segmentation and Frequency Distributions

The porosity and specific surface is clearly defined for a porous system, apart from the length-scale problem. For an open porous system it can be interesting to segment the pore space into virtual individual pores with windows at the necks between connected pores. If this is accomplished, e.g., pore-size distributions can be constructed also for open pore structures like ceramic sponges. In favorable cases segmentation can be performed using existing methods. However, for the volume images studied the results obtained using MATLAB® and MAVI[33] were not satisfying. A method was thus worked out and implemented that allowed a successful segmentation. It is partially described in [26, 55]. However, the program used in these papers is not available from the authors. In the following the commercially available watershed transformation is briefly described. The new method is presented in more detail. Both methods for 3D segmentation are compared using again artificially generated 2D images.

2.3.3.1 Watershed Transformation

Both methods require a binary image $(\tilde{\rho}')_{nm}$. In Fig. 2.20 black areas signify discs in a loose packing. The regular structure in Fig. 2.20a has porosity $\epsilon = 0.55$, the irregular structure in Fig. 2.20b has a slightly lower porosity $\epsilon = 0.53$. Both methods start with a distance transformation, see Fig. 2.20c. Each grid point in the pore space is encoded with the closest distance to a solid grid point. In MATLAB® the Euclidean distance is used by default. A slightly different definition of the distance is obtained using a kind of "morphological thinning." It was used in [26] and was also implemented for the analysis presented in [24]. Here, the Euclidean distance provided by MATLAB® was used for both methods for the sake of comparability:

$$a_{nm} = \min_{op} \sqrt{(o-n)^2 + (p-m)^2} \quad \text{with} \quad \tilde{\rho}'_{nm} = 1 \quad \text{and} \quad \tilde{\rho}'_{op} = 0. \tag{2.118}$$

[33] MAVI – Modular Algorithms for Volume Images, Copyright © 2006 Fraunhofer Institut für Techno- und Wirtschaftsmathematik.

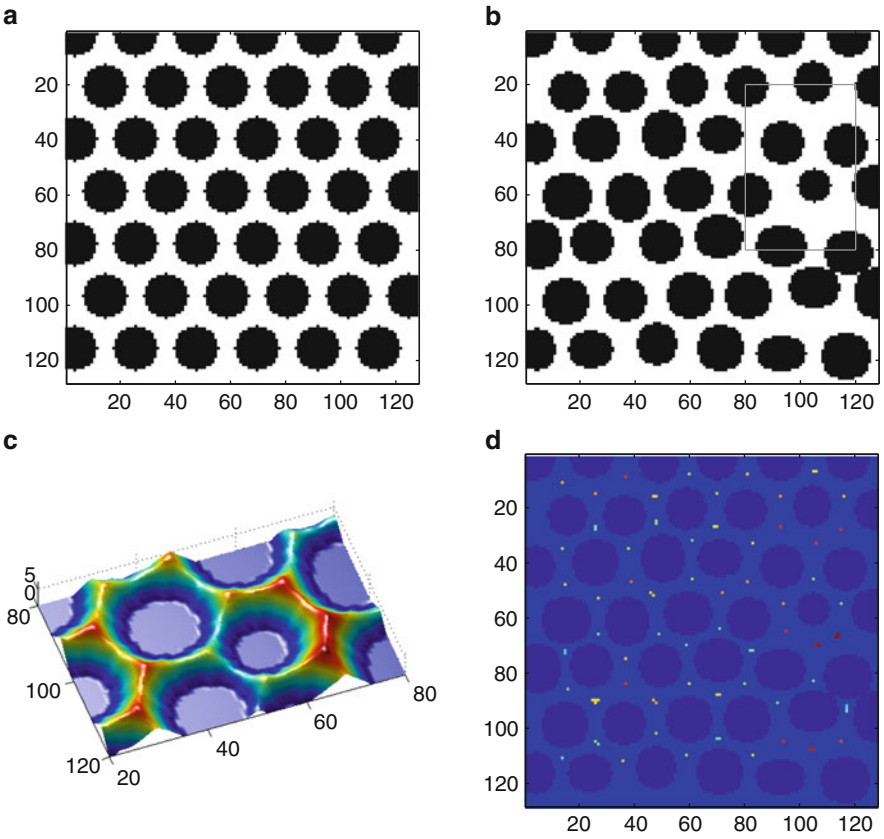

Fig. 2.20 Simple 2D geometries used to test pore-space segmentation. (**a**) Regular structure. (**b**) Irregular structure. (**c**) Distance transformation (2.118) for the cut-out indicated in (**b**). (**d**) Local maxima for the irregular structure (**b**). The average in the neighborhood of local maxima (2.121) is superimposed on the structure

For the watershed transformation, the "distance hills" $(a)_{nm}$ are inverted to the "valleys" $(-a)_{nm}$. Infinite depth is assigned to the solid phase. This matrix is segmented by the watershed transformation [68],[34] in analogy with the catchment basins in hydrology. In Fig. 2.21a the successful segmentation of the regular structure is shown. Each disc is surrounded by six regions in the pore space (catchment basins) that are identified as individual pores. The pixel line separating the basins is labeled separately by the program. In the 3D case, the separation surface is the window in the neck between two pores. At low resolution, a significant portion of grid points is assigned to the separation and not to pores, which is

[34]Concerning the algorithm, MATLAB® refers to [46], where several watershed algorithms are described.

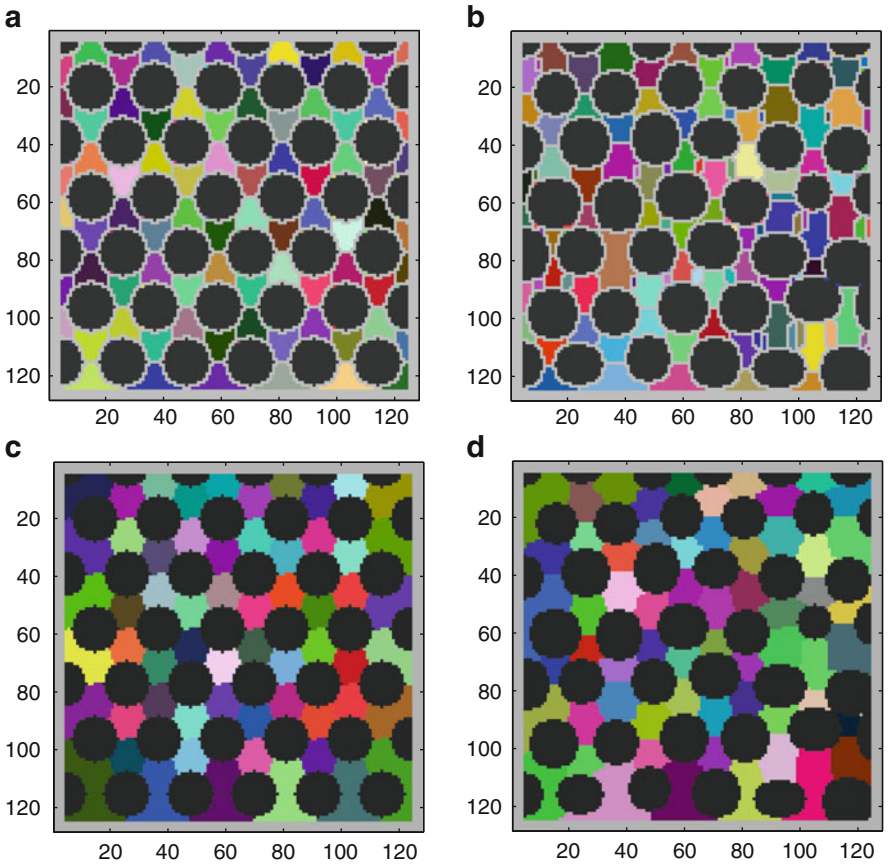

Fig. 2.21 Segmentation of the 2D structures shown in Fig. 2.20. (**a**, **b**) Results obtained with the commercial program. (**c**, **d**) Results obtained with the developed program. (**a**) Successful segmentation by watershed transformation for the regular structure. (**b**) Over-segmentation by watershed transformation for the irregular structure. (**c**) Successful segmentation by stratus transformation for the regular structure. (**d**) Successful segmentation by stratus transformation for the irregular structure

problematic. Discs are also segmented. However, the area associated with a disc can be larger than the disc itself. In Fig. 2.21a the grid points of the discs are plotted in black. Colored spots on the disc borders indicate this artifact. In addition, grid points at the border of discs are again not counted as part of an individual pore.

For the irregular structure in Fig. 2.21b the standard watershed transformation leads to an over segmentation, i.e., some discs are surrounded by many small areas identified as individual pores. Modified versions allow to solve this problem by user intervention, e.g., setting of starting points or collection of areas. However, user intervention introduces a subjective component and is impracticable for large 3D data sets. The problem can also be tackled by preflooding.

2.3.3.2 "Stratus" Transformation

For the procedure partially described in [26, 55][35] the distance matrix $(a)_{nm}$ is not inverted. In the 2D case this matrix can be represented as hilly landscape. The procedure is analog for the 3D case, although more difficult to visualize. Segmentation of the pore space amounts to the assignment of grid points to individual hilltops. The gradual process can be compared to the spectacle that can be seen from a hilltop in the situation of meteorological inversion. The observer can enjoy the sunshine, while everything only some meters below is covered by above-ground fog, an even stratus cloud.[36] Hilltops are the pore centers. As the stratus gradually descends, more and more grid points become visible and are associated with the adjacent hill. Eventually grid points on a saddle border on two hills. The saddle is the virtual boundary between the pores. The stratus is gradually lowered until all grid points are assigned to hills representing pores.

For the search of hilltops or local maxima, first the pairs of indices (n, m) fulfilling

$$a_{nm} = \max_{(o,p) \in O \times P} a_{op} \tag{2.119}$$

are determined. Here $O \times P$ is a moving product set of natural numbers around (n, m). It covers a quadratic (3D: cubic) range with edge length $2l$ and $2l + 1$ points along the edges:

$$\begin{aligned} O &= \{a \,|\, a \in \boldsymbol{N} \text{ and } n - l \leq a \leq n + l\} \\ P &= \{a \,|\, a \in \boldsymbol{N} \text{ and } m - l \leq a \leq m + l\}. \end{aligned} \tag{2.120}$$

Hereby a first list of length K with index pairs of local maxima $\boldsymbol{r}_k = (n_k, m_k)$ is obtained. Additionally a list of the associated averages

$$\bar{a}_k = \frac{1}{(2l+1)^2} \sum_{o=n_k-l}^{n_k+l} \sum_{p=m_k-l}^{m_k+l} a_{op} \tag{2.121}$$

is established. Grid points in the border area of the image matrix are to be treated separately. Alternatively points at the border can be excluded as potential pore centers, as it was done in the presented analysis. The value of l should be

[35] Generation of the distance matrix by a kind of "morphological thinning" is explained in detail, the following steps are only mentioned. However, a straight-forward search for local maxima in the next step leads to an over segmentation. Also in the subsequent association of adjacent grid points to the maxima, care must be taken to avoid distorted pores. Therefore details of the developed procedure are described and in Sect. 6.3 the implementation in MATLAB® is listed.

[36] In Zrich, a tablet on the tramway bearing the inscription "Uetliberg hell" (Uetliberg bright) indicates this situation.

smaller than the smallest considered distance between two pore centers. For the segmentation shown in Fig. 2.21c, d, $l = 4$ was chosen.

As the indices are natural numbers only discrete values are obtained as distances by (2.118). Thus it can occur for an irregular structure as shown in Fig. 2.20b that a ridge or small plateau is obtained instead of a crest, see Fig. 2.20d. Each point of the line contributes to the list $\boldsymbol{r}_k$. In the following association of grid points this would lead to an over-segmentation. Therefore a second parameter c is introduced as minimum distance between two pore centers. In the decision which point $\boldsymbol{r}_k$ is to be retained form a set of local maxima with distances smaller than c the averages $\bar{a}_k$ are compared. For a grid point at the end of a ridge the average is smaller than for a point in the middle of the ridge. Thus, starting with the first local maximum in the list, each local maximum is tested against the following ones with respect to their distance. If the inequality

$$|\boldsymbol{r}_k - \boldsymbol{r}_{k+l}| < c \quad \text{with} \quad l \in \{a \,|\, a \in \boldsymbol{N} \text{ and } k + l \leq K\} \tag{2.122}$$

is false for a $\boldsymbol{r}_k$ and all l this local maximum is incorporated in the final list of local maxima $(\boldsymbol{r})_j$. As soon as the inequality (2.122) is fulfilled for one l the comparison is stopped for this k. If the following local maximum has a higher average, i.e., if

$$\bar{a}_k < \bar{a}_{k+l} \tag{2.123}$$

is fulfilled, $\boldsymbol{r}_k$ is discarded. If this is not the case, $\bar{a}_{k+l}$ and $\boldsymbol{r}_{k+l}$ are replaced by $\bar{a}_k$ and $\boldsymbol{r}_k$, respectively. Thus the decision if the local maximum is to incorporated in the final list is postponed to following tests. In the example of the regular structure shown in Fig. 2.21c the final list has the same length J as the original list, namely $K = 60$. For the irregular structure of Fig. 2.21d however $K = 81$ and $J = 60$. The minimum distance was chosen as $c = 6$.

In the gradual association of grid points in the pore space to bordering points already assigned to pore centers two points have to be considered. For large data sets the implementation has to be numerically efficient and all grid points in the pore space have to be covered. Furthermore it has to be avoided that pores get distorted by an unsuitable systematic procedure (e.g., growth of pores into neighboring pores). First "gradually" has to be defined. Distances calculated by (2.118) extend from one to several lattice spacings. For the structure shown in Fig. 2.21d, e.g., the maximum distance amounts to $\sqrt{7^2 + 1}$ and for the structure in Fig. 2.21c 5 is obtained (with two possibilities: $\sqrt{5^2}$ and $\sqrt{3^2 + 4^2}$). In the first step the lattice points with a distance between the rounded off maximum distance h_1 and the maximum distance are considered. These grid points fulfill the inequality

$$a_{nm} > h_1 \text{ with } h_1 = a_{\max} - (a_{\max} \bmod 1) \text{ and } a_{\max} = \max_j a(\boldsymbol{r}_j). \tag{2.124}$$

Grid points already assigned have to be excluded. These are collected in the matrix $(z)_{nm}$ of the segmented image and are set to the value j of the corresponding pore

center. Initially the segmented image is only non-zero at the local maxima:

$$z_{nm} = \begin{cases} j & : \quad (n,m) = \boldsymbol{r}_j \\ 0 & : \quad \text{else} \end{cases} . \tag{2.125}$$

When all grid points above the highest level are assigned new points are considered applying (2.124) with a lower level h_i reduced, e.g., by one.[37] Both conditions for the points to be considered can be combined in a compact matrix notation and are thus efficiently evaluated in MATLAB® :

$$(\Theta)_{nm} = ((a)_{nm} > h_i) \ \wedge \ (\neg(z)_{nm}). \tag{2.126}$$

The negation is implemented such that $\neg z_{nm} = 0$ for $z_{nm} \neq 0$. The matrix notation in (2.126) signifies for the components

$$\Theta_{nm} = \begin{cases} 1 & : \quad a_{nm} > h_i \text{ and } z_{nm} = 0 \\ 0 & : \quad \text{else} \end{cases} . \tag{2.127}$$

Thus (2.126) is a binary matrix with ones at the positions of grid points to be considered and zeros elsewhere. The neighborhood of points under consideration to points already assigned is established by comparison of $(\Theta)_{nm}$ with a cyclical shifted version of matrix $(z)_{nm}$. In the 2D case a shift by one is executed either to the left, to the right, to the bottom, or to the top. For the indices the shift is either the addition or subtraction of one in either the first or the second index:

$$(n,m) \to (n,m) + \xi \quad \text{with} \quad \xi \in \{(-1,0),(1,0),(0,-1),(0,1)\}. \tag{2.128}$$

As $(\Theta)_{nm}$ is a binary matrix the shift amounts to a bit-shift operation. For $n > 0$ a shift by n bits to the left or to the top is denoted by $<< n$. A shift to the right or bottom is denoted by $>> n$. For $n < 0$ directions are inverted. Thus the matrix-oriented logical operation

$$(\Lambda)_{nm} = (\Theta)_{nm} \ \wedge \ ((z)_{nm} << \xi) \tag{2.129}$$

yields the binary matrix $(\Lambda)_{nm}$ with ones at the positions of points under consideration that are adjacent with already assigned points in direction ξ and zeros elsewhere. At the positions where $(\Lambda)_{nm}$ contains ones the matrix $(z)_{nm}$ should be assigned with the value of the neighboring assigned point. This can be done again very efficiently by indexing of the matrix $(z)_{nm}$ with the binary matrix $(\Lambda)_{nm}$ and

[37] The distance matrix generated in [26, 55] contains only natural numbers so that a reduction of the levels by less than one is not meaningful in this case.

with the version cyclical shifted in the opposite direction, respectively[38]:

$$(z)_\Lambda = (z)_{\Lambda >> \xi}. \tag{2.130}$$

Indexing with the (shifted) matrix signifies for the components

$$z_{nm} = \begin{cases} z_{op} & : \quad \Lambda_{nm} = 1 \text{ with } (o,p) = (n,m) - \xi \\ z_{nm} & : \quad \text{else} \end{cases}. \tag{2.131}$$

Thus the gradual assignment can be described as follows:

1. Determine the grid points to be assigned at a given level and state of assignment using (2.126).
2. Generate a random permutation of the shift-vectors ξ in the set given in (2.128).
3. Determine consecutively for the four (3D: six) permuted shifts the neighboring pixel (3D: voxels) according to (2.129) and assign those grid points according to (2.130).
4. Repeat steps 1 to 3 until all grid points above the actual level are assigned.
5. Lower the level and repeat steps 1 to 4 until level zero is reached and all grid points are assigned to individual pores.

The implementation in a computer program is listed in Sect. 6.3. Without random permutations the oblique borders between pores seen in Fig. 2.21c, d are not obtained. If the random element is not desired a list of suitable permutations can be fixed, leading to an exactly reproducible segmentation. Without the gradual lowering of levels small pores grow into large pores.

2.3.3.3 Comparison of Methods and Example of Analysis

Figure 2.21c, d shows that the implemented stratus transformation produces meaningful results not only for the regular but also for the irregular structure. All grid points in the pore space are associated to separate pores. Only one point at $(x, y) \approx (120, 90)$ remains. However, it is surrounded by discs and is not part of the open pore space. At variance with the commercial method areas at the border of the data set are not assigned to new pores as on the left, bottom, and right border of Fig. 2.21a. Indeed the distance matrix has local maxima at the borders, but borders were not included in the search for local maxima using (2.119). If pore centers at the border are to be allowed, these regions have to be treated separately.

Examples of geometrical characteristics whose distribution can be analyzed are the pore volume, pore surface, coordination number (i.e., number of pores directly

[38]Equivalent and more intuitive is the assignment of new values with the equation $(z)_\Lambda = (z << \xi)_\Lambda$. Due to the syntax of MATLAB® this version requires an additional step as the cyclical shifted matrix cannot be indexed with a matrix in the same expression.

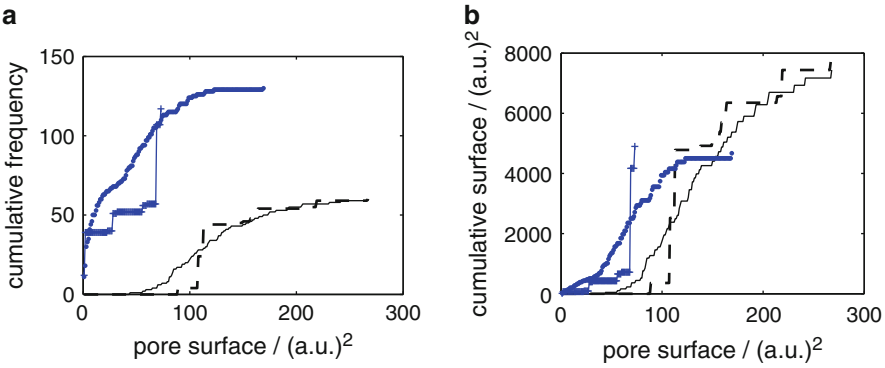

Fig. 2.22 Cumulative pore-surface distribution for both structures and methods shown in Fig. 2.21. The distributions are not normalized in order to emphasize the differences for the two methods. (**a**) Cumulative distribution by number or frequency Q_0. (**b**) Cumulative distribution by surface Q_2. *Crosses* correspond to Fig. 2.21a, *points* to Fig. 2.21b, the *broken line* to Fig. 2.21c, and the *solid line* to Fig. 2.21d

connected to one pore) or the cross-section area of the windows between pores. The total number of pores J is obtained immediately. Whereas the stratus transformation yields 60 pores for both examples, watershed transformation results in 121 pores for the regular structure in Fig. 2.21a and 147 for irregular structure in Fig. 2.21b. For the regular structure the difference is mainly due to pores assigned to the discs that are larger than the discs. The rest is due to 19 additional pores at the left, bottom, and right border. For the irregular structure the number is increased by over-segmentation.

As example the cumulative pore-surface distribution for both structures and methods is shown in Fig. 2.22, see figure caption. Cumulative distribution signifies that at an abscissa value for the considered kind of quantity the total amount of parts with quantity less or equal to that value are given as ordinate value. In Fig. 2.22a the number of parts was chosen as amount, the corresponding cumulative distribution is denoted as Q_0. In Fig. 2.22b the surface of the parts was chosen as amount, corresponding to Q_2. The parts are the virtually separated pores. In the 3D case Q_2 can also be used. More common is the volume or mass as amount with the corresponding symbol Q_3. The kind of quantity is the pore size, here as pore surface in units of the pixel numbers. In order to emphasize the differences between both methods the distributions are not normalized as usual to the total amount. A discrete derivative to a distribution density is noisy due to the small number of pores.

The total number of pores is given in Fig. 2.22a at the end points of the curves. Due to the reasons discussed above it is significantly higher for the watershed transformation. Some over-segmented pores for the irregular structure do not contribute as part of the border was excluded from the analysis for both structures and methods. Endpoints in Fig. 2.22b indicate the total pore surface. As discussed above it is markedly smaller for the watershed transformation as grid points of

the watershed line are counted separately and not as part of the pore space. Both methods reproduce the slightly higher porosity of the regular structure.

Due to the difficulties of the watershed transformation the resulting distributions are not very significant. At least the 60 correctly assigned pores of the regular structure have a narrow surface distribution. With the surface as amount, small over-segmented areas or isolated grid points around the discs contribute less than in the frequency distribution.

The surface distribution for the regular structure is somewhat less narrow using the stratus transformation. At higher surfaces this is due to the larger pores at the left, bottom, and right border. For the irregular structure the median of the distribution by frequency Q_0 amounts to 115 grid points, for the distribution by surface Q_2 to 133. For the regular structure the median of the distribution by frequency and by surface amounts to 111 grid points.

A different application of the stratus transformation to the segmentation of a poorly resolved 3D structure can be found in [24] and Sect. 4.6, p. 132.

2.3.4 Signal, Noise, and Variance

In the preceding it has been assumed that the sample solely consists of areas with constant observable spin density and areas that give no signal. In this section the general case of a continuously distributed observable spin density is considered. In some applications the variance of the spin density is of interest, such as in the characterization of the uniformity of mixtures, see Sect. 4.3, p. 111ff and [32]. Therefore the influence of artifacts on the signal amplitude and variance in the measured NMR image is analyzed.

According to (2.38) the nondimensionalized total transverse magnetization M^+ in ideal Fourier imaging is the Fourier transform of the spin density ρ. In Sect. 2.3.1 it was shown in an example how already artifacts due to the inverse transform (2.40) lead to a distortion of the amplitude in the result $(\tilde{\rho})_{nmo}$. In the following this artifact is neglected compared to artifacts resulting from the inhomogeneity of the rf field $\boldsymbol{B_1}$ and noise. First the generation of the signal and the consequence of rf inhomogeneity is treated in some detail. Then the origin of noise and its impact on the magnitude image is discussed on p. 70f. The influence of inhomogeneities and noise on the observed signal variance is finally treated on p. 71f.

2.3.4.1 Signal Amplitude

To begin with the spatial variation of $\boldsymbol{B_1}$ leads to a spatial dependence of the angular velocity of the Rabi nutation (2.24). For $\omega_1\tau = -\gamma B_1(\boldsymbol{r})\tau \neq \pi/2$ the local transverse magnetization is scaled with $\sin(\omega_1\tau) < 1$. Frequently a second π rf pulse is used for refocusing, see e.g., Fig. 2.8. Due to the deviance $2\omega_1\tau \neq \pi$ in average a total scaling with $\sin^3(\omega_1\tau)$ is obtained [27]. For $\omega_1\tau \approx \pi/2$ this

second-order attenuation of the signal is neglected against the linear dependence of the signal on $\boldsymbol{B_1}$ discussed in the following.

In [37] the voltage U induced in the reception coil is derived using the reciprocity theorem [39]. It relates this voltage to the field $\boldsymbol{B}_1^{\mathrm{dc}}$ generated by the coil when driven with the direct current I^{dc}:

$$U = -\iiint_V \frac{\mathrm{d}}{\mathrm{d}t}\frac{1}{I^{\mathrm{dc}}}\boldsymbol{B}_1^{\mathrm{dc}}(\boldsymbol{r})\boldsymbol{M}(\boldsymbol{r},t)\,\mathrm{d}x\mathrm{d}y\mathrm{d}z. \tag{2.132}$$

The relation of this voltage to the measured spin-density image is derived with consideration of an inhomogeneous $\boldsymbol{B}_1^{\mathrm{dc}}(\boldsymbol{r})$ field. To this the transverse magnetization expressed in (2.32) and (2.37) in the rotating frame of reference has to be expressed in the laboratory frame:

$$\boldsymbol{M}(\boldsymbol{r},t) = \rho(\boldsymbol{r})\langle\mu_z\rangle\left[\cos(\omega_0 t - \boldsymbol{k}\boldsymbol{r})\,\boldsymbol{e_x} + \sin(\omega_0 t - \boldsymbol{k}\boldsymbol{r})\,\boldsymbol{e_y}\right]. \tag{2.133}$$

Insertion into (2.132) and execution of the time derivative yields

$$\begin{aligned} U = -\frac{\langle\mu_z\rangle}{I^{\mathrm{dc}}}\iiint_V \rho(\boldsymbol{r}) \\ [-\sin(\omega_0 t - \boldsymbol{k}\boldsymbol{r})\,B_{1,x}^{\mathrm{dc}}(\boldsymbol{r}) + \cos(\omega_0 t - \boldsymbol{k}\boldsymbol{r})\,B_{1,y}^{\mathrm{dc}}(\boldsymbol{r})] \\ (\omega_0 - \gamma\boldsymbol{G}\boldsymbol{r})\,\mathrm{d}x\mathrm{d}y\mathrm{d}z. \end{aligned} \tag{2.134}$$

In the time derivative of the phase $\boldsymbol{k}\boldsymbol{r}$ due to gradients definition (2.36) was used. However, the contribution $|\gamma\boldsymbol{G}\boldsymbol{r}| \ll |\omega_0|$ on the signal amplitude is neglected. It is assumed that $B_{1,x}^{\mathrm{dc}}(\boldsymbol{r}) = 0$, i.e., $\phi_1 = -\pi/2$ in (2.22). Denoting the remaining transverse component as $B_{1,y}^{\mathrm{dc}}(\boldsymbol{r}) = -B_1^{\mathrm{dc}}(\boldsymbol{r})$ the induced voltage is expressed as

$$U = \frac{\langle\mu_z\rangle}{I^{\mathrm{dc}}}\omega_0\iiint_V \rho(\boldsymbol{r})\cos(\omega_0 t - \boldsymbol{k}\boldsymbol{r})\,B_1^{\mathrm{dc}}(\boldsymbol{r})\,\mathrm{d}x\mathrm{d}y\mathrm{d}z. \tag{2.135}$$

Before digitization the induced high-frequency voltage in the megahertz range is mixed with the resonance frequency, assumed to be equal to the rf frequency. This corresponds to the transformation in the rotating frame, see (2.18). As for the excitation here the common case is considered that a linear polarized field is detected. To obtain the circular polarized average magnetization the voltage is mixed in quadrature detection with two reference signals phase-shifted by $\pi/2$. Multiplication of the time-dependent term with $\cos(\omega_0 t)$ respectively $\sin(-\omega_0 t)$ yields

$$\begin{aligned} \cos(\omega_0 t - \boldsymbol{k}\boldsymbol{r})\cos(\omega_0 t) &= \frac{1}{2}[\cos(2\omega_0 t - \boldsymbol{k}\boldsymbol{r}) + \cos(-\boldsymbol{k}\boldsymbol{r})] \\ \cos(\omega_0 t - \boldsymbol{k}\boldsymbol{r})\sin(-\omega_0 t) &= \frac{1}{2}[-\sin(2\omega_0 t - \boldsymbol{k}\boldsymbol{r}) + \sin(-\boldsymbol{k}\boldsymbol{r})]. \end{aligned} \tag{2.136}$$

The high-frequency component at about twice the resonance frequency is eliminated by a low-pass filter. The field averaged over the sample is denoted as $\langle B_1^{\mathrm{dc}} \rangle$ and relative errors compared to a homogeneous field as $e(\boldsymbol{r})$. The result of mixing and filtering then reads

$$U \cos(\omega_0 t) \rightarrow \frac{\langle \mu_z \rangle \langle B_1^{\mathrm{dc}} \rangle}{2 I^{\mathrm{dc}}} \omega_0 \iiint_V \rho(\boldsymbol{r}) e(\boldsymbol{r}) \cos(-\boldsymbol{k}\boldsymbol{r}) \, \mathrm{d}x \mathrm{d}y \mathrm{d}z$$

$$U \sin(-\omega_0 t) \rightarrow \frac{\langle \mu_z \rangle \langle B_1^{\mathrm{dc}} \rangle}{2 I^{\mathrm{dc}}} \omega_0 \iiint_V \rho(\boldsymbol{r}) e(\boldsymbol{r}) \sin(-\boldsymbol{k}\boldsymbol{r}) \, \mathrm{d}x \mathrm{d}y \mathrm{d}z. \quad (2.137)$$

In analogy to (2.38) the second contribution is multiplied by i and added to the first contribution. Nondimensionalization with $\langle \mu_z \rangle \langle B_1^{\mathrm{dc}} \rangle \omega_0 / (2 I^{\mathrm{dc}})$ yields as final result

$$U^+(\boldsymbol{k}) = \iiint_V \rho(\boldsymbol{r}) e(\boldsymbol{r}) \exp(-i \boldsymbol{k}\boldsymbol{r}) \, \mathrm{d}x \mathrm{d}y \mathrm{d}z. \quad (2.138)$$

Thus the nondimensionalized complex voltage is the Fourier transform of the spin density weighted with relative errors of the rf-field amplitude. Whereas this weighting can already be recognized in (2.132) the factor used above for nondimensionalization shows the dependencies of the signal amplitude:

$$U \propto \langle \mu_z \rangle \frac{\langle B_1^{\mathrm{dc}} \rangle}{I^{\mathrm{dc}}} \omega_0 = \frac{\gamma I (I+1) \hbar^2}{3 k T} \frac{\langle B_1^{\mathrm{dc}} \rangle}{I^{\mathrm{dc}}} \omega_0^2, \quad (2.139)$$

In the expression of the Boltzmann averaged z component of the observed nuclear magnetic dipoles, see (2.30), γB_0 was replaced by the resonance frequency ω_0. The signal is thus proportional to the square of the resonance frequency. This motivates the efforts to generate the highest possible homogeneous field, as in many NMR applications the SNR is critical. The signal is further proportional to the B_1 field per current in the sample volume. Optimization of this factor along with other characteristics of the rf probe is the object of continuous research. The factors I and γ are properties of the kind of nucleus under investigation. Although the signal increases with the spin quantum number, nuclei with $I > 1/2$ are used less frequently. They possess an electric quadrupole moment. In the presence of fluctuating gradients of the electric field this leads to a very rapid signal decay. Isotopes with high magnetogyric ratio γ, spin 1/2, and large natural abundance are ^{1}H and ^{19}F. Hydrogen nuclei are studied most frequently. The sample temperature T is usually predetermined by the application. However, when measuring at different temperatures, the inverse proportionality of the signal amplitude on the temperature has to be included in a quantitative analysis.

2.3.4.2 Noise

Perturbation of the signal by noise was already introduced as additive contribution in (2.103). It has to be minimized in order to increase SNR. The noise voltage U_n is expressed in [37] as

$$U_n = (F 4kT_c \, \Delta f \, R_c)^{1/2}. \tag{2.140}$$

Whereas T in (2.139) denotes the sample temperature T_c signifies the temperature of the conductors in the rf coil. In order to reduce noise, cryogenic rf probes are established in sophisticated NMR systems. This is also beneficial for the coil resistance R_c. The noise figure of the preamplifier and the spectral width are denoted by F and Δf, respectively. Due to the skin effect the coil resistance is frequency dependent. For a wire of length l_c and radius $r_c \ll l_c$ it is given by

$$R_c = \frac{l_c}{2\pi r_c} \sqrt{\frac{\mu_r \mu_0 \omega_0}{2\sigma_c(T_c)}}, \tag{2.141}$$

s. also (3.4). The temperature-dependent electrical conductivity is denoted as σ_c and the relative permeability as μ_r. From (2.139) to (2.141) it follows that SNR scales with $\omega_0^{7/4}$. In [20] a noise contribution due to losses in the sample which is quadratic in the frequency is considered. In this case SNR is only proportional to ω_0 respectively B_0. The effectively attainable SNR depends on many factors, see e.g., [1, 13, 20, 22, 37].

As a result of the measurement the discrete inverse Fourier transform of (2.138) including B_1 inhomogeneities with additional in-phase and quadrature-phase noise is considered. In the common case of magnitude images it is expressed as

$$\begin{aligned} \hat{\rho}_{nmo} &= \sqrt{[\mathrm{Re}(\tilde{\rho}_{nmo})\, \hat{e}_{nmo} + n_{i,nmo}]^2 + [\mathrm{Im}(\tilde{\rho}_{nmo})\, \hat{e}_{nmo} + n_{q,nmo}]^2} \\ &\approx \tilde{\rho}_{nmo}\, \hat{e}_{nmo} + n_{i,nmo}. \end{aligned} \tag{2.142}$$

For the discrete inverse Fourier transform of the ideal measurement the notation $(\tilde{\rho})_{nmo}$ was already used to indicate the presence of transformation artifacts. In analogy the outcome of an ideal measurement of $e(\boldsymbol{r})$, i.e., with constant ρ in (2.138) would be denoted as $(\tilde{e})_{nmo}$. However, the multiplicative relation between ρ and e in (2.138) does not strictly transform into a multiplicative relation between $(\tilde{\rho})_{nmo}$ and $(\tilde{e})_{nmo}$, as can be seen by inspection of (2.46). In fact transformation artifacts depend on the details of the new product function. Nevertheless the notation $(\tilde{\rho})_{nmo}$ is used in (2.142). Deviations from the multiplicative relation, which are small for a smoothly varying e are accounted for by introduction of the new symbol $\hat{e}$. The simplification in (2.142) assumes that the imaginary part of the measurement can be neglected against the real part (without phase errors, see Sect. 2.3.5) and that the real part including in-phase noise is always positive. This is the case of high SNR.

2.3.4.3 Variance

The variance of the measured spin density is calculated as

$$\hat{s}^2 = \frac{1}{NMO-1} \sum_{n=1}^{N} \sum_{m=1}^{M} \sum_{o=1}^{O} (\hat{\rho}_{nmo} - \langle \hat{\rho} \rangle)^2. \tag{2.143}$$

Accepting the simplified expression in (2.142) the relation to the variance $\tilde{s}^2$ of the ideally measured spin density $(\tilde{\rho})_{nmo}$ and the variances of the inhomogeneity $(\hat{e})_{nmo}$ and noise $(n_i)_{nmo}$ can be approximated as [32, 42]:

$$\hat{s}^2 \approx \tilde{s}^2 + \langle \tilde{\rho} \rangle^2 s_e^2 + \frac{1}{N_A} s_n^2. \tag{2.144}$$

The variance of the ideally measured spin density has a factor of $\langle \hat{e} \rangle^2$ which is neglected as by definition $\langle e \rangle = 1$. The variance of the inhomogeneity is denoted by s_e^2. Its contribution scales with the square of the average spin density. In the last term s_n^2 signifies the noise variance for one scan or average, $N_A = 1$. In (2.144) it is assumed that there is no covariance between the ideally measured spin density, the inhomogeneity of the rf field and noise. The relation is formulated for the case that the accumulated nondimensionalized voltage is divided by the number of averages. Otherwise the variance of the ideally measured signal would increase with N_A^2. Therefore the scaled noise variance decreases with the inverse of N_A as factor.

If the contributions of artifacts can be determined, (2.144) can be used to correct the variance calculated from the experimental data by subtraction of these contributions. To this end measurements on a sample of same size and similar, but homogeneous spin density can be performed. For the usual case of ^{1}H such a sample can be realized by a mixture of normal and heavy water (D_2O). For a homogeneous sample the variance of the ideally measured spin density is assumed to be zero. The two remaining contributions can be separated by measuring with variable number of scans and fitting of (2.144) to the results, see Fig. 2.23.

2.3.5 Phase Correction

Deviations of the measured spin density $(\tilde{\rho})_{nmo}$ from the true spin density $\rho(\boldsymbol{r})$ due to transformation and discretization artifacts have been treated in Sect. 2.1.3, p. 14ff. The impact of noise on the signal and magnitude image as well as the application of filters were discussed on p. 50ff in Sect. 2.3.1. Systematic errors originating from inhomogeneities of the $\boldsymbol{B_1}$ field were considered in Sect. 2.3.4. In the following the influence of nonlinear phase errors on the measured spin density and their correction will be presented.

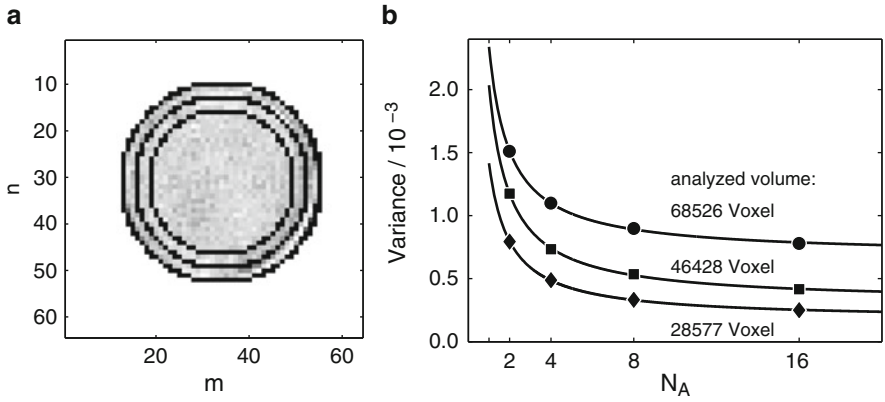

Fig. 2.23 Experimental determination of contributions to the variance by artifacts. (**a**) Slice of a 3D image of a homogeneous sample (i.e., $\tilde{s}^2 = 0$) with analyzed areas of different size. (**b**) Variance of the measured spin density (in the units used $\langle\tilde{\rho}\rangle = 0.41$) for the different areas as a function of the number of averages. *Solid lines* show fits of (2.144) to the data, allowing to separate the contributions. For white noise s_n^2 shows no systematic dependence on the area analyzed. For decreasing size, 0.0017, 0.0017, and 0.0012 are obtained, respectively. As expected, the contribution by inhomogeneities s_e^2 decreases with size: 0.0041, 0.0018, and 0.0010. Reprinted from [32] © 2007, with permission from Elsevier

2.3.5.1 Influence of Phase Errors

The influence of phase errors increases with decreasing SNR. Therefore noise is considered in the complex image. For the sake of simplicity, inhomogeneities of the $\boldsymbol{B_1}$ field are neglected. In addition it is assumed that the imaginary part of the transformed spin density can be neglected, $\tilde{\rho}_{nmo} = \mathrm{Re}(\tilde{\rho}_{nmo})$. Experimentally, a phase error $(\phi_e)_{nmo}$ is observed, so that the measured spin density is expressed as

$$\hat{\rho}_{nmo} = (\tilde{\rho}_{nmo} + n_{i,nmo} + i\, n_{q,nmo})\, \exp(i\, \phi_{e,nmo}). \tag{2.145}$$

Phase errors originate e.g. from off-resonance effects, pulse-phase errors, relaxation, transformation artifacts, or effects of electronic signal processing. If the experimental image is expressed as a magnitude image and a phase image, the relation to the unknown quantities in (2.145) is

$$|\hat{\rho}_{nmo}| = \sqrt{(\tilde{\rho}_{nmo} + n_{i,nmo})^2 + n_{q,nmo}^2} \tag{2.146}$$

$$\phi_{nmo} = \phi_{n,nmo} + \phi_{e,nmo}. \tag{2.147}$$

The noise contribution to the image phase is the four-quadrant inverse tangent

$$\phi_{n,nmo} = \tan^{-1}(n_{q,nmo}/(\tilde{\rho}_{nmo} + n_{i,nmo})). \tag{2.148}$$

For uncorrelated noise the average of $\phi_{n,nmo}$ is zero. The standard deviation of the phase resulting from noise is approximately $s_n/\tilde{\rho}_{nmo}$, the inverse of SNR [42]. According to (2.146) noise in the imaginary part also contributes to the magnitude image. In addition, normal distribution of noise leads to a Rice respectively Rayleigh distribution in the magnitude image, see (2.105) and (2.106). This does not only decrease SNR but also leads to a systematic, signal-dependent bias of signal amplitude.

2.3.5.2 Intention and Method of Phase Correction

The intention of phase correction is to determine the phase error $(\phi_e)_{nmo}$, to correct the complex image for the phase error and to use the real part of the result [2, 5, 11, 17, 45, 47, 53, 64]:

$$\mathrm{Re}\{\hat{\rho}_{nmo}\,\exp(-i\,\phi_{e,nmo})\} = \tilde{\rho}_{nmo} + n_{i,nmo} \tag{2.149}$$

$$= |\hat{\rho}_{nmo}|\cos(\phi_{n,nmo}). \tag{2.150}$$

The experimental phase consists of the more or less smooth phase error with additional noise. It can be attempted to fit a parametrized function $(\phi_o)_{nmo}$ to the experimental phase $(\phi)_{nmo}$. This requires that the phase image can be first corrected for 2π jumps, as the experimental phase is contained in an interval of width 2π. However, this procedure called phase unwrapping fails if the image consists of several unconnected regions with low SNR. Another method circumvents the ambiguity of the phase. The procedure is to minimize the magnitude or square of the imaginary part, e.g.,

$$\min_{\boldsymbol{k}_o} \sum_{nmo} |\hat{\rho}_{nmo}|^2 \sin(\phi_{nmo} - \phi_{o,nmo})^2 \tag{2.151}$$

with the parameter vector $\boldsymbol{k}_o$ of the phase fit function. The index o signifies order if the fit function represents a series expansion. Differences between the fitted and experimental phase of multiples of 2π have no influence on the sine function producing the imaginary part. For unconnected regions in the image it was observed that this method can lead to areas with positive as well as areas with negative signal (with superimposed in-phase noise). In the areas with negative signal a phase error of π remains. In order to solve also this problem, a new method was developed [33]. It consists of the maximization of the real-part sum:

$$\max_{\boldsymbol{k}_o} \sum_{nmo} |\hat{\rho}_{nmo}|\cos(\phi_{nmo} - \phi_{o,nmo}). \tag{2.152}$$

Taylor expansion of the cosine to second order shows that in this approximation and without 2π jumps the procedure corresponds to a least-square fit of the phase

function with the signal magnitude as weight. Fitting without weight yields similar results. Using the squared signal magnitude as weight leads to a chi-square fit, as the standard deviation of the phase is inversely proportional to the signal intensity. A fundamentally different method uses the phase of a filtered image as approximation for phase correction, see [47] and Fig. 4.4.

2.3.5.3 Implementation

The implementation of the new method is shown schematically in Fig. 2.24. A third-order 3D polynomial is used as fit function, corresponding to 20 fit parameters. The magnitude and phase images are read by the program. Only points with intensities above a chosen threshold are retained so that the fit is not loaded by points containing only noise. If the remaining number still exceeds a chosen limit points are discarded from the list at regular intervals. Typically 10^5 points are used for the fit, corresponding to over 45 points per direction in space. Identification of the global first-order optimum turned out to be essential for successful phase correction. To this end the starting points for the first-order fits in the parameter vectors $\boldsymbol{k}_1$ are first taken from a suitable lattice. For the constant term only a 2π interval has to be considered, values of -1.5, 0, 1.5, and 3 rad are chosen, respectively. The linear component for each spatial direction is chosen such that the change in phase along the image extension amounts to 0, ± 1, ± 2, or ± 4 rad, respectively. The 4D lattice vectors are sorted by increasing magnitude and used one by one in this order. For each starting point the maximum obtained according to expression (2.152) is saved along with the parameter vector. Optimizations starting from lattice points is aborted if the attained real-part sum exceeds a chosen fraction of the magnitude sum. If this criterion is not fulfilled for all of the 1,372 lattice points, a chosen number of optimizations with random starting points from a larger domain are executed and the parameter vector resulting from the most successful optimization is retained. If desired second- and third-order fits are executed with parameters from the lower-order fit as starting point. The new parameters are randomly chosen for each of the optimizations. Typically, two second-order and one third-order optimization is added. A lattice with six dimensions for the additional second-order terms or even ten dimensions for the additional third-order terms would be very large. Addition of the second- and third-order was observed to lead to a comparatively small increase of the sum in expression (2.152).

Optimization was performed in MATLAB® R2007a with a quasi-Newton method. It yielded better results in shorter times than a simplex method. For the first-order optimization the analytical gradients were provided. The computation time on a simple personal computer (Intel P4 3.2 GHz processors, 1 GB RAM, Microsoft Windows XP Pro SP2 operating system) is of the order of minutes. In order to investigate computation times results for several runs on a more efficient multi-core computer were averaged (Intel Xeon CPU 5130@2.00 GHz processor, 14 GB RAM, XP Pro x64 Edition SP2 operating system). The computation time as a function of number of points included and order is compiled in Table 2.1 (all first-order

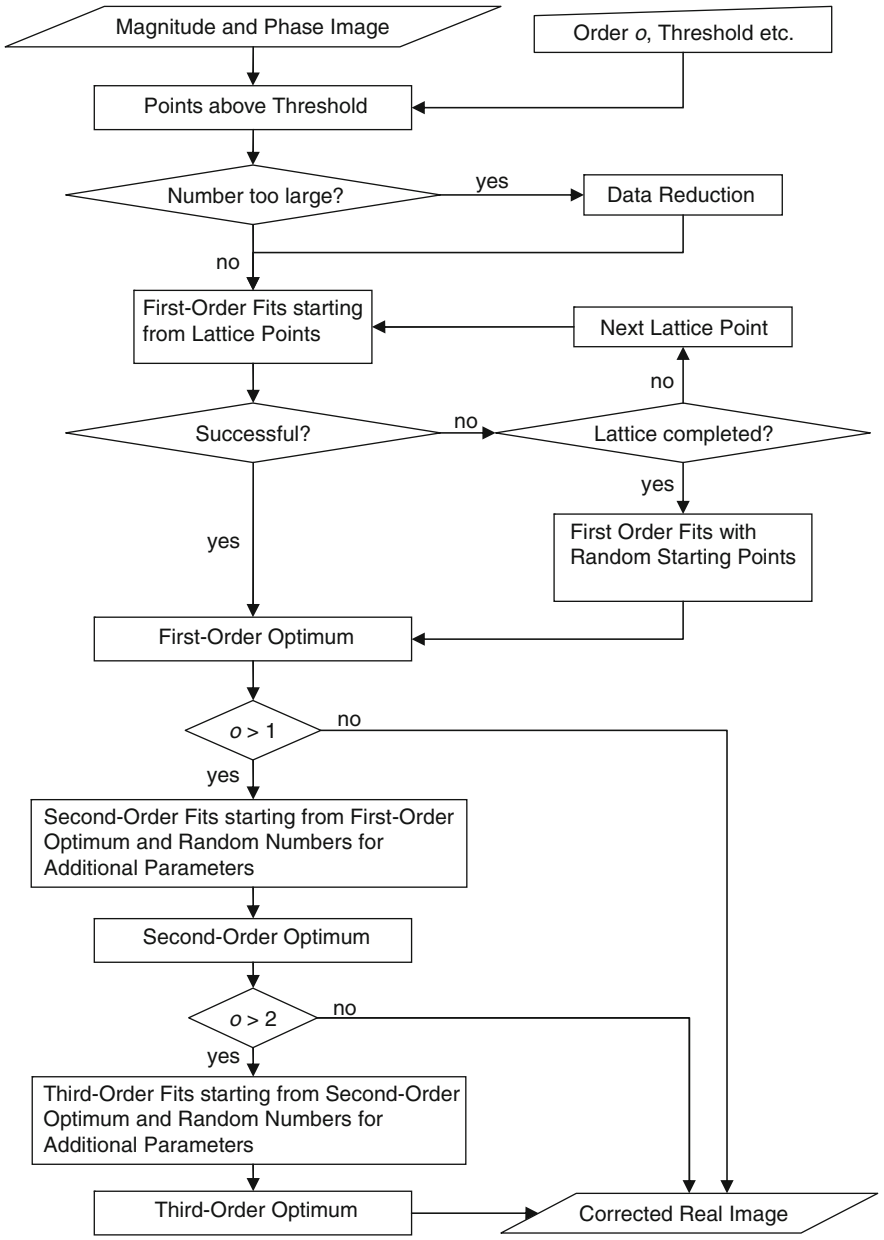

Fig. 2.24 Procedure of phase correction. Reprinted from [33] © 2009, with permission from Elsevier

Table 2.1 Computation time for phase correction in seconds

Number of points	13,351	26,922	53,836	107,263	214,514
Second order	4	8	16	40	121
Third order	39	78	157	377	1,005

calculations took less than 2 s). For the first three numbers of points computation time scales with the number of points, then the increase is over proportional. At a given number of points third-order optimization takes about ten times longer than the second-order optimization. Including all fourth-order terms would probably lead to hardly acceptable computation times. Concerning the number of points included, satisfactory results were already obtained with the lowest value corresponding to about 23 points per spatial dimension.

2.3.5.4 Application of the Method to Test Cases

The method was developed to investigate the deposition of small particle masses in fibrous filters in situ, see Sect. 4.1. Here it is first examined and discussed for several test cases.

First it was investigated if the polynomial series is suitable and sufficiently flexible to map phase errors that occur experimentally. A 3D gradient-echo was used as test image. Here inhomogeneities of the static field are not refocused as it is the case for a SE image. A sample tube was filled with an aqueous Gadovist solution (relaxation agent, 2.5 mmol/l). The entire available sample volume was filled in order to assess the performance of the method in the border areas. Within the sample SNR is so high that according to (2.146) or (2.148) and (2.150) the magnitude and phase-corrected real-part image should be nearly identical. Deviations indicate an insufficient phase correction. Outside the sample there should be only noise. Figure 2.25 shows four out of 64 horizontal slices through the sample in four columns. In the first three rows the difference of the magnitude image shown in the last row and the corrected real-part image is represented for a first, second, and third-order polynomial, respectively. Black represents full correction, white a difference of 10% of the maximum intensity in the magnitude image. The first row shows that for slices near the center already the first-order polynomial leads to a high degree of correction. For slices near the border, however, errors of up to 10% remain. These errors are markedly reduced in second order, see second row, and no longer observable in third order in the third row. The presence of pattern outside the sample indicates experimental artifacts. In general a bright border at the rim of the sample shows that at the interface phase errors occur that are not described by a smooth function. Apart from this, correction with the new method is successful for this data set and a third-order polynomial is suitable and sufficiently flexible.

Next the ability of the method to correct the phase in the case of low SNR and isolated regions was investigated. To this end known masses of oil-filled microcapsules with different spatial distributions were imaged with a fast SE

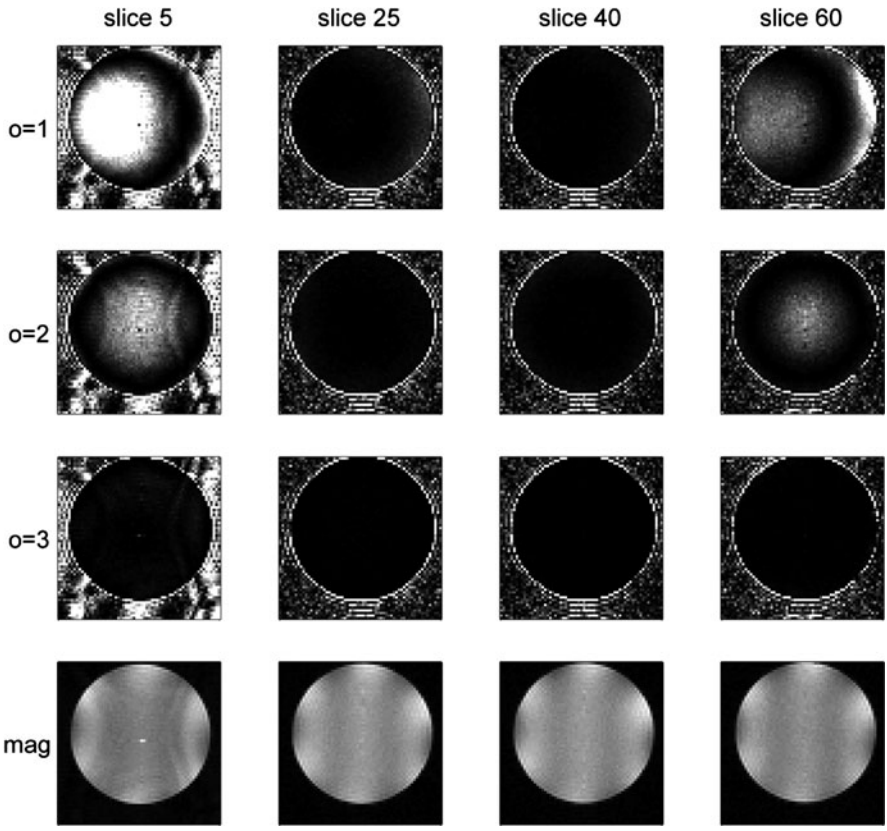

Fig. 2.25 Convergence of phase correction with order of polynomial (1–3) for two slices close to the border of the sample (5 and 60) as well as two slices in the middle (25 and 40). The first three rows show the difference of the magnitude and real-part image. For this data set with high SNR the difference should approach zero (*black*). *Last row*: magnitude image. Reprinted from [33] © 2009, with permission from Elsevier

sequence. The total signal with and without phase correction is plotted against the total mass in Fig. 2.26. The linear relation for the phase-corrected data in the double-logarithmic plot shows the expected proportionality (note that a linear dependence with positive ordinate intersection does not appear linear in a double-logarithmic plot). For the magnitude data the calibration curve deviates at low masses toward the plateau of the sum of magnitude noise.

The applicability of the method to large data sets was tested for the image of a fibrous filter immersed in an aqueous Gadovist solution with tenside. The data set acquired with a fast SE sequence comprises 256^3 points. Phase correction was successful. However, marked intensity distortions occur in the phase-corrected real-part image in the vicinity of small air bubbles which remain in the sample in spite of thorough degassing. In the magnitude image, air bubbles are not easily distinguished for fibers and lead to errors in the determination of fiber structure.

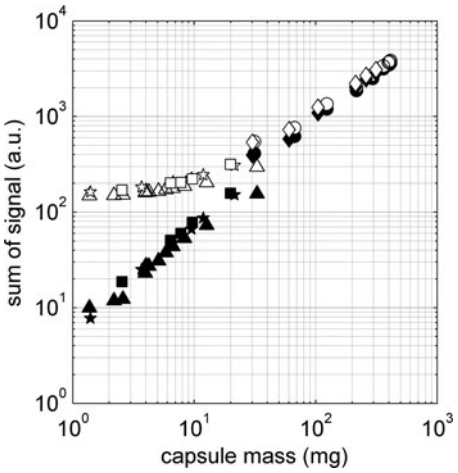

Fig. 2.26 Signal calibration with (filled symbols) and without (open symbols) phase correction. Reprinted from [33] © 2009, with permission from Elsevier

Phase correction could thus be useful also for images with high SNR in the automatic detection of air bubbles or interfaces between different susceptibilities in general.

The method was also applied successfully to a series of volume images with increasing signal decay by transverse relaxation. For early high SNR images noise has almost the same influence in the magnitude and phase-corrected real-part image. However, magnitude images with strong decay and low SNR approach the limit of magnitude noise. This leads to errors, e.g., in the fit of the transverse relaxation time T_2.

Finally it is noted that the method can also be used for data in which the spin density can appear with negative sign, e.g., images with inversion-recovery or fat-water filter. To this end the complex image is squared and the fit function is used to approximate the double of the phase error. This was shown for simulated data.

References

1. Abragam, A (1961) Principles of nuclear magnetism. Clarendon Press, Oxford
2. Ahn C, Cho Z (1987) A new phase correction method in NMR imaging based on autocorrelation and histogram analysis. IEEE Trans Med Imaging 6(1):32–36
3. Bardakci M, Tillich JE, Holz M (2006) Characterization of structure and transport in porous media by pulsed field gradient (PFG) NMR technique – Part I: Master curve and characteristic inner length. Chem Eng Technol 29(7):847–853. DOI 10.1002/ceat.200600043
4. Behnke B, Schlotterbeck G, Tallarek U, Strohschein S, Tseng LH, Keller T, Albert K, Bayer E (1996) Capillary HPLC-NMR coupling high-resolution NMR spectroscopy in the nanoliter scale. Anal Chem 68(7):1110–1115
5. Bernstein M, Thomasson D, Perman W (1989) Improved detectability in low signal-to-noise ratio magnetic-resonance images by means of a phase-corrected real reconstruction. Med Phys 16(5):813–817

6. Bloch, F (1946) Nuclear induction. Phys Rev 70:460–474
7. Bloch F, Siegert A (1940) Magnetic resonance for nonrotating fields. Phys Rev 57(6):522–527. DOI 10.1103/PhysRev.57.522
8. Bloembergen N, Purcell EM, Pound RV (1948) Relaxation effects in nuclear magnetic resonance absorption. Phys Rev 73:679–712
9. Blümich, B (2000) NMR imaging of materials. Clarendon Press, Oxford
10. Braun S, Kalinowski HO, Berger S (1998) 150 and more basic NMR experiments. Wiley-VCH, Weinheim
11. Bretthorst, GL (2008) Automatic phasing of MR images. Part I: Linearly varying phase. J Magn Reson 191(2):184–192. DOI 10.1016/j.jmr.2007.12.010
12. Callaghan PT (1990) PGSE MASSEY, a sequence for overcoming phase instability in very-high-gradient spin-echo NMR. J Magn Reson 88(3):493–500
13. Callaghan PT (1991) Principles of nuclear magnetic resonance microscopy. Clarendon Press, Oxford
14. Canet D (1996) Nuclear magnetic resonance: Concepts and methods. Wiley, Chichester
15. Caprihan A, Fukushima E (1990) Flow measurements by NMR. Phys Rep 198(4):195–235
16. Cavanagh J, Fairbrother WJ, Palmer AG III, Skelton NJ (1996) Protein NMR spectroscopy. Academic Press, San Diego
17. Chang Z, Xiang, Q (2005) Nonlinear phase correction with an extended statistical algorithm. IEEE Trans Med Imaging 24(6):791–798. DOI 10.1109/TMI.2005.848375
18. Chen CN, Hoult DI, Sank VJ (1983) Quadrature detection coils – A further square-root2 improvement in sensitivity. J Magn Reson 54(2):324–327
19. Cotts RM, Hoch MJR, Sun T, Markert JT (1989) Pulsed field gradient stimulated echo methods for improved NMR diffusion measurements in heterogeneous systems. J Magn Reson 83(2):252–266
20. Edelstein WA, Glover GH, Hardy CJ, Redington RW (1986)The intrinsic signal-to-noise ratio in NMR imaging. Magn Reson Med 3(4):604–618
21. Engelke F (2010) Virtual photons in magnetic resonance. Concept Magn Res A 36A(5):266–339. DOI 10.1002/cmr.a.20166
22. Ernst RR, Bodenhausen G, Wokaun A (1987) Principles of nuclear magnetic resonance in one and two dimensions. Clarendon Press, Oxford
23. Feynman RP (1985) QED : The strange theory of light and matter. Alix G. Mautner memorial lectures. University Press, Princeton, NJ
24. von Garnier A, Hardy EH, Schweitzer JM, Reimert R (2007) Differentiation of catalyst and catalyst support in a fixed bed by magnetic resonance imaging. Chem Eng Sci 62(18–20, Sp. Iss. SI):5330–5334. DOI 10.1016/j.ces.2007.03.034
25. Geen H, Freeman R (1991) Band-selective radiofrequency pulses. J Magn Reson 93(1):93–141
26. Gladden LF, Alexander P (1996) Applications of nuclear magnetic resonance imaging in process engineering. Meas Sci Technol 7(3):423–435
27. Glover GH, Hayes CE, Pelc NJ, Edelstein WA, Muller OM, Hart H, Hardy CJ, ODonnell M, Barber W (1985) Comparison of linear and circular-polarization for magnetic-resonance imaging. J Magn Reson 64(2):255–270
28. Goldman M (1991) Quantum description of high-resolution NMR in liquids. Oxford University Press, Oxford
29. Grosse J, Dietrich B, Martin H, Kind M, Vicente J, Hardy EH (2008) Volume image analysis of ceramic sponges. Chem Eng Technol 31(2):307–314. DOI 10.1002/ceat.200700403
30. Halbach RE, Battocletti JH, Sances A, Bowman RL, Kudravcev V (1979) Cylindrical crossed-coil NMR limb blood flowmeter. Rev Sci Instrum 50(4):428–434
31. Hardy EH (2006) Magnetic resonance imaging in chemical engineering: Basics and practical aspects. Chem Eng Technol 29(7):785–795. DOI 10.1002/ceat.200600046
32. Hardy EH, Hoferer J, Kasper G (2007) The mixing state of fine powders measured by magnetic resonance imaging. Powder Technol 177(1):12–22. DOI 10.1016/j.powtee.2007.02.042
33. Hardy EH, Hoferer J, Mertens D, Kasper G (2009) Automated phase correction via maximization of the real signal. Magn Reson Imaging 27(3):393–400. DOI 10.1016/j.mri.2008.07.009

34. Harris RK (1986) Nuclear magnetic resonance spectroscopy. Longman Scientific and Technical, Essex
35. Hoult D, Ginsberg N (2001) The quantum origins of the free induction decay signal and spin noise. J Magn Reson 148(1):182–199
36. Hoult DI (2009) The origins and present status of the radio wave controversy in NMR. Concept Magn Res A 34A(4):193–216. DOI 10.1002/cmr.a.20142
37. Hoult DI, Richards RE (1976) Signal-to-noise ratio of nuclear magnetic-resonance experiment. J Magn Reson 24(1):71–85
38. Hurlimann MD, Burcaw L, Song YQ (2006) Quantitative characterization of food products by two-dimensional D-T-2 and T-1-T-2 distribution functions in a static gradient. J Colloid Interface Sci 297(1):303–311. DOI 10.1016/j.jcis.2005.10.047
39. Jin J (1999) Electromagnetic analysis and design in magnetic resonance imaging. CRC Press, Boca Raton
40. Karlicek RF, Lowe IJ (1980) Modified pulsed gradient technique for measuring diffusion in the presence of large background gradients. J Magn Reson 37(1):75–91
41. Kimmich R (1997) NMR tomography, diffusometry, relaxometry. Springer-Verlag, Berlin, Heidelberg, New York
42. Kreyszig E (1970) Introductory mathematical statistics. Wiley, New York
43. Kriesten E, Alsmeyer F, Bardow A, Marquardt W (2008) Fully automated indirect hard modeling of mixture spectra. Chemom Intell Lab Syst 91(2):181–193. DOI 10.1016/j.chemolab.2007.11.004
44. Latour L, Mitra P, Kleinberg R, Sotak C (1993) Time-dependent diffusion-coefficient of fluids in porous-media as a probe of surface-to-volume ratio. J Magn Reson Ser A 101(3):342–346
45. Liu J, Koenig J (1990) An automatic phase correction method in nuclear-magnetic-resonance imaging. J Magn Reson 86(3):593–604
46. Meyer F (1994) Topographic distance and watershed lines. Signal Process 38(1):113–125
47. Noll DC, Nishimura DG, Macovski A (1991) Homodyne detection in magnetic-resonance-imaging. IEEE Trans Med Imaging 10(2):154–163
48. Ohser J, Mcklich, F (2000) Statistical analysis of microstructures in materials science. Wiley, Chichester, England
49. Pople JA, Schneider WG, Bernstein HJ (1959) High-resolution nuclear magnetic resonance. McGraw-Hill Book Co, New York
50. Redpath TW, Norris DG, Jones RA, Hutchison JMS (1984)A new method of NMR flow imaging. Phys Med Biol 29(7):891–895
51. Rosenfeld D (1998) An optimal and efficient new gridding algorithm using singular value decomposition. Magn Reson Med 40(1):14–23
52. Sankey MH, Holland DJ, Sederman AJ, Gladden LF (2009) Magnetic resonance velocity imaging of liquid and gas two-phase flow in packed beds. J Magn Reson 196(2):142–148. DOI 10.1016/j.jmr.2008.10.021
53. Sarkar S, Heberlein K, Metzger G, Zhang X, Hu X (1999) Applications of high-resolution echoplanar spectroscopic imaging for structural imaging. J Magn Reson Imaging 10(1):1–7
54. Sedarat H, Nishimura DG (2000) On the optimality of the gridding reconstruction algorithm. IEEE Trans Med Imaging 19(4):306–317
55. Sederman AJ, Alexander P, Gladden LF (2001) Structure of packed beds probed by magnetic resonance imaging. Powder Technol 117(3):255–269
56. Shankar R (1980) Principles of quantum mechanics. Plenum Press, New York
57. Singer JR (1959) Blood flow rates by nuclear magnetic resonance measurements. Science 130(3389):1652–1653
58. Slichter CP (1980) Principles of magnetic resonance. Springer-Verlag, Berlin
59. Song YQ, Venkataramanan L, Hurlimann MD, Flaum M, Frulla P, Straley C (2002) T-1-T-2 correlation spectra obtained using a fast two-dimensional Laplace inversion. J Magn Reson 154(2):261–268. DOI 10.1006/jmre.2001.2474
60. Stejskal EO (1965) Use of spin echoes in a pulsed magnetic-field gradient to study anisotropic restricted diffusion and flow. J Chem Phys 43(10P1):3597–3603

61. Stejskal EO, Tanner JE (1965) Spin diffusion measurements – Spin echoes in presence of a time-dependent field gradient. J Chem Phys 42(1):288–292
62. Stepisnik J (1985) Measuring and imaging of flow by NMR. Prog Nucl Magn Reson Spectrosc 17(Part 3):187–209
63. Sudmeier JL, Gunther UL, Albert K, Bachovchin WW (1996) Sensitivity optimization in continuous-flow FTNMR. J Magn Reson Ser A 118(2):145–156
64. Tisdall D, Atkins M (2005) MRI denoising via phase error estimation. In: Fitzpatrick JM, Reinhardt JM (eds) Medical imaging 2005: Image processing, Pt 1–3, *Proceedings of the society of photo-optical instrumentation engineers (spie)*, vol 5747. Medical Imaging 2005 Conference, San Diego, CA, 15–17 February 2005, pp 646–654. DOI 10.1117/12.595677
65. Torrey HC (1956) Bloch equations with diffusion terms. Phys Rev 104(3):563–565
66. VanAs H, Schaafsma TJ (1987) Measurement of flow by the NMR repetitive pulse method. J Magn Reson 74(3):526–534
67. van de Ven FJM (1995) Multidimensional NMR in liquids: Basic principles and experimental methods. VCH Publishers, Inc, New York, Weinheim, Cambridge
68. Vincent L, Soille P (1991) Watersheds in digital spaces – An efficient algorithm based on immersion simulations. IEEE Trans Pattern Anal Mach Intell 13(6):583–598

http://www.springer.com/978-3-642-21627-5

NMR Methods for the Investigation of Structure and Transport

Hardy, E.H.

2012, XVIII, 210 p., Hardcover
ISBN: 978-3-642-21627-5